12-2015

Deposition and Characterization of Carbon Nanotubes (CNTS) Based Films for Sensing Applications

Amila C. Dissanayake
Western Michigan University, amila.8352@gmail.com

DEPOSITION AND CHARACTERIZATION OF CARBON NANOTUBES (CNTs) BASED FILMS FOR SENSING APPLICATIONS

by

Amila C. Dissanayake

A dissertation submitted to the Graduate College
in partial fulfillment of the requirements
for the degree of Doctor of Philosophy
Physics
Western Michigan University
December 2015

Doctoral Committee:

Asghar N. Kayani, Ph.D., Chair
Muralidhar K. Ghantasala, Ph.D.
Sung G. Chung, Ph.D.
Paul Pancella, Ph.D.

DEPOSITION AND CHARACTERIZATION OF CARBON NANOTUBES (CNTs) BASED FILMS FOR SENSING APPLICATIONS

Amila C. Dissanayake, Ph.D.

Western Michigan University, 2015

The advent of carbon nanotubes (CNTs) has opened up lot of novel applications because of their unique electrical and mechanical properties. CNTs are well known material for its exceptional electrical, mechanical, optical, thermal and chemical properties. A single-wall nanotube (SWNT) can be either semiconducting, metallic or semi-metallic, based on its chirality and diameter. SWNTs can be used in transistor device as active channels due to high electron mobility (~10000 $cm^2/(V\ s)$, electrical interconnects, nano-scale circuits, field-emission displays, light-emitting devices and thermal heat sinks due to low resistivity, high current density (~$10^9 A\ cm^{-2}$) and high thermal conductivity (~3500 $W\ m^{-1}$). Further, their high Young's modulus and fracture stress is suitable for various sensing applications such as strain/pressure and use in chemical/biological sensors. This work mainly involves the deposition of CNT-based films following two different methods via a conventional microwave chemical vapor deposition (MWCVD) and spinning CNT-composites, and explored the possibility of using CNT-based films in strain gauge applications. Deposited films are characterized and analyzed for their structure, microstructure, composition and electrical properties. Rutherford Backscattering Spectrometry (RBS), X-ray Reflectivity (XRR), Scanning

Electron Microscopy (SEM), X-ray Diffraction (XRD), X-ray Photoelectron Spectroscopy (XPS), Atomic Force Microscopy (AFM) and electrical impedance measurement techniques are used to characterize the films prepared by both the above mentioned methods. The synthesis/deposition process is improved based on the observed films properties.

A carbon nanotube forest grown on the Si (100) substrate with Ni as a catalyst using CVD system shows an amorphous nature due to loss of catalytic activity of Ni nano-islands. XPS and RBS data show Ni nano-particles diffused into the Si substrate and surface layer of Ni particles turns out to nickel silicide. The diffusion of Ni nano-particles and nickel silicide formation occurs due to annealing and longer plasma treatment. Because of annealing and plasma treatment, the phase of Ni changes from amorphous to hexagonal close packed with $p6_3/mmc$ space group and cubic Fm-3m with plasma treatment time. Further, the role of Ni diffusion into silicon in the catalyzing CNT formation has been investigated and discussed further.

Carbon nanotube-polymer nanocomposite films are synthesized using spin coating of a polyurethane and CNTs mixture. This produced porous films with the average pore size of around 10μm. The electrical conductivity of the CNTs-polymer composites increases with the carbon nanotube loading, and composites show frequency independent conductivity as frequency increases. Generally, ac conductivity as a function of signal frequency for the above composites shows conductive behavior. The parallel RC-circuit model reveals that composites without any cross-linkers are uniform and homogenous. The composite with low carbon nanotube content with cross-linkers shows

the same trend. But composites with higher carbon nanotube content with cross-linkers shows poor dispersion and agglomeration of carbon nanotubes.

ACKNOWLEDGEMENTS

First and foremost I would like to express my sincere gratitude to my thesis advisor Dr. Asghar Kayani for his invaluable assistance, patience and motivation during my doctoral studies. I would also like to thank Dr. Muralidhar Ghantasala for his support and guidance during all the time of my research. I greatly appreciate the support and encouragement provided by my dfissertation committee members Dr. Sung Chung and Dr. Paul Pancella to successfully complete my dissertation. I would like to thank Dr. Valery Bliznyuk and Dr. Margaret Joyce for their help at the engineering college. I am really appreciative of the Department of Physics and Graduate College of Western Michigan University for providing me the financial support for my dissertation work.

I would especially like to thank Dr. Suntharampillai Thevuthasan for providing me an internship in the Pacific Northwest National Laboratory (PNNL) as well as assistance, motivation, and enthusiasm to pursue my carrier as a scientist. I would also like to thank other scientists at PNNL who helped me at various stages of this research, especially Dr. Shuttha Shutthanandan, Dr. Vijayakumar Murugesan, Dr. Praveen Thallapally, Dr. Manjula Nandasiri, Dr. Mark Bowden and Dr. Tamas Varga.

I would like to acknowledge PNNL for providing research facilities to me through an internship to complete my dissertation work. The part of research was performed using Environmental Molecular Sciences Laboratory (EMSL), a national scientific user facility

sponsored by the Department of Energy's Office of Biological and Environmental Research and located at PNNL. PNNL is operated for the U.S. DOE by Battelle Memorial Institute under contract number DE-AC05-76RL01830.

Finally, I would like to dedicate this dissertation to my parents Mrs. B.M. Dissanayake and Mr. M.L.W. Dissanayake for their unconditional love, support, patience and understanding. Simply, I do not have enough words to thank them. Thanks are extended to the colleagues and friends who motivated and supported me to my academic carrier. It is not possible to complete this journey without all of your support.

Amila C. Dissanayake

TABLE OF CONTENTS

Table of Contents—Continued

CHAPTER

Table of Contents—Continued

CHAPTER

LIST OF TABLES

LIST OF FIGURES

List of Figures—Continued

List of Figures—Continued

List of Figures—Continued

CHAPTER 1

INTRODUCTION

The objectives of this dissertation are to: (1) understand and optimize the growth of carbon nanotubes (CNTs) on the Si substrate in terms of their structural and electronic properties, and (2) synthesize and optimize novel carbon nanotube-polymer composites in terms of mechanical and electronic properties for strain sensor applications. In this chapter, a general overview of carbon nanotubes, CNTs growth process by plasma enhanced chemical vapor deposition (PECVD) technique, carbon nanotube strain sensors, and the objectives of the study will be presented. A literature survey of the growth of CNTs by PECVD technique and carbon nanotube strain sensors is presented in the second chapter. In the third chapter, thin film deposition by Physical Vapor Deposition (PVD), Plasma Enhanced Chemical Vapor Deposition (PECVD), spin coating, and characterization techniques used in this study are briefly discussed, followed by the sample preparation. The optimization of CNTs growth and synthesis of CNTs polymer composite parameters are discussed in detail in the results and discussion. Then, growth of CNTs, synthesis of CNTs-polymer composite, and characterization of thin films is discussed, along with their structural, physical, mechanical, and electrical properties. Finally, the results and conclusion of this study are summarized.

1.1 Carbon nanotubes (CNTs)

Carbon is at the sixth position of the periodic table. Single carbon atom has six electrons with $1s^2$, $2s^2$ and $2p^2$ atomic orbital configuration. This electronic configuration leads to sp (e.g., C_2H_2), sp^2 (e.g., graphite, graphene), or sp^3 (e.g., diamond) hybridization forms. This unique property arises due to its position in the periodic table. The invention of nanometer size sp^2 bonded carbon allotropes such as fullerenes, carbon nanotube, and graphene has motivated the research community around the globe [1] [2] [3]. The structures of allotropes are shown in Figure 1. Since graphene and carbon nanotube are close in physical structure, most of the properties of CNTs originate from graphene.

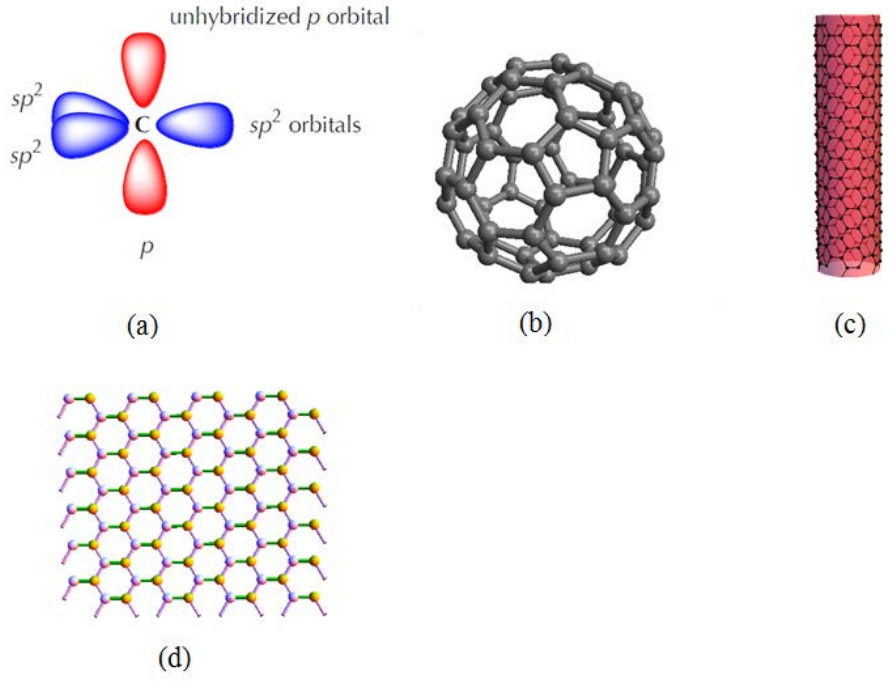

Figure 1. sp2 hybridization of carbon and its allotropes (a) The three sp2 hybridized orbital are in plane and 2p orbital makes right angle to the plane **[4]** (b) Fullerene **[5]** (c) Carbon nanotube (d) Graphene. (Image courtesy: Wolfram demonstration).

1.1.1 Graphene

Graphene is a planar allotrope of carbon where all the carbon atoms form sp^2 bonds in a single plane [6]. The planar honeycomb structure of graphene is shown in Figure 2**.** The sp^2 form three σ bonds, which are the strongest covalent bond. The σ bonds electrons localized along the plane connecting carbon atoms and are responsible for the strength and mechanical properties of graphene and CNTs. The $2p_z$ electrons form covalent bonds called π- bonds, where the electron cloud is at a right angle to the carbon atom plane. These delocalized electrons are responsible for the electronic properties of graphene and CNTs. The carbon-carbon bond length is a_{c-c} approximately 1.42 Å. Graphene lattice structure can be considered as Bravais lattice with a basis of two atoms indicated as A

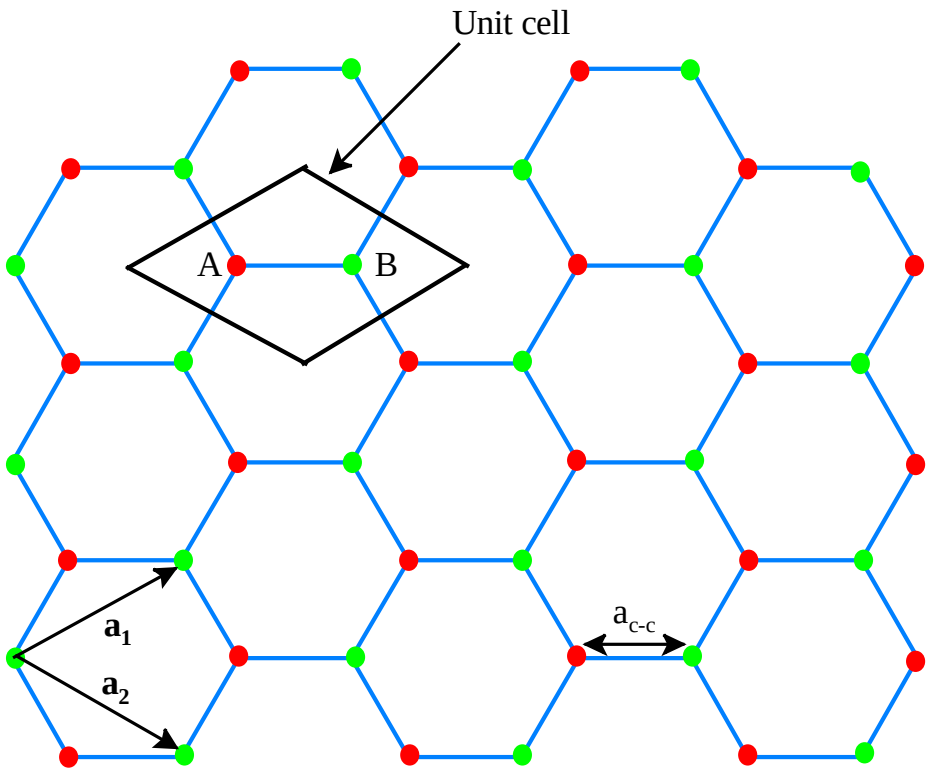

Figure 2. The honeycomb crystal structure of graphene. The primitive unit cell is indicated by parallelogram with a basis of two atoms A and B. (Adopted from Philip Wong et al. **[6]**)

and B in Figure 2.These two atoms contribute two π electrons per unit cell to the electronic properties of graphene. The primitive unit cell can be considered an equilateral parallelogram with side $a = \sqrt{3}\, a_{c-c} = 2.46$ Å . The primitive unit vectors are defined as in Figure 2 with $|a_1| = |a_2| = a$.

$$\boldsymbol{a_1} = \left(\frac{\sqrt{3}a}{2}, \frac{a}{2}\right), \quad \boldsymbol{a_2} = \left(\frac{\sqrt{3}a}{2}, -\frac{a}{2}\right) \ldots\ldots\ldots\ldots\ldots\ldots\ldots\ldots\ldots\ldots\ldots\ldots\ldots\ldots\ldots\ldots\ldots\ldots \quad (1)$$

The reciprocal lattice of graphene shown in Figure 3 is also a hexagonal lattice with a 90° rotation with respect to the direct lattice. The reciprocal lattice vectors are defined with $|b_1| = |b_2| = 4\pi/\sqrt{3}\, a$.

$$\boldsymbol{b_1} = \left(\frac{2\pi}{\sqrt{3}a}, \frac{2\pi}{a}\right), \boldsymbol{b_2} = \left(\frac{2\pi}{\sqrt{3}a}, -\frac{2\pi}{a}\right) \ldots\ldots\ldots\ldots\ldots\ldots\ldots\ldots\ldots\ldots\ldots\ldots\ldots\ldots\ldots\ldots\ldots\ldots \quad (2)$$

The Brillouin zone is illustrated as the green hexagon in Figure 3 with sides of length $b_{BZ} = |b_1|/\sqrt{3} = 4\pi/3a$ and area equal to $8\pi^2/\sqrt{3}a^2$, which is a main tool for describing the electronic band of solids. There are three high symmetry points in the Brillouin zone which are used for describing the dispersion of graphene. These points are identified as the Γ-point, the M-point, and the K-point [7].

The energy dispersion relation for π- orbital calculated by *Nearest neighbor tight-binding* (NNTB) model [8].

$$E(\boldsymbol{k})^{\pm} = \pm\gamma\sqrt{1 + 4\cos\frac{\sqrt{3}a}{2}k_x\cos\frac{a}{2}k_y + 4\cos^2\frac{a}{2}k_y} \ldots\ldots\ldots\ldots\ldots\ldots\ldots\ldots\ldots\ldots\ldots \quad (3)$$

Where γ- hoping or transfer energy

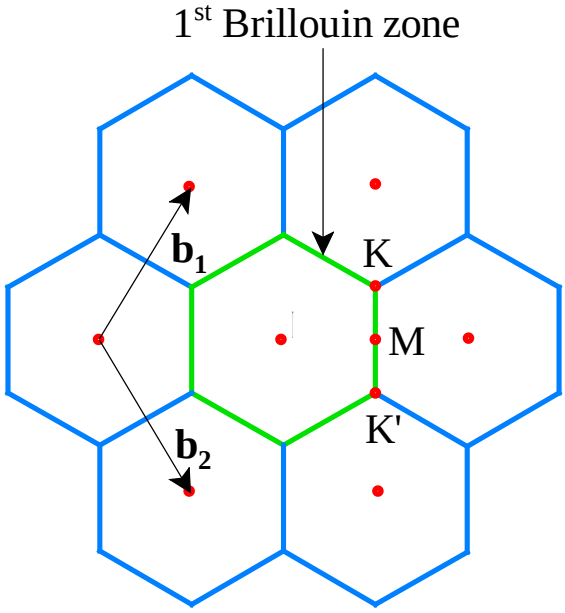

Figure 3. The reciprocal lattice of graphene. The first Brillouin zone is indicated by the green hexagon with the high symmetry point labeled as Γ, M and K located at the center midpoint of the side and corner of the hexagon respectively. (Adopted from Philip Wong et al. **[6]**)

Figure 4 shows the 3D plot of NNTB dispersion all over the Brillouin zone. The upper half of the curve represents the dispersion of the conduction (π^*) band and the lower half is the valance (π) band. The most striking feature is that conduction and the valance band are degenerated at the K-point, owing to the absence of a band gap at Fermi energy. Therefore, graphene is considered as a semi-metal or zero band gap semi-conductor.

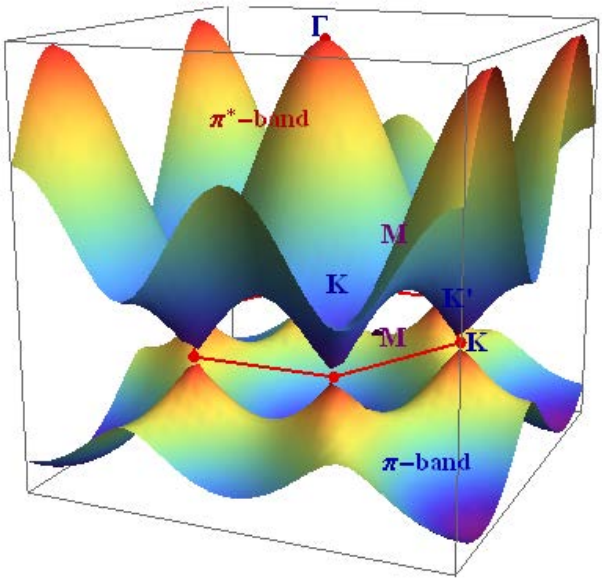

Figure 4. The nearest neighbor tight-binding band structure of graphene. The hexagonal Brillouin zone is super imposed and touches the energy bands at the K-points. (Image courtesy: Wolfram demonstration)

1.1.2 Nanotube structure

There are two types of CNTs, called single-wall CNTs (SWCNT) and multi-wall CNTs (MWCNT) as shown in Figure 5. A single-wall CNT can be considered as a void cylindrical structure of carbon atoms with a diameter that ranges from 0.5 nm to about 10 nm and a length that varies from a few microns to centimeters. A MWCNT has multiple concentric cylindrical walls with spacing between walls equivalent to the interlayer spacing of graphite. CNTs are considered as 1-D nano-materials, due to their small diameter that direct the movement of electron along the tube axis.

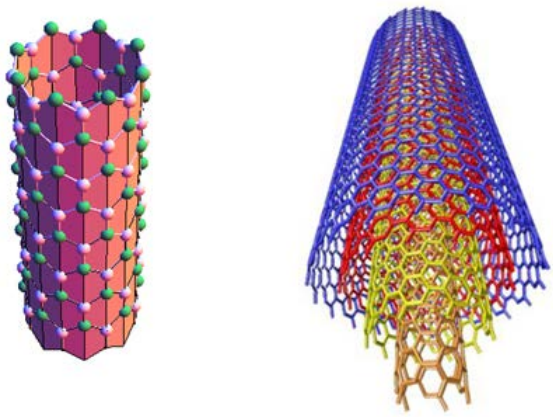

Figure 5. Illustration of two types of CNTs (a) A single-wall CNT (Image courtesy: Wolfram demonstration) (b) A multi-wall CNT **[9]**.

It is easy to understand the origin of the different families of CNT by considering that a CNT comes from the wrapping of a graphene sheet. Further, this mathematical construction shows the way to determine the primitive lattice of CNTs, which is required to develop the CNT band structure.

With reference to Figure 6, a single-wall CNT can be conceptually visualized by considering wrapping the dashed line containing primitive lattice points A and C with the dashed line containing primitive lattice points B and D, such that point A overlaps with B, and C with D to form the nanotube. The CNT can be characterize by three parameters, the chiral vector $\mathbf{C_h}$, the translation vector **T,** and the chiral angle θ. The chiral vector is the geometrical parameter that uniquely defines a CNT, and $|C_h| = C_h$ is the circumference. $\mathbf{C_h}$ is defined as the vector connecting any two primitive lattice points of graphene such that when wrapping into a nanotube these two points coincide. In general,

$$C_h = n\boldsymbol{a_1} + m\boldsymbol{a_2} = (n, m) \text{ (n,m are positive integers,} 0 \leq m \leq n) \ldots\ldots\ldots\ldots\ldots \quad (4)$$

The resulting carbon nanotube is described as an (n, m) CNT.

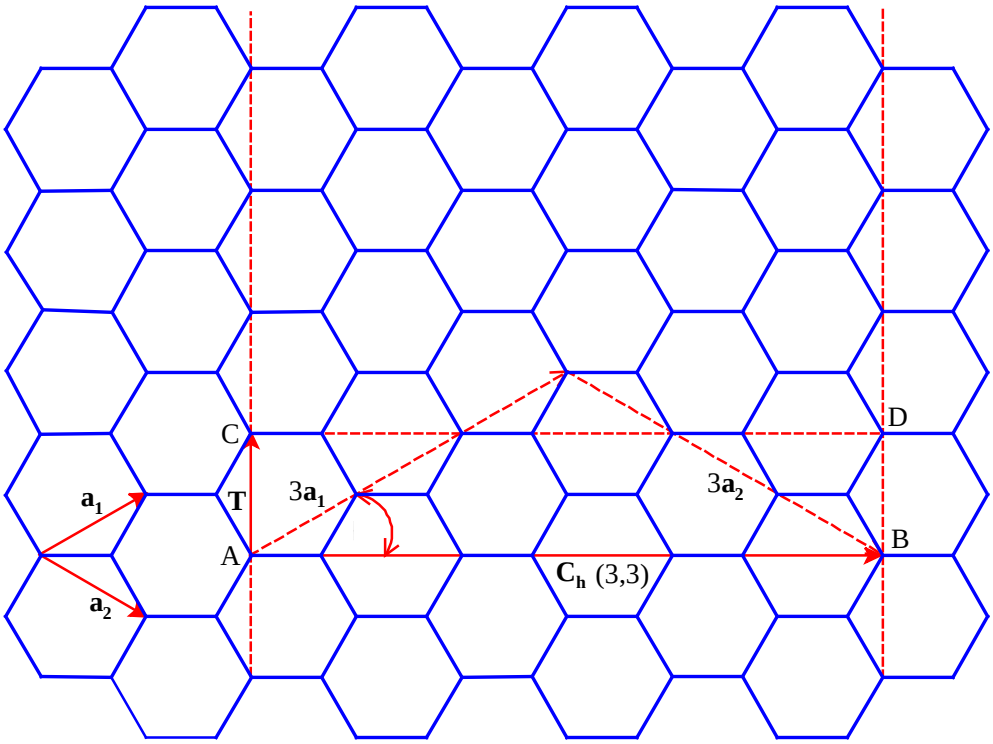

Figure 6. An illustration to describe the mathematical construction of a CNT from graphene. Wrapping the dashed line constraining points A and C to the dash line with points B and D consequences in the (3,3) armchair carbon nanotube with θ = 30°. The CNT primitive unit cell is the cylinder formed by wrapping line AC onto BD. (Adopted from Philip Wong et al. **[6]**)

1.1.3 CNT Brillouin zone

The wavevectors defining the CNT of the first Brillouin zone are the reciprocals of the primitive unit cell vectors given by the reciprocity condition,

$$e^{i(K_a+K_c).(C_h+T)} = 1 \ldots\ldots\ldots\ldots\ldots\ldots\ldots\ldots\ldots\ldots\ldots\ldots\ldots\ldots\ldots\ldots\ldots\ldots\ldots\ldots\ldots\ldots\ldots\ldots\ldots\ldots \quad (5)$$

where K_a is the reciprocal lattice vector along the tube axis and K_c is along the circumferential direction.

The allowed wavevectors *within* the Brillouin zone can be determined from the Bloch wave functions. The allowed wavevectors k along the axial direction are obtained by periodic boundary conditions on the Bloch wave functions, resulting in the set of wavevectors,

$$k = \frac{2\pi}{N_{uc}T} l, l = 0,1, \dots, N_{uc} - 1, \dots\dots\dots\dots\dots\dots\dots\dots\dots\dots\dots\dots\dots\dots\dots\dots\dots\dots\dots\dots. \quad (6)$$

where N_{uc} is the number of unit cells in the nanotube. The maximum value of *l* is determined by the condition that the solution for *k* is confined to the first Brillouin zone. In the case of very long CNTs, i.e., $N_{uc} \gg 1$ [10], the spacing between *k*- values becomes extinct and *k* can be considered as a continuous parameter along the tube axis,

$$k = \left(-\frac{\pi}{T}, \frac{\pi}{T}\right) \dots\dots\dots\dots\dots\dots\dots\dots\dots\dots\dots\dots\dots\dots\dots\dots\dots\dots\dots\dots\dots\dots\dots\dots \quad (7)$$

where wavevectors have been centered to be symmetric about zero with the standard Brillouin zone convention.

Applying the same boundary conditions to determine the wavevectors q along the circumferential direction yield,

$$q = \frac{2\pi}{C_h} j, j = 0,1, \dots, N - 1 \dots\dots\dots\dots\dots\dots\dots\dots\dots\dots\dots\dots\dots\dots\dots\dots\dots\dots\dots\dots\dots\dots \quad (8)$$

where, N is the number of hexagons in a single unit cell of the single-wall nanotube.

It is observed that the wavevector q is quantized compared with the relatively continuous k variable, which implies that allowed CNT wavevectors in the Brillouin zone are composed of a series of 1D cuts of the reciprocal lattice of graphene as shown in Figure 7.

The degeneracy of the valence and conduction band at a K-point resulted in the absence of a bandgap which explains the metallic behavior of graphene. At other points in the

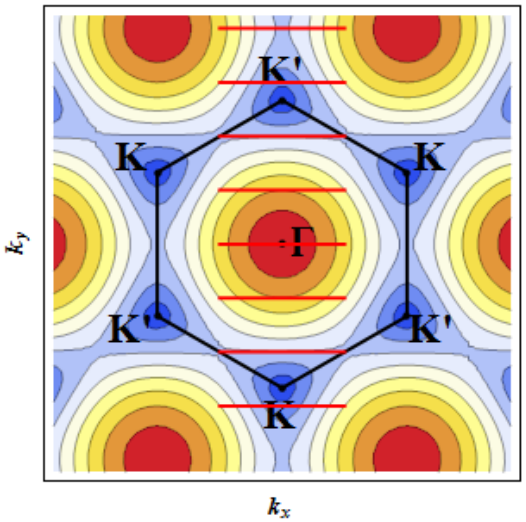

Figure 7. Brillouin zone of a (4,0) CNT overlaid on the contour plot of the conduction band of graphene. (Image courtesy: Wolfram demonstration)

Brillouin zone, there exists an energy gap between two bands. It is obvious that if any of the CNT 1D bands cut the reciprocal lattice of graphene at a K-point, then the nanotube will be metallic; otherwise the nanotubes will have gaps between the valence and conduction bands and hence become semiconducting.

Figure 8 shows Brillouin zones of conducting (3,0) and semiconducting (4,0) nanotubes.

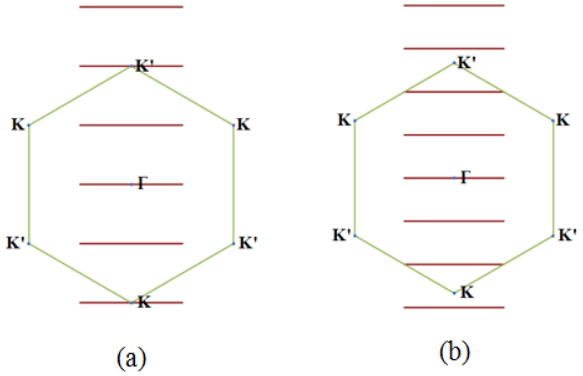

Figure 8. Brillouin zone of (a) (3,0) and (b) (4,0) CNT overlaid on the reciprocal lattice of graphene. The Brillouin zone of CNTs consists of the series of dark lines representing the N (6 and 8 respectively) 1D bands. (Image courtesy: Wolfram demonstration)

1.2 Synthesis of carbon nanotubes

In 1991, the carbon nanotube was discovered by Sumio Iijima in a multi-wall form and single-wall tubes were found two years later [2] [11] [12]. This discovery encouraged the research on carbon nanotube and growth techniques. Carbon nanotubes can be synthesized using different techniques such as arc-discharge; laser ablation, chemical vapor deposition (CVD), and plasma-enhanced chemical vapor deposition (PECVD). This chapter explains the basics of the PECVD technique and the growth process of carbon nanotubes.

1.2.1 PECVD

Microwave sources are very popular at pressures such as 1 to 20 Torr and power levels from 300 W to 2kW and have been widely used for diamond coating [13]. CNT literature

also consisted of several successful demonstrations of MWCNT growth of using microwave CVD [14] [15] [16]. These sources use a 2.45 GHz power supply and the power coupling is achieved through antennas or wave guides. The substrate is located in the plasma chamber. The PECVD system consists of matching network, other power coupling components, mass flow controllers, and vacuum pumps. For CNT growth, the wafer is loaded in the reactor and the system is pumped down to low pressure for minimizing impurities and water vapor. Then, the substrate is heated to the desired temperature and feedstock gas (e.g., methane, acetylene, ethane etc...) is admitted into the reactor chamber with dilution gases such as argon or hydrogen. Because plasma is dissociated, the hydrocarbon creates a lot of reactive radicals that may lead to substantial amorphous carbon deposition. Therefore, it is desirable to dilute the hydrocarbon with argon [17], hydrogen [18], or ammonia [19] .The gas flow rate and chamber pressure can be adjusted to the desired level independent from each other with the aid of a throttle valve. Next, the power from the power source is coupled to the plasma. At the end of the coating, the heater, power source, and the gas flow are turned off and the system is purged with argon gas. The wafer is removed after the reactor cools below 50 °C.

1.2.2 Physical techniques for catalyst preparation

Physical techniques such as magnetron sputtering [20] [21], electron gun evaporation [22], thermal evaporation [23], and ion beam sputtering [24] have been used in catalyst preparation. In general, a thin catalyst film (< 5nm) is applied on the substrate by these techniques. The particle size and the resultant nanotube diameter seem to correlate to film thickness. Thinner films lead to particles with smaller diameter and tube diameter [23]. In PECVD technique, an inert gas, hydrogen or ammonia plasma, is ignited before

admitting feedstock gas for creating catalyst nano-particles using ion bombardment [25] on the substrate at higher temperatures. Typically, Ni, Co, Fe, Cu, Pd, Pt, and Mn metals can be used as a catalyst film for CNT growth in PECVD technique because of two reasons: high solubility and the diffusion rate of carbon in these metals at high temperature [26].

1.3 Polymer composite

Electrically conductive polymers have a wide range of applications in many fields such as electronic, photovoltaics, energy, and aerospace industries. There are many conducting polymers such as polyacetylene or poly(p-phenylene) doped with iodine (I_2) or arsenic pentaflouride (AsF_5), which makes polymer composites electrically conductive and has a vast variety of applications. Conductive polymer composites are composed with insulating and conducting heterogeneous materials and electrical conductivity can be tailored to suit desired applications. The conducting phase could be stainless steel fibers, copper-coated graphite, or carbon particles in a micrometer scale. In recent times, scientists are interested in composite materials incorporated with conducting nano-scale fillers such as carbon nanotubes, and nanoparticles of silver, copper or gold. A nano-scale filler is defined as a material that has a dimension at least less than one hundred nanometers (100 nm) in size. These fillers have substantial advantage over the micro-scale fillers due to their high surface-to-mass ratio and aspect ratio.

Carbon nanotubes play an important role as a nano-scale filler with unique mechanical, transport, and electromechanical properties. A carbon nanotube incorporated polymer matrix results in a composite with significantly enhanced mechanical and transport

properties with potential applications in many fields, for example, electromagnetic interference shielding (EMI), electrostatic dissipation, and photovoltaic devices. CNT considerably enhances the electrical conductivity of a composite by making a CNT network within a polymer matrix without affecting other properties. Electrical conductivity of nanotubes change under mechanical stress [27], consequently, this phenomenon can be employed to monitor stress distribution and devising the composite for strain sensing.

A CNT-polymer composite as a resistance strain provides a range of advantages over conventional strain gauges, explicitly, its higher strain sensitivity and long-lasting mechanical properties. Its novel and advanced applications in the civil engineering, aerospace industry, or bio-mechanical field are promising and exciting. The development of the next generation of CNT-polymer composite for strain sensor has some major drawbacks, mainly understanding the physics of the composite at a nano-scale, the relationship between structure and properties, the integrity and interaction of the components at the interface, and the role of nanomaterials in enhancing the properties of the composites. Therefore, the strain sensor based on a carbon nanotube-polymer composite is empirical with a wide range of questions to be answered.

1.4 Type of sensors based on carbon nanotube-polymer composite

The devices that measure or sense physical or chemical features such as temperature, pressure, concentration, etc. are called sensors. Sensors convert this detected feature into an electrical signal. To manufacture a sensor commercially, it should have high sensitivity, responsive time, and reliability. Further, the production cost should be low

and easily amenable to mass production. Sensors have been used in different industries such as construction, manufacturing, aerospace, medical and environmental monitoring, and so on. The advanced technology experienced by current society demands enhanced safety and structural integrity of health facilities, as well as eco-friendly systems. This has paved the way for researchers around the globe to develop new technologies and sensing materials. Nanotechnology along with the new generation of materials like carbon nanotubes can be considered as the perfect way to achieve low cost, light weight, and macro/micro/nano scale sensors. The array of sensors that can be developed by employing CNTs as the sensing material is vast and only a few of them are strain, stress, pressure, chemical, biological, optical sensors [28].

1.5 Objectives of the study

A complete understanding of resistivity and strain sensing properties of a nanocomposite requires profound understanding of the role of each composite component in determining the electrical conductivity and mechanical properties. This requirement can be met by investigating the behavior and characteristic of the components at the nano-scale. Studies regarding the strain sensing properties of carbon nanotube-polymer composites are limited to factors such as experimental observation of the resistivity, the effect of polymer types, and fabrication methods. Experimental studies to explore the composite at nano-scale have not been sufficiently addressed. In this dissertation, the growth conditions of carbon nanotube based on chemical vapor deposition (CVD) technique have been optimized in terms of temperature, thickness of catalyst layer, plasma treatment time, and gas (H_2, CH_4, Ar) flow rates. According to the experimental studies, Ni, Fe, Co and Mo are considered most suitable catalysts for CVD technique.

Furthermore, hydrocarbon such as methane (CH_4) and acetylene (C_2H_2) or carbon monoxide (CO) are most suitable precursor gases while H_2, Ar act as carrier gases. Secondly, carbon nanotube-polymer composite films were synthesized using wet chemistry techniques with different conditions to optimize the conductivity and mechanical properties.

Therefore, the main objectives of this study are:

1. Grow a carbon nanotube forest on an Si wafer for synthesizing CNTs film-polymer hybrid films
2. Synthesize CNTs-polymer composite films
3. Estimate the individual parameters such as resistance and capacitance of these films with different carbon nanotube loading, effects of the individual parameters' values to the overall composite piezo-resistivity, and contribution of the cross-linkers on mechanical properties of the films
4. Characterizing these films using various *ex situ* characterization techniques to understand the structural, chemical, and electrical properties
5. Fabricate and test a novel design of strain sensor based on these films

A literature survey of CNTs-polymer composite, sample preparation, characterization results of structural, chemical and electrical properties of these films along with discussion and conclusions are presented in the following chapters.

CHAPTER 2

LITERATURE SURVEY OF CARBON NANOTUBE-POLYMER COMPOSITES

In this chapter, a review of the present literature on carbon nanotube-polymer composite and strain sensors based on carbon nanotube is presented.

2.1 Carbon nanotube-polymer composite

Carbon nanotube-polymer composite is made up of a polymer matrix and carbon nanotube as the filler. Because of its nanometer size and high aspect ratio, nanotubes have high surface energy and a tendency for agglomeration. For example, single-wall CNTs (SWCNTs) exist as bundles or rope to minimize the surface energy of individual tubes [29]. A homogenous dispersion of CNTs in the polymer matrix can be achieved by separating aggregates, or bundling. To achieve an electrical conductivity composite, a three-dimensionally connected network of CNTs is preferred. The remaining major challenge is to develop a reproducible dispersion technique for CNTs in a polymer matrix.

2.1.1 Dispersion of CNTs and synthesizing CNT-polymer composite

The key factors governing CNTs dispersion in polymers are morphology and attractive forces between nanotubes [29]-[31]. The high surface energy, aspect ratio, and flexibility enhance CNTs entanglements. Further, it shows a strong tendency for aggregation due to van der Waals forces. For practical applications, carbon nanotubes should be dispersed in

a polymer matrix; therefore, these cohesive forces must be overcome. Many techniques have been employed in determining effective ways for disaggregation. Effective disaggregation is critical for enhancing the desired properties of the composite. There are many literature papers based on the techniques that overcome the van der Waals forces, suggesting dispersion and disaggregation are accomplished by sonication [32] [33], shear mixing [34] or extrusion [35].The most widespread technique is sonication [33], which has been found that the resulting localized heating and the cavitation forces support in separating the tubes from each other. Cavitation forces also lead to shorten and degrade the nanotubes [36]. Several research groups have carried out studies based on the effect of sonication as sonication time and frequency. Most of the time, mild sonication conditions have been applied (low power, short time) in a presence of a surfactant [37]; or a solvent that shows some degree of interaction with the nanotubes which lead to disaggregation. Hence, the composite is synthesized by either mixing the dispersion of nanotubes with a polymer solution, in-situ polymerization in the nanotube dispersion, or coagulation [38] - [46]. Non-covalent interaction can be observed between carbon nanotube and some polymers such as polyphthalamide (PPA), polyvinylpyrrolidone (PVP), and polyphenyl ethers (PPE). In some cases, it is believed that nanotube-polymer interaction arises due to π-π stacking, which is enough to affect dispersion and stability of nanotubes in polymer matrix.

2.2 Electrical conductivity of CNT-polymer composite

Extensive theoretical and experimental studies have been done on electrical conductivity of CNT-polymer composites during the last two decades [47] - [54]. Experimentally, the electrical behavior of a CNT-polymer composite is characterized by using either DC

resistance or AC impedance techniques on bulk or thin film samples. In the following paragraph, a brief assessment of DC, AC conductivities and mechanism of electrical conductivity of composite is described.

2.2.1 Direct current (DC) conductivity

In this case, direct current signal (I, in amperes (A)) is passed into sample and the subsequent potential drop (V, in volts (V)) across a thickness or length of the sample is determined. Ohm's law states potential difference across two points of a conductor is directly proportional to the current flowing through the two points and the resistance (R, in ohms (Ω)) is given by,

$$V = I \times R \quad \ldots\ldots\ldots\ldots\ldots\ldots\ldots\ldots\ldots\ldots\ldots\ldots\ldots\ldots\ldots\ldots\ldots\ldots\ldots\ldots\ldots\ldots\ldots\ldots\ldots\ldots\ldots\ldots \quad (9)$$

Where, I- current through the conductor, V- potential drop across the conductor, R- resistance of the conductor.

Here, resistance depends on the intrinsic resistivity (ρ), length (L) and cross sectional area (A) of material which current passes through.

$$R = \rho \frac{L}{A} \quad \ldots\ldots\ldots\ldots\ldots\ldots\ldots\ldots\ldots\ldots\ldots\ldots\ldots\ldots\ldots\ldots\ldots\ldots\ldots\ldots\ldots\ldots\ldots\ldots\ldots\ldots\ldots\ldots\ldots\ldots\ldots\ldots \quad (10)$$

DC resistance can be used to determine the volume (ρ_{vr}) or surface resistivity (ρ_{sr}). Volume resistivity is a measure of the leakage current directly through the material. Surface resistivity is the electrical resistance on the sample surface of an insulator. Figure 9 and Figure 10 show the experimental setup for volume and surface resistivity respectively [55]. Volume or surface resistivity can be determined based on the area (A)

or distance (L) between the electrodes, thickness (t) or width (w) of the sample, applied voltage (V), and measured current (I) across the samples [55].

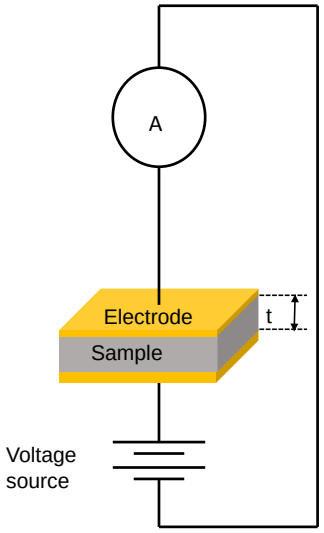

Figure 9. Experimental setup for measuring volume resistivity. (Adopted from Njuguna et al. **[56]**)

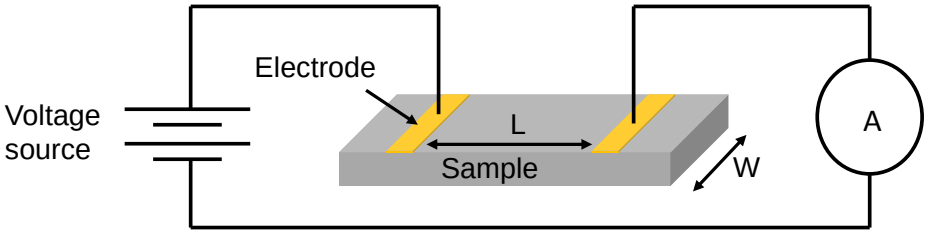

Figure 10. Experimental setup for measuring surface resistivity. (Adopted from Njuguna et al. **[56]**)

$$\boldsymbol{\rho_{vr}} = \frac{VA}{It} \quad \ldots \qquad (11)$$

or

$$\rho_{sr} = \frac{Vw}{IL} \dots\dots\dots\dots\dots\dots\dots\dots\dots\dots\dots\dots\dots\dots\dots\dots\dots\dots\dots\dots\dots\dots\dots\dots\dots\dots\dots. \qquad (12)$$

From equation (11) and (12) the electrical conductivity σ can be obtained. Electrical behavior of the composite can be evaluated by a plot of conductivity against the CNT mass fraction (or volume). An insulator-to-conductor transition of carbon nanotube-polymer composites occurs as the mass (or volume) fraction of CNT is increased. This transition can be interpreted as a three-stage process as shown in Figure 11. In the low CNT weight fraction (region I), the composite maintains its insulating phase, because none of nanotube clusters form a percolating network and the distance between tubes is way outside the limit of critical 'tunneling distance' ($D>D_t$). As the weight fraction of nanotube increases, a few nanotube clusters or individual nanotubes begin to form a percolating network. At this point (in region II), inter-tube distance is less than the critical tunneling distance which gives rise to a sharp increase in conductivity. This region is called the percolation region and the weight fraction at this point where the composite is transitioning from an insulator to a conductor is called the percolation threshold, ψ_c. Nanocomposite becomes highly conductive at a high CNT mass fraction due to formation of multiple percolating networks (referring to path 1, 2, and 3 in Figure 11). In this region, nanotubes are almost touching each other and conductivity of the composite reaches its maximum value [56]. The electrical conductivity of the composite can be described as a filler mass fraction by power law function of the form [56];

$$\sigma \propto (\phi - \phi_c)^t \dots\dots\dots\dots\dots\dots\dots\dots\dots\dots\dots\dots\dots\dots\dots\dots\dots\dots\dots\dots\dots\dots\dots\dots\dots \qquad (13)$$

Where, ϕ_c – percolation concentration, t- critical component. The percolation concentration and critical component can be determined by fitting the power law function

to the conductivity-mass (or volume) fraction data. Percolation concentration signifies the filler extent at the point where transition from insulator to conductor occurs. Critical exponent represents the dimensionality of the percolation network under consideration (For 3D system, t~2) [56].

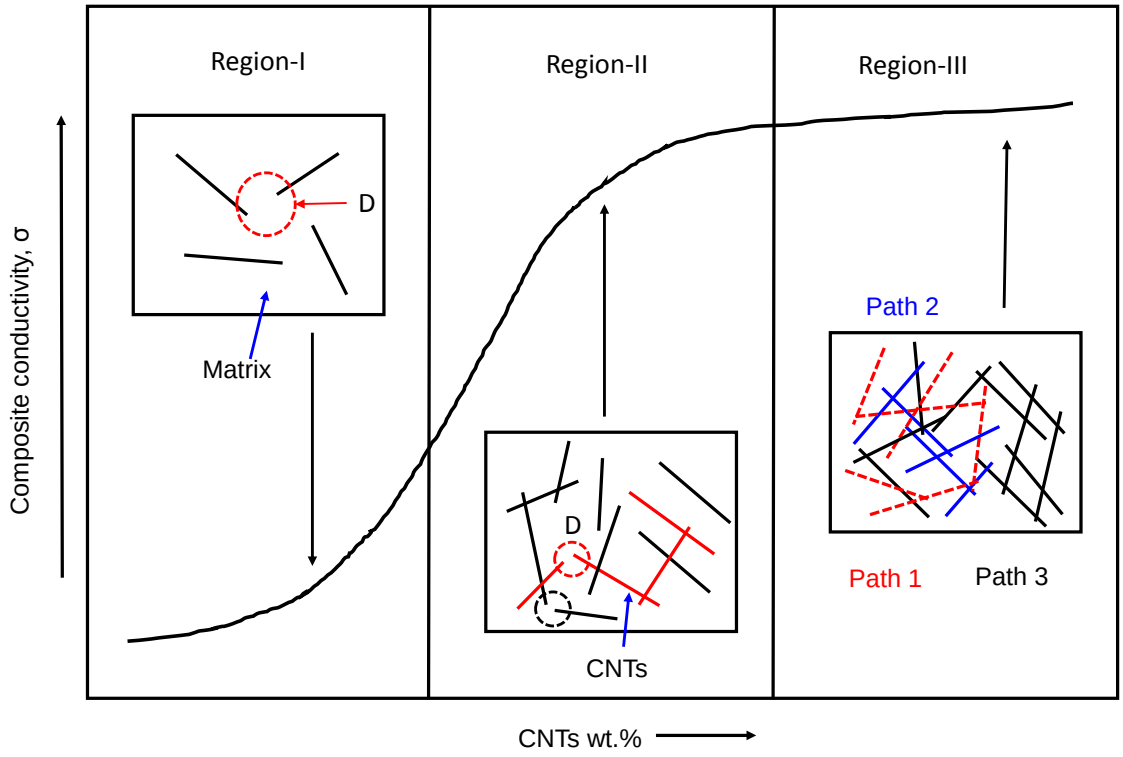

Figure 11. Variation of electrical conductivity and evolution of percolating networks as CNT wt.% increases. (Adopted from Njuguna et al. **[56]**)

2.2.2 Alternating current (AC) conductivity

In an alternating current conductivity measurement, electric current reverses its direction periodically. Electrical impedance (Z) is a measurement of opposition to the alternating current circuits, describing not only the relative amplitudes of the voltage and current, but

also relative phases. In this case, Ohm's law can be written by including total impedance in the circuit.

$$I = \frac{V}{Z} \quad (14)$$

Impedance can be determined by applying an AC voltage to a sample and measuring current through the sample. The resultant alternating current signal can be analyzed as a sum of sinusoidal function (a Fourier series). An applied alternating voltage signal can be expressed as a function of time,

$$V_t = V_o \sin(\omega t) \quad (15)$$

V_t- potential at time t, V_o- amplitude of the signal and ω – radial frequency (radians/second). The relationship between ω and frequency (f) (in hertz (Hz)) of the signal is given by,

$$\omega = 2\pi f \quad (16)$$

The resultant signal I_t has a phase shift (ϕ) and amplitude I_o,

$$I_t = I_o \sin(\omega t + \phi) \quad (17)$$

Therefore, impedance of the circuit can be determined based on Ohm's law.

$$Z = \frac{V_t}{I_t} = \frac{V_o \sin(\omega t)}{I_o \sin(\omega t + \phi)} = Z_o \frac{\sin(\omega t)}{\sin(\omega t + \phi)} \quad (18)$$

AC impedance measurements are obtained at range of different frequencies as a function of CNTs mass fraction. AC conductivity measurements are suitable for evaluating electrical properties of high resistance materials and therefore the experimental setup shown in Figure 10 can be used.

2.3 Mechanism of electrical conductivity

Generally, there are two distinct regions in AC conductivity variation with frequency. At low nanotube weight fraction, conductivity increases with frequency while at high nanotube weight fraction; AC conductivity is independent from the AC frequency [39] [57] [58]. DC conductivity of the composite follows percolation behavior described in equation (13). AC conductivity at low nanotube weight fraction shows some deviation and a good agreement at high nanotube weight fraction. The difference in AC and DC conductivity at low nanotube weight fraction can be explained by a hopping conduction mechanism. DC conductivity is restricted by the maximum of the range of activation energies as a carrier hops through the sample while AC conductivity is restricted by the highest barrier experienced as the charge carrier travels for one half period of the field [39]. For low weight fraction, just above the percolation threshold, AC conductivity is more favorable than DC conductivity throughout the entire network as a large energy barrier can be avoided. This may result in higher AC conductivity. Frequency dependence electrical properties of CNT-polymer composites have been studied by Kim et al. [57]. At the low frequency domain, dielectric relaxation similar to the pure epoxy was observed and in the vicinity of the percolation threshold another relaxation peak was observed in the electric modulus plot attributed to interfacial relaxation. Further, peak height of the loss tangent spectra was found to increase and move to higher frequency as CNT mass fraction increased, indicating an enhancement of conducting paths. Kilbride et al. [39], Kim et al. [57], and Berger et al. [59] studies found that AC conductivity at a high frequency scaled after a certain characteristic frequency (ω_0) based on the power law of the form,

$\sigma(\omega) \propto \omega^s$ ……(19)

with s= 0.92 [39] and s=0.66 [57] , indicating a universal character of AC conductivity which was further confirmed by both studies of AC conductivity versus frequency data, where data was falling into a single curve. The approximate power law with 0.8<s<1.0 was characteristic of hopping in a disordered material, where hopping charge carriers are subjected to a randomly varying energy barrier. The dominant transport mechanism is governed by a hopping of charge carriers according to the above studies. Although the value of s= 0.92 for PVA/MWCNT falls within the 0.8<s<1.0 range no 's' value was obtained for PmPV/MWCNT in the same study by Kilbride and co-workers [39]. Further, Kim et al. [57] who studied epoxy/SWCNT composite obtained a lower value for exponent 's' and a variation of this exponent is not well explained. Further study is required to address these gaps for better understanding of the electrical conductivity in polymer-CNT composites.

2.4 Carbon nanotube-Polymer composite strain sensors

As discussed in the introduction, carbon nanotube and carbon nanotube-polymer composites have been used to develop different types of strain sensors based on characteristic resistivity. In this section, a review of strain sensors fabricated using carbon nanotube-polymer composites and their characteristics is summarized. Resistivity can be defined as the change in electrical resistance of a material to the original resistance when subjected to an external strain, i.e., $\frac{\Delta R}{R_o}$. Here, ΔR- change in resistance at a given strain and R_o is the original resistance of the material. The terms like "gauge factor", "sensor

sensitivity", and "sensitivity factor" are used to express the sensor performance. Gauge factor (K) is defined as the ratio of piezoresistivity to the applied axial strain ε,

$$K = \frac{\Delta R/R_o}{\varepsilon} \ldots\ldots\ldots\ldots\ldots\ldots\ldots\ldots\ldots\ldots\ldots\ldots \tag{20}$$

Up till now, carbon nanotube-polymer composite strain sensors based on single-wall CNTs [60]-[63] and multi-wall CNTs [61] [64]-[74]. The different types of polymers under consideration for strain sensor development include poly(methyl methacrylate) [61] [68], epoxy resin [64]-[66], polypropylene [75], polysulfone [70], polystyrene [76], poly(dimethyl-siloxane) [62] [67], and polyethylene oxide [69]. These carbon nanotube-polymer composites were characterized in static loading situations for both tensile and compressive strains as well as dynamic loading situations. As shown in **Table 1**, the gauge factor of the sensor depends on different factors such as diversity of nanotubes, polymer matrix, fabrication techniques, and characterization techniques.

Table 1: Gauge factors of CNT-based strain sensors

Type of sensor	**Ref.**	**Gauge factor (K)**
SWCNT films	[61] [77]	7
MWCNT films	[78] [79]	2-3.76, 0.3482
SWCNT/polymer	[61] [62] [63]	1-5, 2-2.5, 0.1-1.8
MWCNT/polymer	[64] [65] [68] [80]	3.2-22.4(tension) and 2.1-7.1 (compression) 5-8 (dry blended) and 1-15 (solution casting) 0.01-1.25 3.2-4.3(tension) and 4.4-5.8 (compression)

2.5 Origin of piezo-resistivity

The basic property related to the sensor sensitivity is change of resistance to the applied strain. Piezo-resistivity witnessed in the strain sensors fabricated from CNT-polymer

composite can be attributed by the variation of conductive networks in composite, such as a tunneling effect in neighboring CNTs due to variation of the inter-tube distance [65] , loss of contact between nanotubes [68], and conductivity change of CNT due to deformation [61] [64] [81].

Tunneling effect is the major driving force in piezoresistivity compared to other mechanisms mentioned above [65]. This phenomenon was found to dominate when the inter-tube distance is less than 1.8 nm [52]. N. Hu et al. [65] developed the theoretical model using "Simmons theory" [82] for the tunneling resistance to handle both tensile and compressive strains. He considered CNTs as "hard-core" objects so that CNTs cannot penetrate into each other. The tunneling resistance between two adjacent CNTs can be estimated by the following equation. A schematic diagram of tunneling effect in composite is shown in Figure 12.

$$R_{tunnel} = \frac{V}{AJ} = \frac{h^2 d}{Ae^2\sqrt{2m\lambda}} \exp\left(\frac{4\pi d}{h}\sqrt{2m\lambda}\right) \ldots\ldots\ldots\ldots\ldots\ldots\ldots\ldots\ldots\ldots\ldots\ldots\ldots \quad (21)$$

Where, J- tunneling current density, V-potential difference, e- electron charge, m-mass of

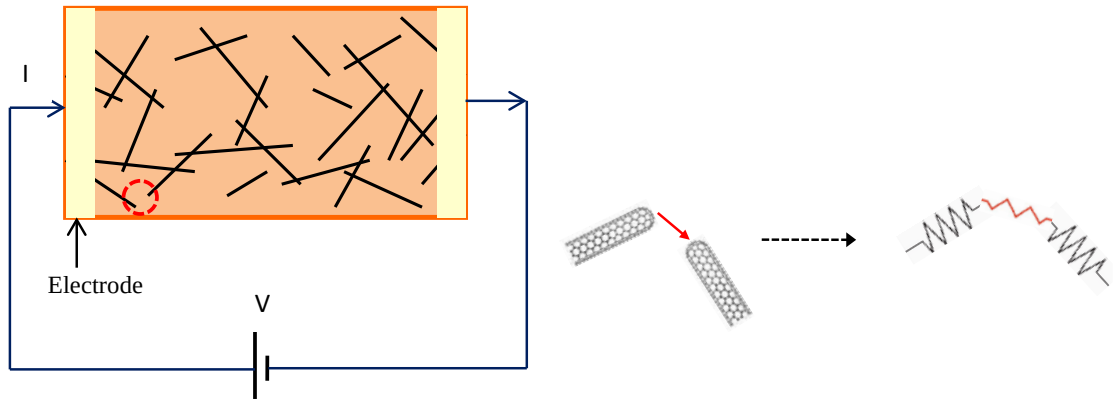

Figure 12. Schematic view of CNT conductive network including tunneling effect. (Adopted from Hu et al. **[65]**)

an electron, h-Planck's constant, d-distance between CNTs, λ-potential barrier for polymer, A- cross sectional area of tunnel (~ cross sectional area of CNT).

According to equation (21), the tunneling resistance increases exponentially with distance which was supported by the experimental findings that nonlinear piezo-resistivity increases in exponential form with increasing CNT concentration [65]-[71] [80]. These results explicitly indicate the dominant role of tunneling resistance plays in determining the piezo-resistivity of CNT-polymer composite sensors.

CHAPTER 3

EXPERIMENTAL TECHNIQUES

3.1 Thin film deposition process by Physical Vapor Deposition (PVD)

The PVD process can be divided into two categories: (1) sputtering and (2) thermal evaporation.

Sputtering: When a solid surface is bombarded with high energy particles such as Argon or Krypton (chemically inert heavy gas), surface atoms of the solid surface are ejected due to the collision between the surface atom and the high energy particles as shown in Figure 13. This phenomenon is called sputtering or cathode sputtering.

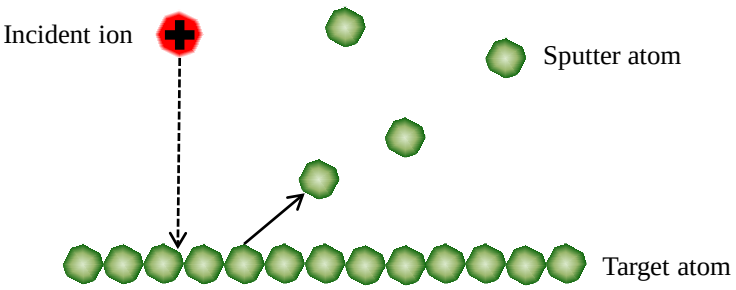

Figure 13. The physical sputtering process.

Cathode sputtering can be used for thin films deposition. There are several techniques that have been developed for thin film deposition such as dc diode, magnetron, rf diode and ion-beam sputtering [83]. The dc diode sputtering system is the simplest among these systems. This system consists of a pair of electrodes. One electrode is a cold

cathode and the other is an anode. The target material to be deposited can be placed on the cathode surface, and the substrate can be placed on the anode. The sputtering chamber contains sputtering gas, typically argon or krypton gas at 10^{-3} Torr range. A glow discharge can be created by applying a dc voltage between two electrodes. The gas ions generated in the glow discharge are accelerated towards cathode and sputter the target, resulting in the deposition of a thin film on the substrate. In this system, the target should be composed of metals since the glow discharge (current flow) is continued between electrodes.

Magnetron Sputtering: In this system [84]-[86], a magnetic field is applied on the cathode as shown in Figure 14. The electron in the glow discharge is moving in cycloidal

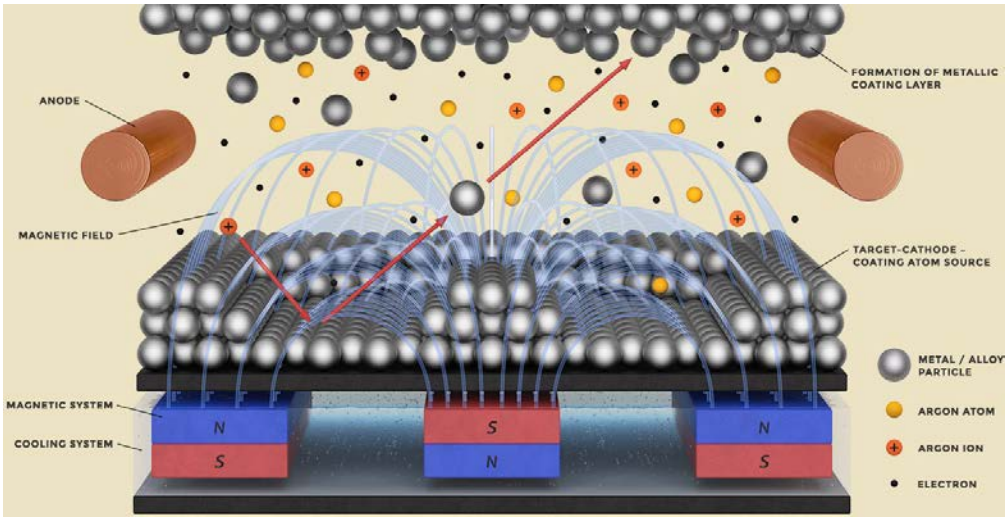

Figure 14. Magnetic field is superposed on the cathode. (Picture courtesy: http://farotex.com)

path and the orbit of an electron drift in the direction of $\boldsymbol{E} \times \boldsymbol{B}$ with velocity E/B, where **E** and **B** represent the electric filed between electrode and transverse magnetic field respectively. Due to the orientation of the magnetic field, the drift path of the electron

forms a closed loop and lead to an electron-trapping effect. The electron-trapping effect enhances the collision between electrons and sputtering gas. The magnetic field enhances the plasma density at the cathode, which leads to higher current density, effectively enhancing the sputtering rate at the target. Due to low gas pressure, the sputtered particles navigate through discharge space without collision, which results in higher deposition rate.

There are two types of magnetron sputtering system available for a thin-film deposition. One is a cylindrical type [87] and the other one is a planar type [88]. In planar magnetron, the magnetic flux terminated on the cathode surface to magnetic core [86] is called a *balanced* magnetron. A system with additional magnetic flux superposed to the balanced magnetron is called an *unbalanced* magnetron [86]. In a balanced magnetron system, some electrons are escaped from the magnetic field without taking part in ionizing gas molecules. These escaping electrons are trapped by the excess magnetic flux of unbalanced magnetron system and make electrons ionizing the sputtering gas. Due to his process, secondary plasma is generated at the close to substrate which leads to enhancing the flux of ionized particles. This ionized flux modifies the film-growing process similar to ion-assisted deposition [89].

Figure 15 shows a schematic diagram of a sputter deposition system. Figure 16 shows the actual picture of the PVD system used to deposit Ni catalyst layers on the Si substrate.

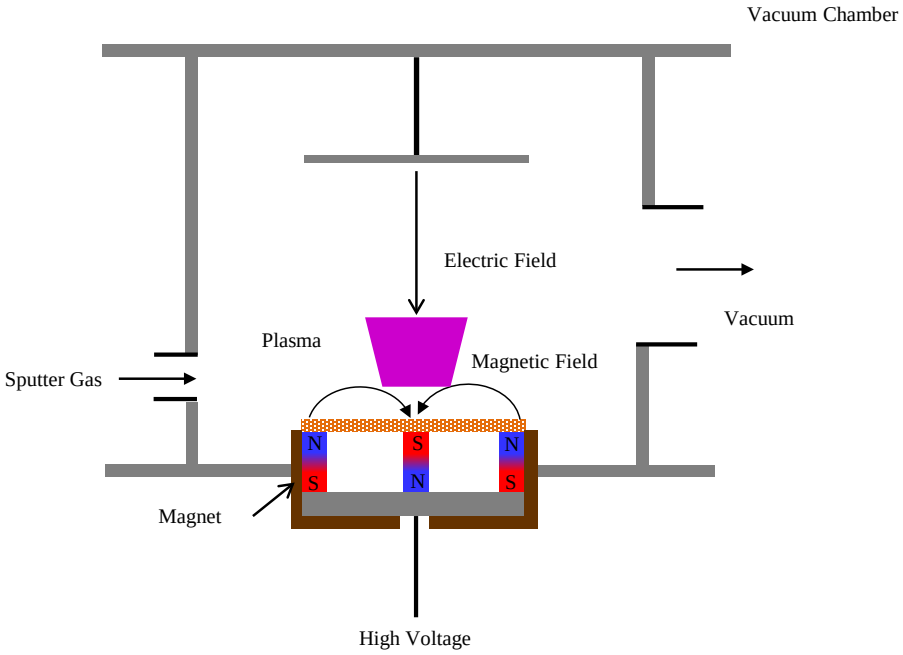

Figure 15. Schematic diagram of sputter deposition system.

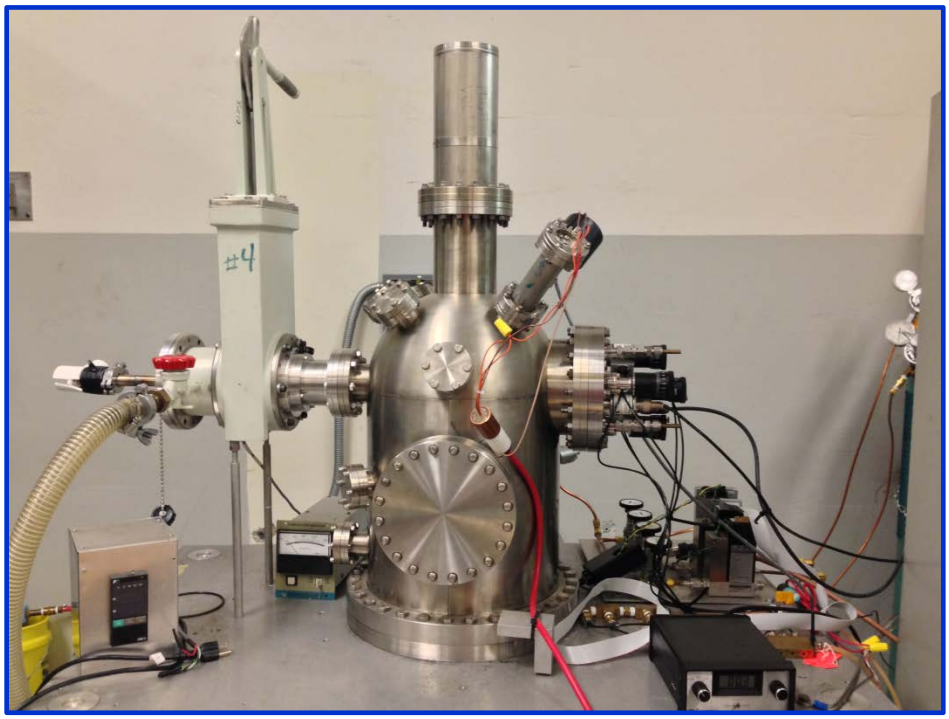

Figure 16. Picture of the physical vapor deposition chamber used for the deposition of Ni catalyst thin films.

3.2 Chemical Vapor Deposition (CVD) process

Chemical vapor deposition process identifies thin solid films deposition techniques on a substrate by a *chemical reaction* of vapor-phase precursors. Therefore, this technique can be distinguished from a physical vapor deposition process. The chemical reactions of precursors take place in the gas phase as well as on the substrate. Precursor reaction can be initiated by heat (thermal CVD), plasma (plasma enhanced CVD), or higher frequency radiation such as UV (photo assisted CVD) [90]- [92].

Plasma Enhanced Chemical Vapor Deposition Process (PECVD): Chemical reactions in CVD are thermodynamically endothermic. This factor becomes an advantage since reactions can be controlled by maintaining the amount of input energy. This means external energy has to supply to the precursor to initiate the chemical reaction. Generally, heat is used as the source of energy to initiate and control the CVD process. But for the high quality thin films with acceptable growth rate, high deposition temperature is required. Generally, to activate the CVD process, the energy of the plasma and photons is widely used. If plasma or photons energy is used, thin film deposition can be done under much milder thermal condition.

Chemical reaction can be initiated by plasmas based on two basic steps. First, to form chemically active species that can be used for thin film formation as a result of dissociation of precursor molecules by inelastic collision with energetic particles formed in plasma. Second, supply the energy to substrate surface to enhance the surface processes such as particle migration, nucleation, and heterogeneous kinetics. The

composition, structure, electrical, and mechanical properties of the thin films will be determined by the plasma parameters.

Many techniques have been developed for generating plasmas, but electrical discharges in gaseous media are ideal [93] [94]. One of the main factors to use plasma as an energy source for CVD process is to overcome high deposition temperatures. Further, electrical discharges present in the gaseous media that form non-thermal plasmas have been used. Plasma enhanced CVD (PECVD) has been used since the 1960s for synthesizing of dielectric films at low temperatures. Industrial PECVD systems have been developed with most of them based on non-thermal plasmas sustained by radiofrequency (RF) or microwave source (MW). The PECVD process is exceptionally complex and the mechanisms of reaction are poorly understood. Despite the hundreds of papers on the study of the PECVD, the detailed mechanism of the deposition is still not clear. Several reviews and books summarize the chemistry of PECVD processes, as well as the physics of plasma [95]-[97].

Further, the journal *Chemical Vapor Deposition* has been committed to developments in traditional PECVD [98]. Figure 17 shows the schematic diagram of plasma enhanced chemical vapor deposition reactor.

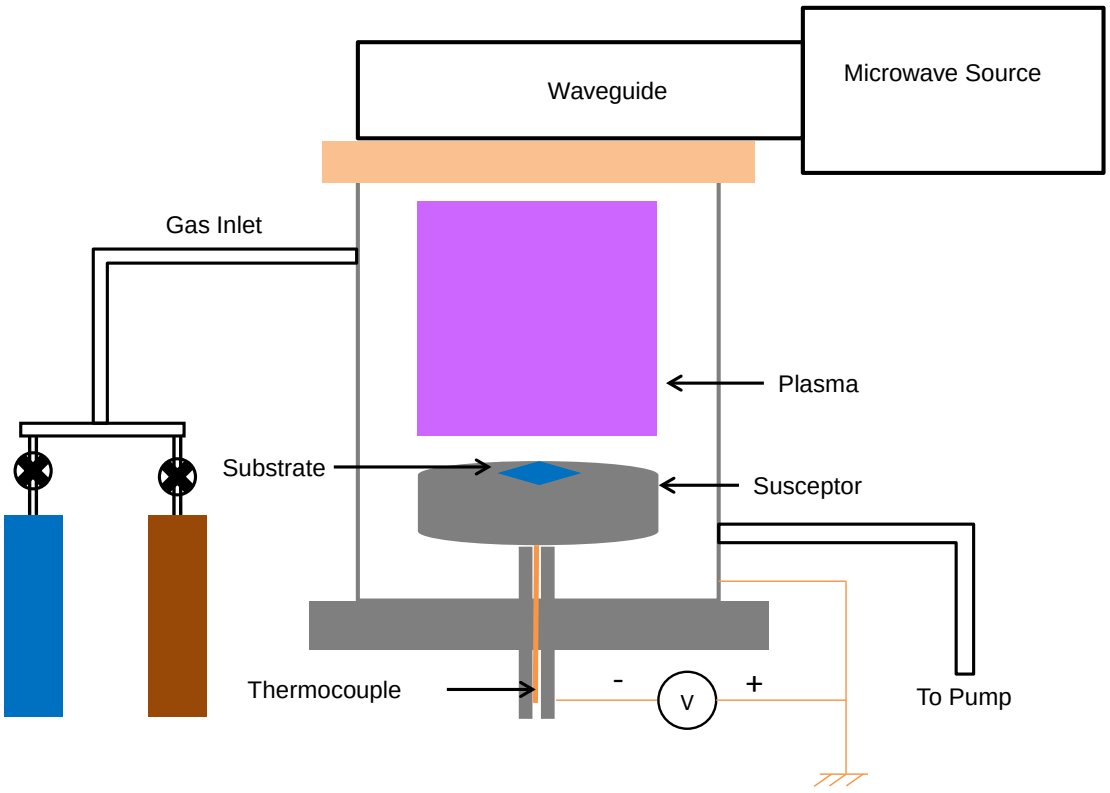

Figure 17. Schematic of microwave plasma enhanced chemical vapor deposition reactor.

CVD Process: CVD processes are involved in highly complex gas-phase and surface reactions. The presence of a hot layer of gas just above the substrate is a significant feature of the process. This layer is termed as a “boundary layer” and the pressures gas phase pyrolysis reaction happening in the layer plays an important role in the CVD film deposition process. The basic pyrolysis steps involved in an overall CVD process is illustrated in Figure 18, which includes important steps [92]:

1. Transport of precursors in the bulk gas flow region into the reactor
2. Producing reactive and intermediates and gaseous by-products from gas phase reactions of precursors in the reaction zone
3. Transport of reactants to the substrate surface
4. Adsorption of the reactants on the substrate surface
5. Surface diffusion for growing sites, nucleation, and surface chemical reactions for film growth
6. Desorption and transport of residual of the decomposition away from the reaction zone.

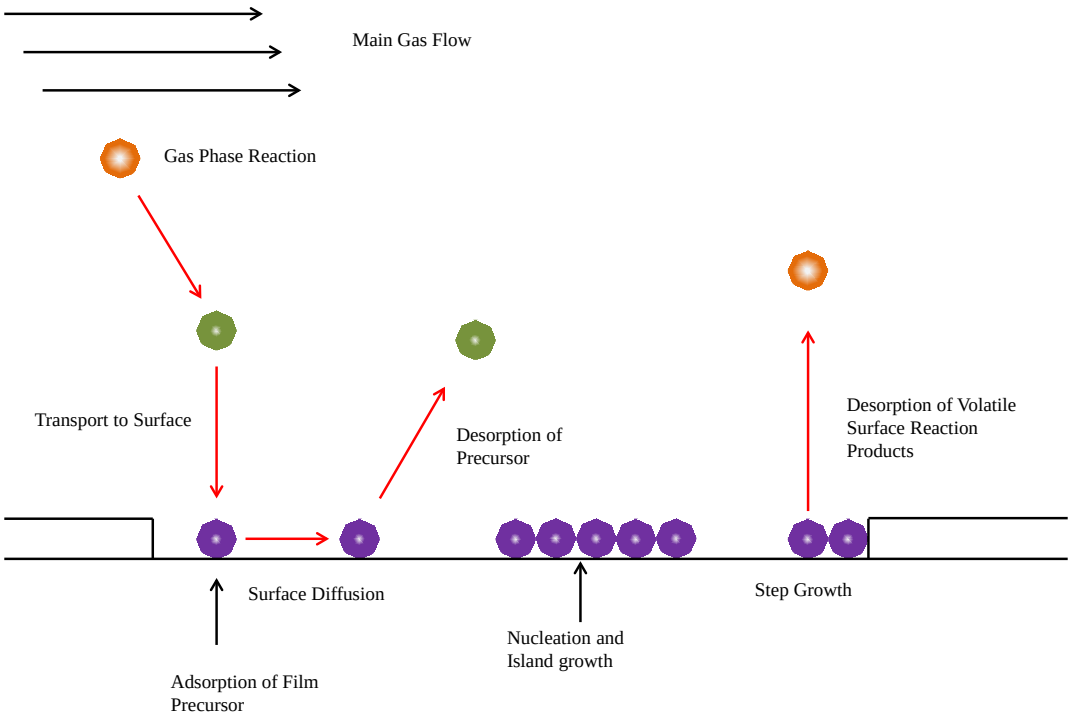

Figure 18. Precursor transport and reaction process in CVD. (Adopted from Jones et al. **[92]**)

In the conventional thermal CVD process, the film growth depends on several parameters, such as temperature of the substrate, operating pressure of the reactor, and composition and chemistry of the gas phase.

A picture of the chemical vapor deposition chamber used for the plasma treatment and the carbon nanotube growth is shown in the Figure 19.

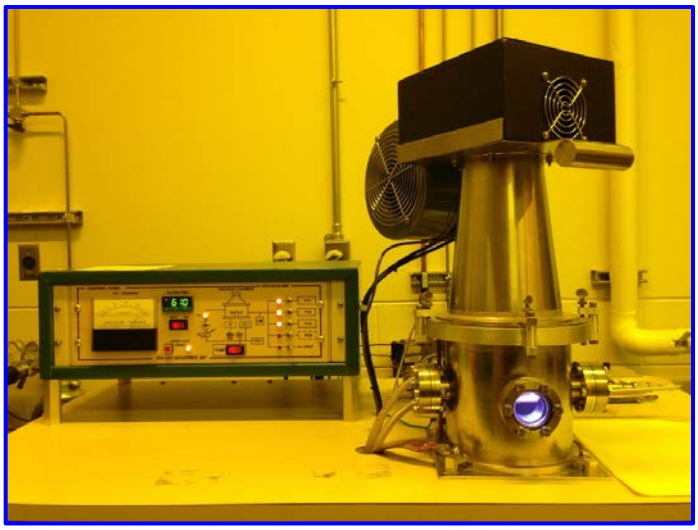

Figure 19. A picture of the CVD system used for CNTs growth.

3.3 Plasma treatment

Plasma surface treatment is considered as a technique that raises surface energy of material to improve the bonding characteristics. This process is used to treat materials such as polymer, glass, papers or even metals. Plasma technology consists of a different purpose for surface treatment such as cleaning, printing, electronic packaging etc. Plasma technology is comprehensively used in automobile and aircraft industry.

Plasma is considered as a fourth chemical state of mater. When sufficient energy is supplied to each state, it changes from solid to liquid and from liquid to gas in sequence. If additional energy is supplied into the system in the gas phase, then the gas becomes ionized and reaches the plasma state. The plasma state consists of ions (positive or negative), electrons, and radical and neutral atoms (or molecules). When plasma comes into contact with the material surface it transfers additional energy from plasma to the material surface for subsequent reactions to take place on the surface. The altered surface properties are ideal for printing, electronic packaging, or adhesive bonding.

Ultra-violet (UV)/ Ozone (O_3) plasma treatment (UVO): During this process, hydrocarbon contaminants on the surface are excited and/or dissociated by the absorption of short-wavelength UV radiation. At the same time, atomic oxygen is generated when molecular oxygen is dissociated by 184.9 nm UV radiation. This atomic oxygen is combined with an oxygen molecule to synthesize ozone molecules which are subsequently dissociated by 253.7 nm UV radiation. The products of excited and/or dissociated contaminant molecules react with atomic (high energy) oxygen to form volatile molecules which desorb from the surface. Radical such as *OH, COO*, and CO* are also formed on the surface. Oxidation of the surface is responsible for the increase in the polar groups which is directly related to the adhesion properties of the material surface.

3.4 Spin coating

Spin coating from a solution is a common technique to produce a thin uniform film on a substrate. In this process, few drops of solution are drop casted on the substrate and the

substrate is accelerated speedily to the desired rotation speed (revolutions per minute). Solution flows radially, owing to the centrifugal force and excess liquid is driven out off the edge of the substrate. The film further thins slowly until disintegrating pressure effects cause the film to reach an equilibrium thickness or until it turns dense, due to a rise in viscosity from solvent evaporation. Final thinning of the film is due to solvent evaporation [99].

3.5 Rutherford Backscattering Spectrometry (RBS)

Ion beam backscattering spectrometry has been extensively used for analysis of materials for elemental identification, stoichiometry, film thickness, and impurity distribution just below the interface. The fundamentals of ion scattering in solids can be explained by classical mechanics, i.e., elastic scattering of a particle by another particle. The energy E_1 of particles backscattered from a surface atom is related to the incident energy E_0 through the principles of conservation of energy and momentum as following equation [100] [101] [102].

$$\frac{E_1}{E_0} = K = \left[\frac{(M_2^2 - M_1^2 sin^2\theta)^{1/2} + M_1 cos\theta}{M_1 + M_2}\right]^2 \quad \ldots\ldots\ldots\ldots\ldots\ldots\ldots\ldots\ldots\ldots\ldots\ldots \quad (22)$$

Where K is known as kinematic factor, M_1 and M_2 are the masses of the incident and target particles, respectively, and θ is the laboratory angle toward which the incident ion is scattered. Based on equation (22), the best energy separation and mass resolution can be obtained for light target atoms, however for the heavy elements mass resolution fading out. To overcome low mass resolution for heavy elements, high incident energy or a heavier projectile can be used. The Rutherford cross section (σ) is another important

parameter in ion beam scattering. The cross section characterizes the probability of collision between the incident ion and target atom and contributes to the signal amplitude of the backscattering spectrum. The cross section can be defined as the following equation [100]-[102].

$$\sigma(E_0,\theta) = \left(\frac{Z_1 Z_2 e^2}{4E_0}\right)^2 . \frac{4\left[(M_2^2 - M_1^2 \sin^2\theta)^{1/2} + M_2 \cos\theta\right]^2}{M_2 \sin^4\theta (M_2^2 - M_1^2 \sin^2\theta)^{1/2}} \ldots\ldots\ldots\ldots\ldots\ldots\ldots \quad (23)$$

Where Z_1 and Z_2 are the atomic numbers of the incident and target atoms, respectively. According to the above equation, the cross section is very high for heavier elements and detecting a light atom in a heavy element matrix is difficult due to the substantial change in the signal amplitude [103]. Further, the cross section is inversely proportional to the square of initial energy E_0 and for $E_0 > 0.5$ MeV, the scattering cross section does not change significantly as a function of energy. When the energetic ions penetrate into solid material, ions lose energy basically due to electronic interactions with target atom. The rate of the amount of energy (*dE*) lost per distance (*dx*) traversed is called stopping power (*dE/dx*). The stopping cross section $\left(\varepsilon = \frac{1}{N}\left(\frac{dE}{dx}\right)\right)$ can be defined as the ratio between the stopping power and the areal density (N) of the target material within distance *dx*. Since stopping cross sections for many materials have been established as a function of energy, the film thickness can be determined. The energy spread of incident ions due to statistical fluctuations in the number of collision processes is called *energy straggling*. This process is important for bulk materials; for thin films measurements this can be neglected. The ion scattering technique involving elastic and inelastic scattering can be divided into three aspects: (1) low-energy, (2) medium-energy, and (3) high-energy ion scattering. The

Rutherford backscattering technique (RBS) falls into the high-energy ion scattering section. RBS is employed to study the stoichiometry, structure, and thickness of thin films. RBS was used in this study to characterize the thin films grown by the PVD system. Typically, incident ions with energies ranging from 0.5 MeV to 4.0 MeV are used in RBS. In this energy range, the scattering cross section is Rutherford. The energy of the backscattered ions depends on the target atom and the backscattering yield is related to the number of target atoms, and the film thickness can be determined from the width of the peaks in RBS spectrum. The RBS spectrum can be obtained in two different geometries: IBM and Cornell as shown in Figure 20. In IBM geometry places incident beam, exit beam, and surface normal all in the same plane with,

$$\alpha + \beta + \theta = 180^\circ \quad \ldots\ldots\ldots\ldots\ldots\ldots\ldots\ldots\ldots\ldots \quad (24)$$

Where α, β, and θ are incident, exit, and scattering angles respectively. While Cornell geometry is a three-dimensional scattering geometry in which incident beam, exit beam, and rotation axis of the samples are in the same plane and can be described in terms of angle β by equation,

$$\cos\beta = -\cos\alpha\cos\theta \quad \ldots\ldots\ldots\ldots\ldots\ldots\ldots\ldots\ldots\ldots \quad (25)$$

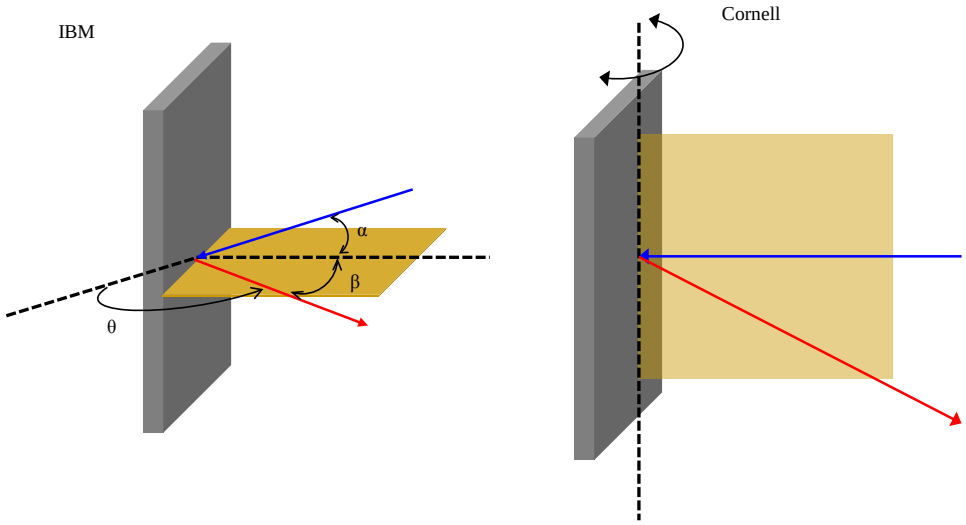

Figure 20. Left: IBM geometry; Right: Cornell geometry. Geometry is dependent on the placement of the detector with respect to the target and incident beam direction.

IBM geometry compromises a simple setup and complicated Cornell geometry has the advantage of a large scattering angle, which optimizes mass resolution, and grazing an incident and exit angle, which optimizes depth resolution. In this study, RBS measurements of nickel (Ni) thin films on silicon (Si) substrate were carried out in a tandem Van de Graaff accelerator in the physics department at Western Michigan University [104]. The backscattering spectra of 2.0 MeV He^{+} ion beam were collected using a silicon surface barrier detector at a scattering angle of 150°. The experimental RBS data was simulated and analyzed using the SIMNRA program [105] [106]. SIMNRA is used mainly for simulation of Rutherford, non-Rutherford cross sections, or nuclear reactions and calculation of electronic stopping powers or energy loss straggling for any ion-target combination with any scattering geometry including transmission

geometry. The film thickness and compositions are calculated by fitting the experimental data by means of the simplex algorithm.

Figure 21 shows the picture of the 6 million volts tandem Van de Graaff accelerator at the Western Michigan University, Department of Physics used for Rutherford backscattering spectrometry.

Figure 21. 6 million volts tandem Van de Graaff accelerator.

3.6 X-ray Diffraction (XRD)

X-rays are electromagnetic (EM) waves with typically shorter wavelength on the order of 1Å ($1*10^{-10}$m). The interaction of X-rays with materials leads to diffraction of coherent and incoherent scattering [107]. X-ray diffraction consists of measuring the intensity and the angle of scattered X-rays from electrons bound to atoms as a function of atomic position. Waves scattered by atoms at different positions and angles depend on the atomic

or molecular species and geometry of the crystal lattice. Therefore, scattered X-rays can be used in phase analysis, determination of crystalline structure, and epitaxial orientation, measurement of film thickness and interfacial roughness, determination of texture, residual stress in films, grain size, and lattice parameters [107]-[109]. The utilizing of scattered X-rays from material to investigate properties mentioned above is called X-ray diffraction (XRD). The following review is the most important and basic result to understand the geometry of diffraction from crystals. Classical EM-waves can be described as a sine wave that has periodicity every 2π radians. The spatial length of each period is called wavelength λ. If two matching waves are not coincident, they have a *phase shift* with respect to each other. This phase shift can be measured in two ways: (1) as a liner shift Δ on a length scale, or (2) as a phase shift, $\delta\phi$ on an angular scale as follows,

$$\frac{\Delta}{\lambda} = \frac{\delta\phi}{2\pi} \rightarrow \delta\phi = \frac{2\pi}{\lambda}\Delta \ldots\ldots\ldots\ldots\ldots\ldots\ldots\ldots\ldots\ldots\ldots\ldots\ldots\ldots\ldots\ldots\ldots\ldots\ldots\ldots\ldots\ldots\ldots\ldots\ldots\ldots \quad (26)$$

The structural information in crystal diffraction can be obtained through the Bragg equation. In Bragg law, X-ray diffraction is explained in terms of the reflection of X-rays by sets of lattice planes, called crystallographic planes, characterized by triplet index *hkl*. These parallel crystallographic planes are equally spaced and separated by distance d_{hkl}. Bragg law considers X-rays as being reflected by a lattice plane similar to a surface of a mirror. Since all X-rays are reflected in the same direction, interference can be observed. Figure 22 shows that the second wave travels a longer distance PN and NQ before and after reflection occurs respectively. If Δ= PN+NQ is multiple $n = 0, \pm 1, \pm 2, \ldots$ of the wavelength λ, then constructive interference occurs.

$$\Delta = n\lambda \quad (27)$$

If the diffracted waves are out of phase i.e., $\Delta = n\lambda/2$, they interfere destructively. The sharp constructive interference intensity emerged based on Bragg law in terms of X-ray wavelength (λ), angle of incidence (θ) and the inter-planer distance (d), as given below [110] [111],

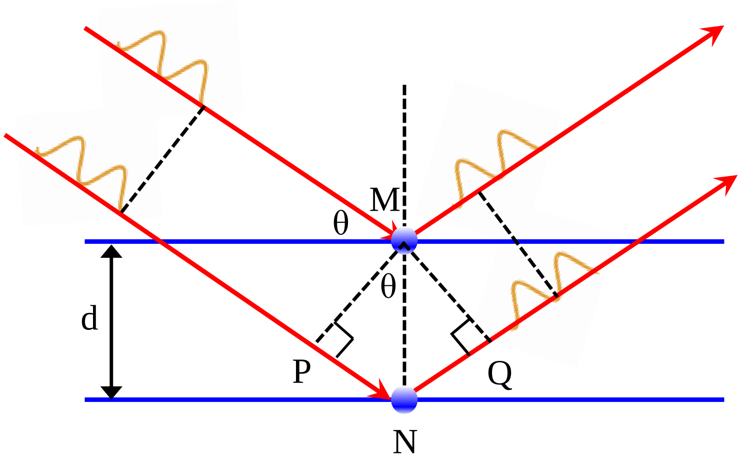

Figure 22. A schematic diagram of the geometry used for derivation of Bragg's law.

$$n\lambda = 2d\sin\theta \quad (28)$$

Depending on the atomic arrangement, crystalline phase and orientation of the samples the peaks can be observed in the XRD pattern if Bragg law satisfied [109]. The extracted information from the XRD pattern depends on the position, intensity, and the profile of the diffraction peaks. The peak positions tell about the translation symmetry, namely geometry, orientation, d-spacing, and lattice parameters of the unit cell. The peak intensity provides the information about electron density inside the unit cell, which means the location of the atoms in the unit cell. The peak profile and width provide the

information on crystallite size, defects, and strain. The crystallite size can be determined from Scherrer formula [112] [113].

XRD is a non-destructive bulk technique for analyzing a wide range of materials from research to industry [103].Further, XRD measurement can be used to investigate the dynamic process such as phase transition, crystallite growth, and thermal expansion. XRD is especially important to understand the growth and characterization of thin film material. For example, high-resolution X-ray diffraction can be used to determine the lattice parameters (both in-plane and out-of-plane) of an epitaxial layer with great precision. The polycrystalline materials can be study by glancing-incidence X-ray diffraction (GIXRD) technique. The thickness of a thin film and interface roughness between two films can be determined by X-ray Reflectivity (XRR) measurements and modeling for multilayer structures.

In GIXRD configuration, the detector is scanned by the diffracted beam asymmetrically over a 2θ range of interest while the incident X-ray beam is fixed at a small angle (~5°). Under this configuration, epitaxial thin films and the single crystal substrate cannot be detected since the Bragg condition is not satisfied. This technique is used to verify the presence of polycrystalline material.

Thin-layered films play an important role in advanced technologies. Single-layer or multi-layer structures can be found in all aspects of research and development. Therefore, there is a growing requirement to accurately characterize these thin films. Determination of layer thickness, interface roughness, and layer density are important to analyze and control the synthesizing parameters. Thus, XRR is the prevailing and non-destructive

technique to characterize thin films. Below the critical angle of total internal reflection, X-rays penetrate only few nanometers (2-5nm) into the film. Above the critical angle, penetration depth (probing depth) increases rapidly. A minimum layer thickness of 1nm and density changes of ~1-2% can be measured under optimum sample conditions.

In this study, GIXRD measurements were performed using Philips X'pert multi-purpose diffractometer shown in Figure 23, operating at 45 kV and 40mA with ceramic X-ray tube with Cu anode ($K\alpha_1$=0.154056 nm). This instrument consists with two beam paths: focusing and parallel beam optics. The focusing optics consist of programmable divergence, anti-scatter and receiving slits; incident and diffracted beam soller slits; a curved, graphite-diffracted beam monochromator; and a proportional counter detector. The principle application of this setup is phase analysis of powder samples. The parallel beam optics consists of a Göbel mirror combined with a 0.27 radian parallel plate collimator; flat, graphite-diffracted beam monochromator; and proportional counter detector. The principal applications of this parallel beam setup include phase analysis of polycrystalline thin films and XRR. For GIXRD measurements, the step size 0.04° was used for the diffraction angle in the 2θ-ω scan with a scan time of about 24 s for each step in a 2θ range of 10-100° while keeping the ω fixed at 5°. The XRD pattern was analyzed by JADE 8.5 and PDF4+ database from ICSD. The lattice parameters of Ni thin films were calculated by JADE pseudo-Voigt profile function using the respective diffraction peaks in the 2θ-ω scan [114]. For XRR measurements, the step size 0.005° was used for the diffraction angle in the ω-2θ scan with a scan time of about 20 s for each step in a 2θ range of 0.1-5.0°. XRR patterns were simulated using BEDE software.

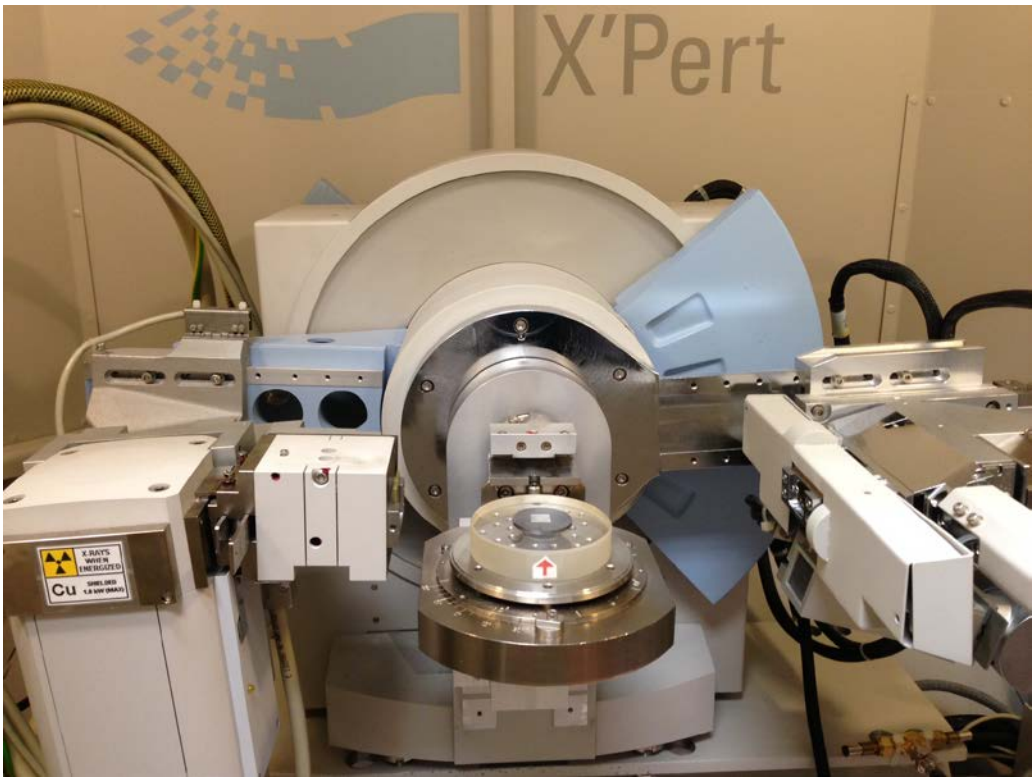

Figure 23. The Philips X'pert multi-purpose diffractometer, which is used for the x-ray diffraction measurements of Ni thin films.

3.7 X-ray Photoelectron Spectroscopy (XPS)

A solid material interacts with its surrounding by its surface. The nature of the interactions with its surrounding depends on the physical and chemical composition of these surfaces. Therefore, *surfaces* influence many crucial properties of the solid. Regardless of the importance of the surface, the proportion of the atoms of solids that can be found at the surface is very small. To detect impurities at a surface at a concentration of 1%, materials at a concentration level of one part per billion (1ppb) need to be detected within the solid. Therefore, a successful technique for analyzing surfaces must be extremely sensitive and efficient at filtering out signal from the majority of the atoms in the sample [103] [115]-[117]. X-ray photoelectron spectroscopy (XPS) has the required

characteristic to become the leading technique for understanding the chemical properties of materials. The basic principle of XPS is based on the photoelectric effect discovered by Hertz in 1887 [116] [118] and extended to surface analysis. XPS is used for quantitative analysis of the surface chemical state and to detect all elements except hydrogen and helium. XPS makes use of soft X-rays, normally Mg Kα (1253.6 eV with a line width ~0.7 eV) or Al Kα (1486.6 eV with a line width ~ 0.85 eV), which are generated by bombarding the Al or Mg anode with high energy electrons (with energies ranging from 15-150 keV) in the X-ray gun [116]. The photoemission process can be initiated by bombarding the samples with the monoenergetic X-rays originated from the electron gun. Schematic representation of the photoemission is shown in Figure 24.

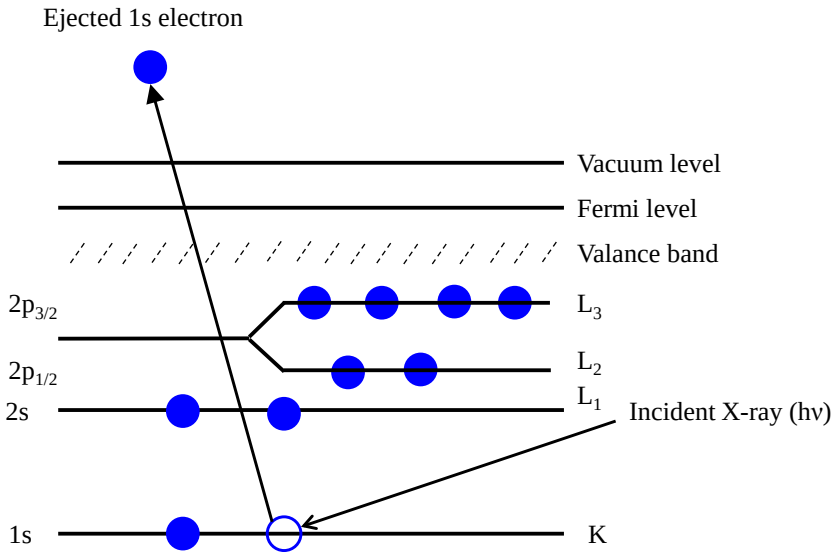

Figure 24. Schematic diagram of the photoemission in XPS process, showing photoionization of an atom by excitation and ejection of an electron from 1s level.

In XPS, a special form of photoemission occurs (i.e., an electron from a core level is ejected by an X-ray photon energy hν). The energy of the ejected electron is analyzed by the electron spectrometer. The kinetic energy (KE) of the ejected electron is the experimental quantity measured by the spectrometer; on the other hand, kinetic energy depends on the energy of the X-ray photon employed to probe the sample. Therefore, kinetic energy is not an intrinsic material property. The binding energy (BE) of the electron is the important parameter that recognizes the electron precisely, in terms of its parent element and atomic energy level. Binding energy can be determined using kinetic energy, energy of the incident X-ray photon (hν), and the work function of the spectrometer (ϕ_s) using following equation [116].

$$BE = h\nu - KE - \phi_s \ldots\ldots\ldots\ldots\ldots\ldots\ldots\ldots\ldots\ldots\ldots\ldots\ldots\ldots\ldots\ldots\ldots\ldots\ldots\ldots\ldots\ldots\ldots\ldots\ldots\ldots. \quad (29)$$

Even though incident X-ray photons penetrate few microns deep into the samples, XPS is surface-sensitive due to the short path length of photoelectrons [119]. In general, photo electrons with kinetic energy varies from 300 to 1500 eV are used for XPS analysis. Because of the short path length of photoelectrons, the distance the electron can travel without inelastic scattering is in the range of 0.5-3 nm or 3-8 atomic layers [120]-[122]. The intensity of the photoelectron decays below the surface. Only electrons without inelastic energy loss leave the bulk, making the practical limit about 8-10 nm for determining non-destructive composition as a function of depth analysis [121]. Those electrons which are excited and escape without out inelastic energy loss contribute to the characteristic photoelectron peaks or spectral lines as a function of binding energy in the spectrum. Those which undergo inelastic scattering and suffer energy loss appear as spectral background in the spectrum. Small variations in the binding energies of the

photoelectron lines or Auger lines, satellite peaks and multiple splitting appear in photoelectron peaks can be used to identify chemical state of elements.

A depth profiling technique can be used to reveal subsurface information by sputtering the samples with ion guns and appropriate ion such as Ar^+ or Xe^+. Combining a sequence of ion gun etch cycles with XPS analyses provides quantified information as well as layer thicknesses. Because of chemical degradation of sensitive materials, use of energetic ions for etching may be inappropriate. To overcome this setback, the angle resolved X-ray photoelectron spectroscopy can be used, as it provides a non-destructive depth profile near the subsurface. Angle-resolved XPS is performed by tilting the samples with respect to the photoelectron analyzer, i.e., changing the angle between the axis of the electron analyzer and the normal to the sample surface.

In this study, AXIS Ultra DLD XPS system from Kratos Analytical in Figure 25 was used to collect data which consist of a dual anode (Mg and Al Kα) X-ray source with high power monochromators and 180° hemispherical analyzer. The X-ray beam is incident to the sample at an angle of 45° off normal, and the emitted photoelectrons were collected at normal to the samples. There were two different modes for collecting data called *survey* and *high resolution*. In the survey scan, the sample was scanned over a wide range of binding energy (0-1500 eV) for identification and quantification of elements or to identify any contaminants on the sample surface. The high resolution scans were collected within a smaller energy window by selecting photoelectron peaks in the survey scans to study the chemical state of the element corresponding to the photoelectron peak selected. The depth profiles were collected by sputtering with 2kV Ar^+ ion rastered over 3*3 mm^2 areas of the samples.

Figure 25. AXIS Ultra DLD XPS system from Kratos Analytical for the x-ray photoelectron spectroscopy measurements of thin films**.**

3.8 Raman spectroscopy

Raman spectroscopy is a one of the most sophisticated spectroscopic techniques available to study vibration and rotational modes in an atomic, a molecular, or a bulk system [103] [123]-[125]. The technique is based on a specific form of inelastic scattering of monochromatic light [126]-[130]. A laser operating in visible, infrared, or ultraviolet region can be used as a monochromatic light source. When light (photons) interact with matter, phonons or some other kind of excitations in the system make the photon energy shift (gain or lose). Energy shift has information about vibrations or rotations modes of the system. Basically a sample is exposed to a laser beam and light from the illuminated point is accumulated using a lens and sent to a monochromator. Rayleigh scattering

(elastic scattering) photons are sifted out while inelastic (Raman) photons are diverting to a detector.

The Raman scattering signal is very weak, because of insufficient inelastic photons. To overcome this difficulty, Raman spectrometers used to have holographic grating and multiple dispersion stages to get a high degree of laser elimination for Rayleigh photons. Photomultipliers used to be the detector for Raman spectrometers. Modern Raman spectrometers utilize edge filters for laser illumination and CCD detectors. There are many special types of Raman spectroscopic techniques used in research and industry due to its very high sensitivity to bonds and their variations. For example, non-linear Raman, time resolved Raman (TR^2), matrix-isolation Raman, high pressure Raman, surface-enhanced Raman (SERS), Raman spectroelectrochemistry, Raman microscopy and Fourier transform Raman (FT-Raman). Figure 26 (a) represents the line diagram of a Raman microscope showing a light source, optical components to direct light, the sample, a monochromator to separate parts of the optical spectrum and a CCD detector. Figure 26 (b) shows the actual picture of the Raman microscope used to collect Raman spectra.

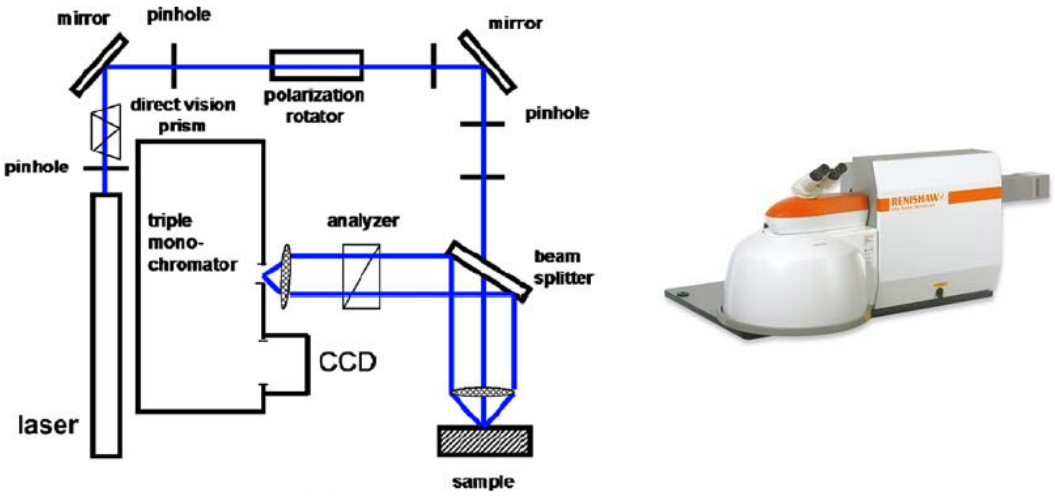

(a) (b)

Figure 26. (a) Schematic diagram of Raman spectrometer. (Reproduced with the permission of the copyright owner **[103]**) (b) RENISHAW inVia Raman microscope.

When a molecule is exposed to light, the interactions take place between the electron cloud and bond of the molecule. Photons excite the molecule from the ground state to a higher virtual energy state. The molecule relaxes these photons and comes back to different vibrational or rotational modes. The energy difference between the new and initial states makes the frequency of emitted photons different than laser frequency. If a molecule returns to a higher energy level than original, the frequency of emitted photon shifts to a lower frequency region. The shift of frequency to a lower region is designated as *Stokes shift*. If a new energy level is less energetic than original, emitted photons will have a higher frequency. The frequency shift to a higher region is designated as *anti-Stokes shift*. The Raman effect takes place due to the change of molecular polarization (amount of deformation of electron cloud) with respect to vibrational coordinates. If a molecule has a higher polarizability, Raman intensity will be higher. In Raman

spectroscopy, the sample is shined by a laser beam in the UV-visible frequency ν_0 and the scattered photons are detected in perpendicular direction to the incident beam as shown in Figure 27. The Rayleigh scattered photons are very intense and have the same frequency as the incident beam ν_0 and Raman scattering, which has weak intensity and two different frequencies indicated by $\nu_0 - \nu_m$ and $\nu_0 + \nu_m$. The frequency ν_m is the vibrational frequency of the molecule. The $\nu_0 + \nu_m$ and $\nu_0 - \nu_m$ lines are designated as the Stokes and anti-Stokes line respectively. In Raman spectroscopy, it is customary to plot the photon intensity versus vibrational frequency as a shift from the incident beam frequency (ν_0). Figure 28 shows the energy levels and transitions that are responsible for Rayleigh, Stokes, and anti-Stokes scattering.

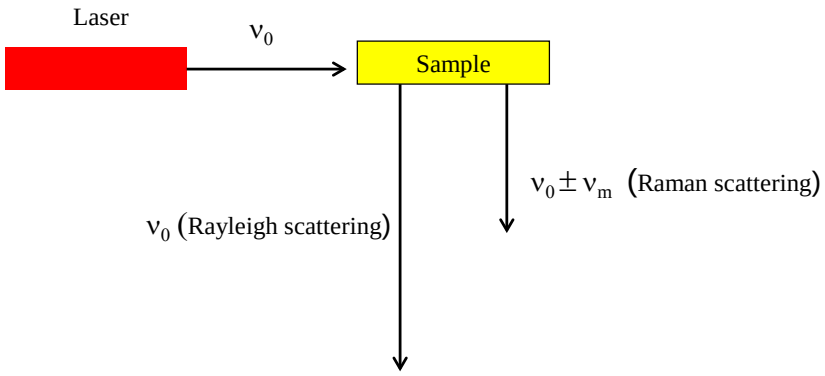

Figure 27. Mechanism of Raman spectroscopy. (Adopted from Ferraro et al. **[123]**)

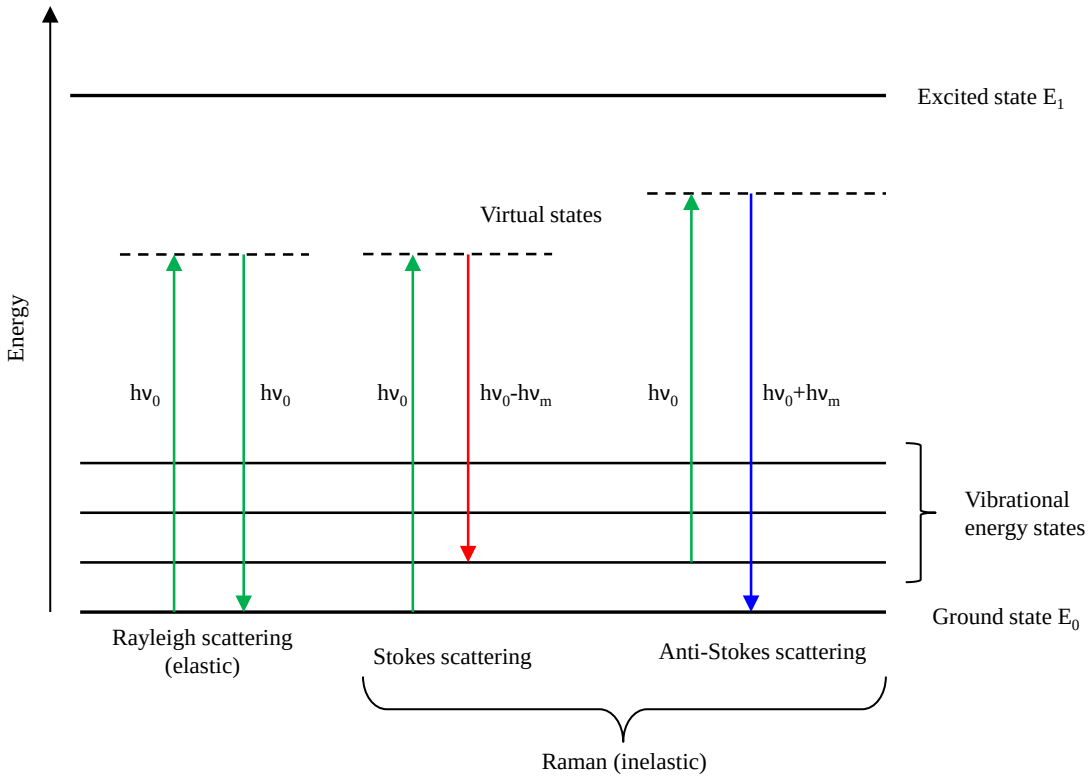

Figure 28. Comparison of energy levels for Rayleigh, Stokes and anti-Stokes scattering.

Raman scattering can be explained by classical theory. Electromagnetic (EM) wave (laser beam) consists of two components, electric (E) and magnetic (B) components. The electric field is responsible for almost all the excitations in a molecule. The electric field is time (t) dependent.

$$E = E_o \cos(2\pi \nu_o t) \quad \text{(30)}$$

Where, E_0– maximum amplitude of the electric field,ν_0 – frequency of the laser beam. When laser beam interacts with a molecule, an electric dipole moment (P) is induced. Dipole moment is defined as below.

$$P = \alpha E = \alpha E_o \cos(2\pi \nu_o t) \quad \text{(31)}$$

$\alpha -$ Polarizability

Molecule has a frequency v_m and the nuclear displacement q is given by,

$$q = q_o \cos(2\pi\, v_m t) \ldots\ldots\ldots\ldots\ldots\ldots\ldots\ldots\ldots\ldots\ldots\ldots \qquad (32)$$

Where, $q_0 -$ vibrational amplitude

For small vibrations, α is linearly depends on q. Therefore, α can be expressed as,

$$\alpha = \alpha_o + \left(\frac{\partial \alpha}{\partial q}\right)_o q + \cdots \ \ldots\ldots\ldots\ldots\ldots\ldots\ldots\ldots\ldots\ldots\ldots. \qquad (33)$$

$\alpha_0 -$ Polarizability at the equilibrium and $\left(\frac{\partial \alpha}{\partial q}\right)_o -$ rate of change of α with respect to q, evaluated at the equilibrium.

From equation (31), (32) and (33),

$$P = \alpha_o E_o \cos(2\pi\, v_o t) + \frac{1}{2}\left(\frac{\partial \alpha}{\partial q}\right)_o q_o E_o [\cos\{2\pi(v_o + v_m)t\} + \cos\{2\pi(v_o - v_m)t\}] \ (34)$$

According to equation (34), $\alpha_o E_o \cos(2\pi\, v_o t)$ indicates an oscillating dipole which radiates light of frequency v_0 (Rayleigh scattering) while the second term is a clear indication of Stokes $(v_o - v_m)$ and anti-Stokes $(v_o + v_m)$ Raman scattering. The vibrations will not show as Raman active if $\left(\frac{\partial \alpha}{\partial q}\right)_o$ is zero. Therefore, for a molecule to be Raman active, the polarizability (α) must be changed with nuclear displacement (q).

In experiments, the frequency v_0 of the laser beam is chosen so that its energy is distant from the first excited state. The signals from the Stokes line (S) are much stronger than the anti-Stokes lines (A), because the population of particles at the ground state is greater

than vibrational states (Maxwell- Boltzmann distribution law). Since both lines (Stokes and anti-Stokes) give the same information about vibrational state of molecules, it is habitual to measure the Stokes side of the spectrum.

In this experiment, Raman spectra were collected using RENISHAW inVia Raman microscope with green laser (wavelength 514 nm) in the frequency range 100-3000 cm^{-1} at 10% of laser power. Further, exposure time was 10s and 4-10 accumulations were employed in each scan.

3.9 Energy Dispersive X-ray Spectroscopy (EDS)

Energy dispersive X-ray spectroscopy is an ideal technique to characterize the elemental composition of a particular specimen [131]. EDS is based on detecting the characteristic X-rays produced by elements after irradiating a specimen with a high energy electron beam. The electrons interact with atoms in the specimen in different ways. When an electron strikes an atom, an electron originally from an inner shell (K shell) is ejected. The atom returns to its lowest energy state, when this “vacancy” is filled by an electron from higher energy level in the atom. In doing so, the high energy electron releases some of its energy in the form of X-rays. As a result, the amount of energy released is precisely equal to the energy difference between the two energy levels as shown in Figure 29. Further, electrons at the other higher energy levels can occupy the vacancy by releasing different amounts of energy. As a consequence, a specimen will emit X-rays at different energies. For example, L-shell electrons emit Kα X-rays and M-shell electrons emit Kβ X-rays. Since, L to K transition is the most probable; the intensity of the Kα radiation is higher than the Kβ radiation. All elements except hydrogen and helium

produce characteristic X-rays. The EDS data were collected using Philips XL30 FEG instrument.

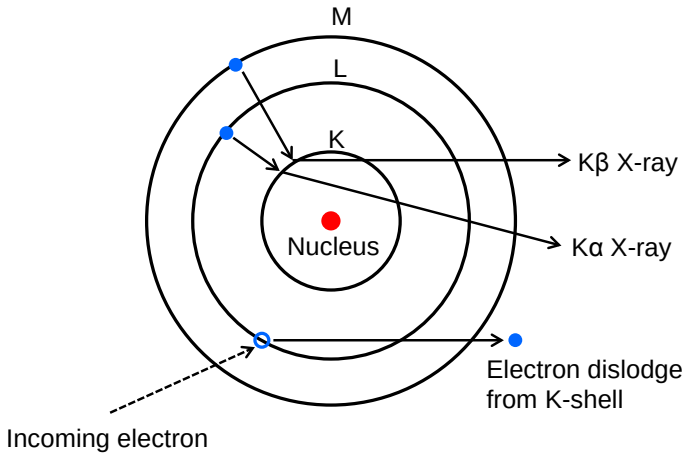

Figure 29. Schematic diagram of origin of characteristic X-rays. (Adopted from Heath et al. **[131]**)

3.10 Electrical conductivity measurements

Following the synthesizing and characterizing CNT-polymer composite thin films, the electrical conductivity of these thin films was measured by Van der Pauw technique and four probe method combined with impedance spectroscopy. The importance of the Van der Pauw, four probe methods and impedance spectroscopy in the surface electrical conductivity measurements of CNT-polymer composite thin films will be briefly discussed in this section.

3.10.1 Van der Pauw method

In 1958, L. J. Van der Pauw developed a technique for determining the resistivity or Hall effect of arbitrary shaped semi-conductor samples [132]. In order for the Van der Pauw technique to work, the structure must be homogenous, isotropic, and free of any isolated

holes. Further, these structures consist of uniform and negligible thickness compared to other area of the structure. More importantly, four ohmic contacts placed far apart from each other on the perimeter of the structure can be used to carry out the measurements and be much smaller than the area of the structure. The contacts must be small as possible and leads connecting the contacts should be of the same material as contacts to minimize thermoelectric effects. When the aforementioned conditions are met, the following relation holds, referring to the experimental configuration shown in Figure 30.

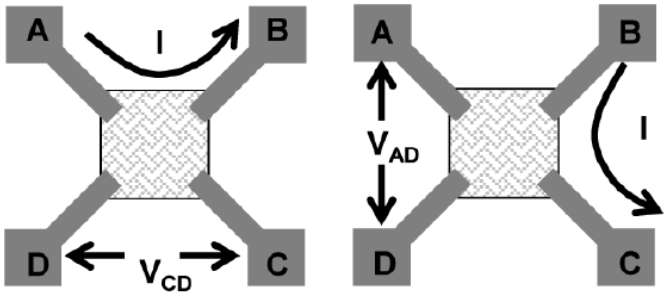

Figure 30. A Van der Pauw configuration, which can be used to measure the sheet resistance (or resistivity) of the sample. (Reproduced with the permission of the copyright owner **[133]**)

$$e^{-\left(\pi\frac{dR_{AB,CD}}{\rho}\right)}+e^{-\left(\pi\frac{dR_{BC,AD}}{\rho}\right)}=1 \ldots\ldots\ldots\ldots\ldots\ldots\ldots\ldots\ldots\ldots\ldots\ldots\ldots\ldots\ldots\ldots\ldots\ldots\ldots\ldots. \qquad (35)$$

Where, $R_{AB,CD}$ is the resistance of the structure when current is forced through contacts A and exits contact B, and voltage is measured across contact C-D. $R_{BC,AD}$ is the resistance of the structure when a current is forced through contact B and exits contact C, and voltage is measured across A-D. d is the thickness of the structure. ρ is the resistivity of the material. Therefore, the resistivity of the sample is given by the Van der Pauw equation, if the sample possesses a line of symmetry, $R_{AB,CD} = R_{BC,AD} = R$

$$\rho = \frac{\pi d R}{ln2} \dots\dots\dots\dots\dots\dots\dots\dots\dots\dots\dots\dots\dots\dots\dots\dots\dots\dots\dots\dots\dots\dots\dots\dots\dots\dots\dots\dots\dots\dots\dots \quad (36)$$

According to this equation, if the structure is known to be homogeneous and perfectly symmetrical, the resistivity can be calculated using the sample thickness (d) and resistance (R) by forcing the one current and make one differential voltage measurement.

3.10.2 Impedance spectroscopy

Impedance spectroscopy (IS) or ac impedance method initially applied in determination of double layer capacitance and in ac polarography [134] [135]. Currently, it is used to characterize electrode process and complex interfaces [136] [137]. IS studies are based on the systems which respond to the periodic small amplitude ac potential signal and then measure the current through the system. The measurements are carried out at different ac frequencies and response from the system contains the information about interface, and its structure and reactions taking places in the system. The current response to a sinusoidal potential will be a sinusoid at the same frequency but shifted in phase (φ) and an expression analogous to Ohm’s law allowed defining the impedance of the component. The impedance (Z) is dependent on the frequency (ω) of the ac signal and consists of real and imaginary components. Therefore, impedance can be expressed in terms of magnitude (Z_0) and the phase shift (φ) as given in the following equation.

$$Z(\omega) = Z_0\,(\cos\varphi + j\sin\varphi) \dots\dots\dots\dots\dots\dots\dots\dots\dots\dots\dots\dots\dots\dots\dots\dots\dots\dots\dots\dots \quad (37)$$

The collective effects of inductance and capacitance form the imaginary part of the complex impedance, whereas resistance forms the real part. In an electrical circuit with a capacitor and a resistor, the ac voltage lags the ac current across the capacitor by 90° and

therefore the imaginary part of the complex impedance is negative. If the real part is plotted on the X-axis and the imaginary part is plotted on the Y-axis of a chart in a range of frequency is called *Nyquist plot*. In this plot the Y-axis is negative and each point on the plot is the impedance at one frequency. On the Nyquist Plot the impedance can be represented as a vector of length $|Z|$. The angle between this vector and the X-axis is commonly called the *phase angle*. Figure 31 shows the Nyquist plot of a simple electrical circuit.

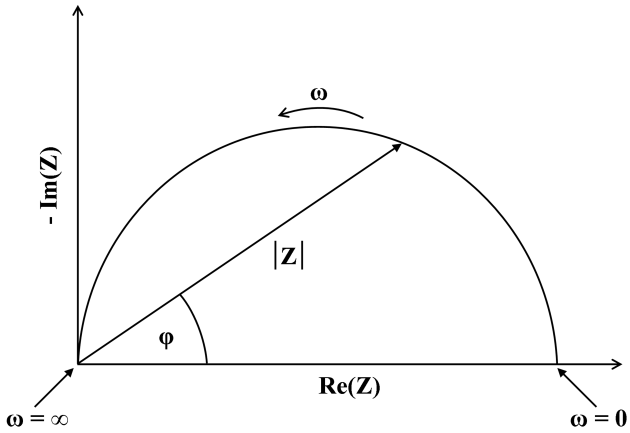

Figure 31. Schematic diagram of a Nyquist plot of simple electrical circuit. (Reproduced with the permission of the copyright owner **[138]**)

The semicircle is characteristic of a single *time constant* and several semicircles can be seen based on the electrical properties (or components) of the system. Another popular presentation method is the *Bode* plot. In this representation, impedance is plotted with log frequency on the X-axis and both the absolute values of the impedance ($|Z|$) and the phase-shift on the Y-axis. The absolute value of the impedance ($|Z|$) can be defined as follows,

$$|Z| = \sqrt{(Im(Z)^2 + Re(Z)^2)} \dots\dots\dots\dots\dots\dots\dots\dots\dots\dots\dots\dots\dots\dots\dots\dots\dots\dots\dots\dots\dots\dots \quad (38)$$

The AC electrical conductivity (σ) of the CNT-polymer composite can be determined using following equation,

$$\sigma(\omega) = \frac{\ln 2}{\pi d}\frac{1}{|Z|} \dots\dots\dots\dots\dots\dots\dots\dots\dots\dots\dots\dots\dots\dots\dots\dots\dots\dots\dots\dots\dots\dots\dots\dots\dots. \quad (39)$$

Where, d is the thickness of the film and $|Z|$ is the absolute value of the impedance.

3.10.3 Experimental setup

The custom built experiment setup was used to measure the AC conductivity of CNT-polymer composite thin films. Here, the square array of an equally spaced 4-point probe head is attached to a positioner system and the whole system mounted on a sample stage was used. The gold plated probes mounted on springs were used as leads and ohmic contact was made from the copper wires, which enter the probe through a plastic block. During the measurements, probes were pressed on the silver electrodes deposited on the sample using a spring-loaded system to obtain better ohmic contacts. The two adjacent probes supplied voltage into the material, and the other two probes were used for measuring the resultant current across the surface of the sample. This technique eliminates measurement errors due to probe resistance and the contact resistance between metal probe and material. Since high impedance gain-phase analyzer involves its current source and voltmeter, the voltage drop across probe resistance and contact resistance is very small due to the draw of little current.

The other end of the probe was connected to a Solartron SI 1260 impedance analyzer to obtain the impedance spectra (Nyquist and Bode plot) by applying ac voltage of 1 V.

Impedance measurements were carried out in a frequency range of 200 Hz to 1 MHz. The conductivity measurements of each sample were carried out in room temperature. The impedance spectra were collected by ZPlot software and the data was analyzed using the ZView program. The absolute value of the impedance at each frequency was obtained and ac conductivity was calculated based on equation (39).

3.11 Atomic Force Microcopy (AFM)

Scanning Probe Microscopy (SPM) is one section of microscopy technique that was developed to provide useful information about properties of a sample at nanometer-resolution, such as topography, hardness, and conductivity. The images of the sample surface arising from this technique are due to the interaction of a proximal probe with a sample surface. The image is formed while the probe is scanned across the surface in a raster pattern as keeping the track of the probe sample interaction as a function of the probe (tip) position. Different types of scanning probe technique can be derived depending on the probe utilized. One of the most common surfaces and thin films analysis techniques is Atomic Force Microscopy (AFM) [139]-[143]. AFM is used to probe the sample in three dimensions and enables 3D images of a sample surface with high lateral spatial resolution (0.1 to 1.0 nm) to form, as well as atomic scale vertical resolution (0.01 nm). It does not require any special sample preparation and it can be used in either an ambient, vacuum, or aqueous conditions.

AFM consists of a micro fabricated sharp tip made up of either silicon or silicon nitride (Si_3N_4) attached to a low spring constant cantilever with different spring constant and resonant frequencies placed above the sample surface, a mechanical system to move and

raster the tip across the sample, a force sensor that deflects as a result of the sample-induced force and a computer with a feedback control and display system for controlling the deflection. The principal behind the operation of an AFM can be described as follows. A very low force about 10^{-9} N is maintained on the cantilever, therefore, when the cantilever moves across the sample it deflects upward or downward owing to the repulsive or attractive force between the tip and surface. According to Hooke's law this force (F) is proportional to the deflection (x) of the cantilever. Therefore,

$$F = kx \dots\dots\dots\dots\dots\dots\dots\dots\dots\dots\dots\dots\dots\dots \qquad (40)$$

Where, k is the spring constant of the cantilever. This deflection can be measured by an optical system which consists of a diode laser, a mirror, and a position sensitive photodiode. The cantilever reflects the laser light to the position sensitive photodiode with the help of reflective coating on the back side of the cantilever and the mirror. Deflections of the cantilever change the position of the laser beam on the photodiode. These deflections are associated with the topography of the sample surface, which is used to generate the image of the sample surface by the control system. A piezoelectric actuator controls the movement of the cantilever. A general schematic of an AFM system is shown in Figure 32.

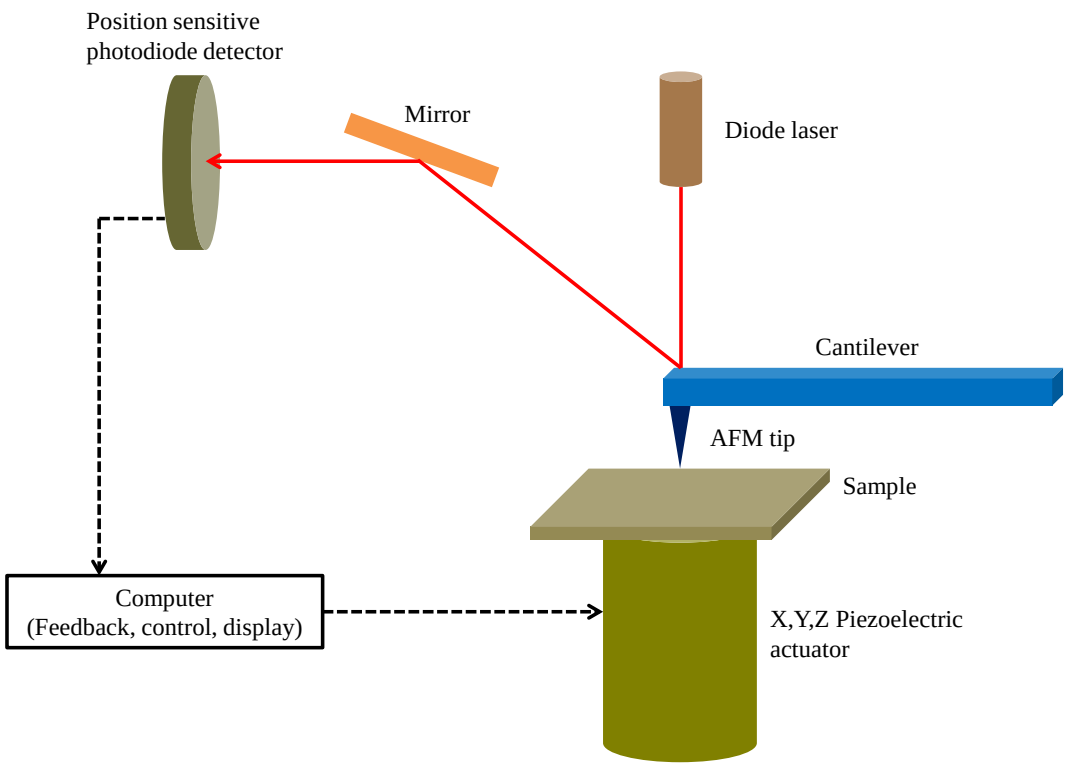

Figure 32. A simple schematic diagram of a typical AFM instrument. (Adopted from Baer et al. **[103]**)

The atomic force microscope can be operated in different imaging modes such as contact mode, non-contact mode, and tapping mode. The contact mode can be operated in constant height mode, i.e., while keeping a constant distant between the tip and the sample surface, and the deflection of the cantilever is used to determine the topography of the sample surface. Contact mode is the easiest way to get atomic scale images, since it observes the hard-core repulsive force between the tip and the sample. On the other hand, contact mode has the potential to generate scan-induced artifacts in the image.

In non-contacting mode, the tip is vibrated at its resonant frequency just above the sample surface. Changes in the attractive van der Waals' forces exerted on the tip due to topography cause the change in the vibration frequency of the cantilever to shift. This

change in the vibration frequency is used to generate the topography image of the sample surface [144].

In tapping mode, at the beginning the cantilever is vibrated at its resonant frequency at much higher amplitude compared to non-contact mode. Then, the tip is brought close to the sample surface so that it comes in contact with the sample surface. This leads to the reduction of the vibration amplitude of the cantilever. This reduced amplitude can be used to maintain the fixed separation between the tip and the sample surface and hence to generate the topography image of the surface [145]. In this study, the Veeco Dimension Icon atomic force microscope is used to image the composite surface using the contact mode.

CHAPTER 4

SAMPLE PREPARATION

4.1 Deposition of Ni catalyst thin films on Si (100) substrates

The growth of Ni catalyst thin films on p-type boron doped Si (100) substrates by physical vapor deposition (PVD) is discussed in chapter 3. Si (100) is the preferred substrate because nanotubes synthesis on the Si substrate might be integrated with conventional microfabrication techniques to obtain a new type of nano-scale device. The Si (100) ($10\times10\times0.575$ mm^3) substrates were cleaned using liquid soap and DI water, and later ultrasonically cleaned with isopropyl alcohol (IPA) for about 15 minutes, and dried using dry air prior to loading in the PVD chamber. There was no further cleaning process inside the chamber. Before the deposition of Ni thin films, the chamber was evacuated to a base pressure of 1×10^{-8}Torr.

For the deposition, high-purity Ni metal (99.9%) target was evaporated by DC magnetron sputtering using argon (Ar) gas, and the DC power supply was set to *constant power* mode at 30W. The Ar gas flow rate was optimized at 200 Standard Cubic Centimeters per Minute (SCCM) for stabilizing the Ni flux prior to opening the target shutter. Thin films of Ni were grown by directing Ni metal flux onto the Si (100) substrate at room temperature in argon plasma of ~ 10^{-3} Torr. The growth rate was determined *ex-situ* by analyzing the as-deposited films using X-ray reflectivity (XRR), Rutherford backscattering spectrometry (RBS), and X-ray photoelectron spectroscopy (XPS). Thin

films with different thickness from 3nm to 50 nm were deposited by keeping the DC power and argon gas partial pressure fixed for all the deposition.

4.2 Carbon nanotube synthesis

A microwave plasma enhanced CVD (MW-PECVD) system with 2.45 GHz and 600W of frequency and power respectively (Tekvac PECVD-60-M) was used to synthesize carbon nanotubes as mentioned in chapter 3. The microwave enhanced plasma is shaped by a conical waveguide to get possible uniform plasma. An O-ring sealed quartz interface passes microwave radiation into the reactor. The platen is made up of stainless steel and can be heated with a resistance type heater for temperatures up to 800 °C. The temperature is monitored and controlled by a microprocessor temperature controller. The temperature is measured by a thermocouple located under the platen (sample holder).

Annealing and plasma treatment are crucial steps for the synthesis of carbon nanotube on the Si substrate with thin layer of Ni that acts as a catalyst. Ni layer during the process is fractured into nanometric Ni-islands. These nano-islands will be the origin of CNT growth and it is essential to obtain homogeneous island dispersion on the wafer. In this study, Ni thin films deposited on the Si substrate were placed on the platen inside the reactor chamber, and the chamber was pumped down to 0.1Torr and a two-step pre-growth treatment of the surface was performed. The samples were heated to 600 °C for 60 minutes in hydrogen (H_2) gas at about 0.4 Torr and 40 sccm to keep a reducing atmosphere and preventing Ni oxidation. This step was followed by a hydrogen plasma treatment for 30 minutes in order to create nano-islands of Ni. The growth of CNTs was performed immediately after the hydrogen plasma treatment step using the same reactor

with mixture of hydrogen (H_2), methane (CH_4), and argon (Ar) gasses at the same temperature. The growth time was 30 minutes for all the samples and the experimental parameters are summarized in Table 2.

Table 2: Summary of the experimental parameters for the growth of CNTs on Si substrate

Sample Name	Annealing time in H_2 plasma (min.)	Dep. Temp. (°C)	Gas flow rate (sccm)			Reactor pressure (Torr)
			Ar	CH_4	H_2	
A1	30	600	0	2.5	40	0.53
A2	30	600	0	5.0	40	0.54
A3	30	600	0	10.0	40	0.60
A4	30	600	0	15.0	40	0.65
B1	30	600	10.0	2.5	40	0.57
B2	30	600	25.0	2.5	40	0.62
B3	30	600	40.0	2.5	40	0.69
C1	30	600	10.0	10.0	40.0	0.65
C2	30	600	25.0	10.0	40.0	0.72
C3	30	600	40.0	10.0	40.0	0.75
D1	30	600	50.0	2.5	0	0.46
D2	30	600	50.0	5.0	0	0.51
D3	30	600	50.0	10.0	0	0.58
E1	30	600	50.0	2.5	5.0	0.55
E2	30	600	50.0	2.5	10.0	0.57
E3	30	600	50.0	2.5	25.0	0.72

4.3 Synthesis of carbon nanotube-polymer composite

This section is divided into two sections for discussing the materials used for synthesis of the composite, and the fabrication technique of the CNT-polymer composite.

4.3.1 Materials

Carbon nanotubes: Catalytic vapor deposition synthesized multi-wall carbon nanotubes were purchased from Sigma-Aldrich (USA). The characteristic of the carbon nanotubes as per the manufacture's specification are as follows. The outer diameter of the nanotubes varies between 6-9 nm and the length is about 5µm. Bulk density is about 0.22 g/cm^3.

Polymer: Selectophore polyurethane from Sigma-Aldrich was used as polymer matrix.

Cross-linkers: Two systems of resins were used as cross-linkers. The idea was to link the polymer chains to each other via cross-linkers and enhance the mechanical properties of the composite. 1,2,6-Trihydroxyhexane and 2,4,6-trihydroxybenzaldehyde from Sigma-Aldrich were used as cross-linkers and both consisted of three –OH groups making them viable systems as cross-linkers.

4.3.2 Synthesizing CNT-polymer composite

Preliminary experiments were conducted to assess the dispersibility of carbon nanotubes and solubility of the polymer matrix and cross-linkers in different types of surfactant. It was observed that dispersibility of CNTs, solubility of polymer matrix, and cross-linkers can be achieved in 1-Methyl-2-pyrrolidinone (NMP).

First, a known amount of PU (800 mg) is added to a known volume of NMP (20 ml). The whole solution was stirred for 48 hours at 50 °C in a water bath. Then, 4 ml of this solution is loaded with different carbon nanotube weight percentages of 1 wt.%, 5 wt.%, 8 wt.% ,10 wt.% and 15 wt.% to the total weight of polymer and carbon nanotubes. A CNT-loaded solution was stirred for few hours depending on CNT loading to achieve

homogenous CNT-polymer solutions. This was followed by ultra-sonication for 30 minutes until the nanotubes were finely dispersed. This procedure was repeated for the synthesis of two more sets of CNT-polymer solutions with exactly the same amount of CNT loading. Then, about 18 mg of 1,2,6-Trihydroxyhexane was added to each of 1 wt.%, 5 wt.%, 8 wt.%, 10 wt.% and 15 wt.% CNT-polymer solutions. Next, 18 mg of 2,4,6-trihydroxybenzaldehyde was added to the reaming CNT-polymer solutions. The cross-linkers added solutions were further stirred for another 3 hours followed by 10 minutes of ultra-sonication. Figure 33 shows a schematic diagram of the CNT-polymer solution processing.

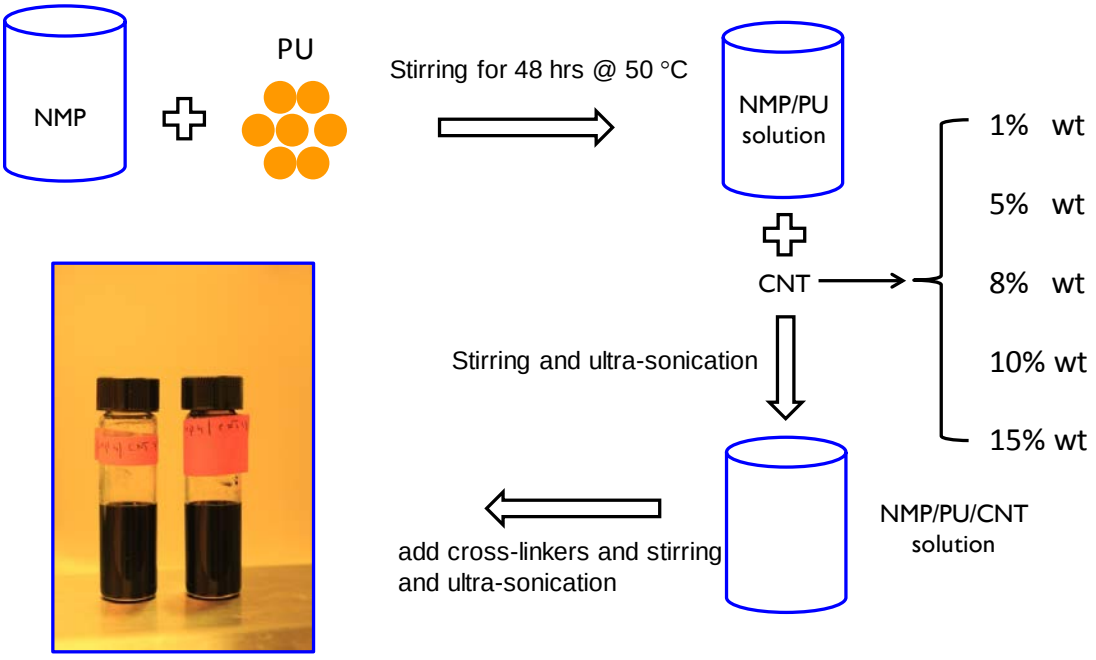

Figure 33. Schematic diagram of the CNT/polymer solution processing.

Thin films samples were prepared to assess the electrical and strain sensing properties of CNT-polymer composite samples. Samples were synthesized on polyimide using a spin

coating technique following experimental parameters such as revolutions per minutes (rpm) and coating time, which were optimized after the preliminary experiments. The polyimide substrates (1.5×1.5 cm^2) were treated with plasma using UVO cleaner (model: Jelight 342) for achieving better adhesion between the substrate and composite. In this process, the substrate was treated with an ultra-violet light and ozone beam for 20 minutes. Oxidation of the surface is responsible for the increase in the polar groups, which is directly related to the adhesion properties of the substrate surface. Once the plasma treatment was done, the substrates were transferred to a clean room facility for thin film deposition of composites. In the clean room, the polymer-carbon nanotube solution was carefully drop-casted onto the plasma-treated substrate and spin coated at 500 rpm for 30 seconds to spread the solution uniformly on the surface. Thin films between 1.5-2.0μm were obtained after 24 hours of curing at room temperature in a vacuum oven.

CHAPTER 5

RESULTS AND DISCUSSION

5.1 Growth rate of Ni catalyst layers on Si (100) substrate

Metals used to catalyze carbon nanotube formation are generally transition metals such as nickel, cobalt, and iron [23] [146] [147]. The ability of transition metals is interrelated to their catalytic activity for the decomposition of carbon compounds and the possibility for carbon to diffuse through and over the metals very quickly [148] [149]. Integration of carbon nanotubes into nano-devices needs fine control of its morphology such as the number of walls, chirality, or growth rate. For achieving a nanotube with predefined parameters using a CVD system, the size of the catalyst particles is important, which is directly related to the thickness of the catalyst layer. Controlling the particle size and chemical environment, the CVD technique can grow single-wall, double-wall, or multi-wall carbon nanotubes [150]-[152]. Recent studies also have shown that the CVD technique can be used to synthesize the SWCNTs with preferential chirality [153]. Even though these new advances have been developed by researchers, the role of the catalyst particles is not fully understood and overall control of CNT growth is still a great challenge. For this investigation, to determine the Ni deposition rate on Si (100) with the experimental parameters mentioned in section 4.1, Ni layers were deposited with different deposition times such as 3.5, 5.0, 8.0, 10.0 and 12.0 minute. Rutherford Backscattering Spectrometry (RBS) was carried out on Ni films to investigate the

film/substrate interface characteristics and to determine the film thickness. The fitted experimental and simulated RBS spectra of the 3.5 minute deposition time Ni film along the random direction are shown in Figure 34. The clearly defined film/substrate interface with the sharp Si edge and Ni peak indicate that there is no inter-diffusion of metal atoms across the film/substrate interface. The film thickness was also determined from the fitted experimental and SIMNRA [106] simulated spectra using the width of the Ni peak, which was found to be around 13.7 nm for the sample under characterization. The areal density of the Ni peak (120.845×10^{15} atoms/cm^2) given in SIMNRA was divided by the atomic density of bulk Ni (9.13×10^{22} atoms/cm^3) to determine the film thickness. The atomic density of bulk Ni was calculated using the mass density value of 8.908 g/cm^3 with help

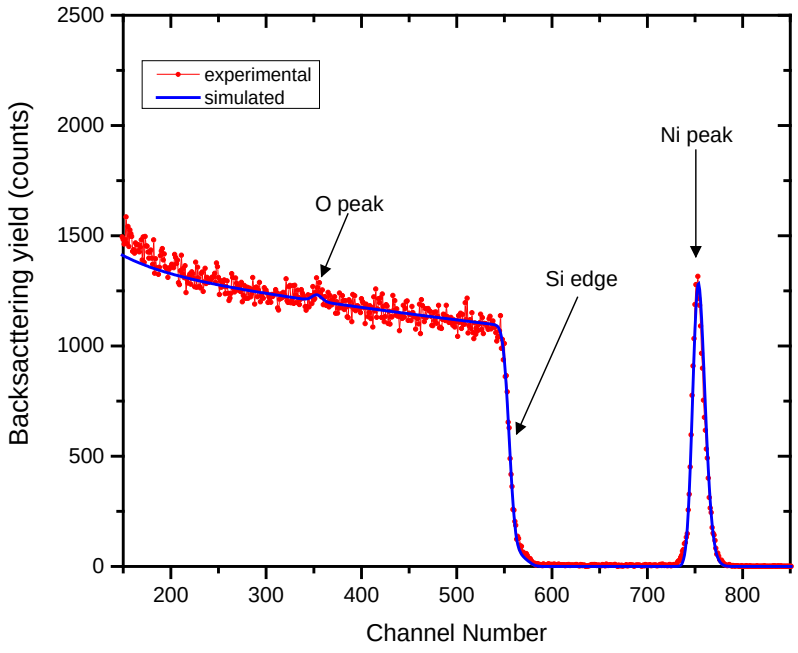

Figure 34. The experimental and simulated RBS spectra of the 3.5 minutes deposition time Ni film deposited on Si (100) substrate.

of TRIM [154] [155] software. Further, around channel number 354 there is a small peak on the Si background, which corresponds to oxygen. This indicated that the first few layers of Ni film were oxidized due to exposure to air. Similar RBS and SIMNRA characterization and simulations were conducted on other samples as well.

X-ray reflectivity (XRR) is a quantitative technique to evaluate electron density, thickness and roughness of thin layers. XRR probes the electron density perpendicular to a surface and hence reveals vital information such as thickness, electron densities and roughness parameters of a layered system. Accuracy and non-destructive nature of XRR can be used to investigate surfaces and interfaces of thin film system at atomic resolution [156] [157]. The coplanar scattering of X-ray around the reciprocal-lattice point is the origin of this technique. The plot of the reflected X-ray intensity against the incidence angle or the reciprocal lattice vector $\boldsymbol{q}$ becomes the XRR profile. The X-ray has a bit higher refractive index for air than condensed matter. Therefore, the incidence angle is lower than the critical angle ($\theta_c = \cos^{-1}(n_{medium}/n_{air})$), and the X-ray beam is totally reflected by the medium. For the small incidence angle, θ_c can be expressed in radians as follows [158],

$$\frac{\theta_c^2}{\rho} = \frac{r_e\lambda^2}{\pi} \dots\dots\dots\dots\dots\dots\dots\dots\dots\dots\dots\dots\dots\dots\dots\dots\dots\dots\dots\dots\dots\dots\dots\dots\dots\dots\dots\dots\dots\dots\dots\dots\dots\dots\dots \quad (41)$$

Where, r_e is the classical electron radius (2.82×10^{-15}m), λ is the X-ray wavelength and ρ is the electron density. X-rays incidence at higher angles penetrates into the medium and the reflected intensity falls based on Fresnel law. Due to the interference of X-rays reflected at different interfaces on the substrate, the intensity of reflected X-rays oscillates with the angle of incidence (Kiessig fringes). The amplitude of fringes depends

on surface, interface roughness, and electron densities of materials. For simple systems like single-layer, bilayer, or periodic multilayer, thickness of layers can be determined through modified Bragg equation,

$$m\lambda = 2t(n^2 - cos^2\theta_m)^{1/2} \ldots\ldots\ldots\ldots\ldots\ldots\ldots\ldots\ldots\ldots\ldots\ldots\ldots\ldots\ldots\ldots\ldots\ldots\ldots\ldots\ldots\ldots\ldots\ldots. \qquad (42)$$

Where m is the diffraction order, t is the layer thickness (multilayer period), n is the mean refractive index of the layers, and θ_m is the incidence angle at which interference maximum of the order m occurs. Further, when the layer system becomes more complicated, the data is processed through modeling and fitting. In these XRR measurements, which were performed using a Philips X'pert diffractometer, a Cu K_α filtered parallel X-ray beam of approximately width of 10 mm and 0.1 mm of height with wave length λ= 1.54056 Å was incident upon a sample at a grazing angle. XRR scans were recorded within the angular range of 0.1° to 5.0° in 0.005° steps. Figure 35 shows XRR curves for the Ni film on Si (100) substrate deposited with 3.5 minutes deposition time. Quite accurate fits to the experimental data were obtained for all five layered structures. Usually a model for a single layer requires five fitting parameters, of which film thickness, density, and interface roughness are the most important ones. The proposed structure used for experimental data fitting is shown in the inset of Figure 35. Based on this fitting, the model layer structure consists of an SiO_2 layer on the Si substrate. This could be due to the exposure of the Si substrate to air. Further, the Ni layer is also oxidized as suggested by RBS technique. For these films the surface roughness varies between 14.39Å and 19.80Å and the density of the films varies between 7.347 g/cm^3 and

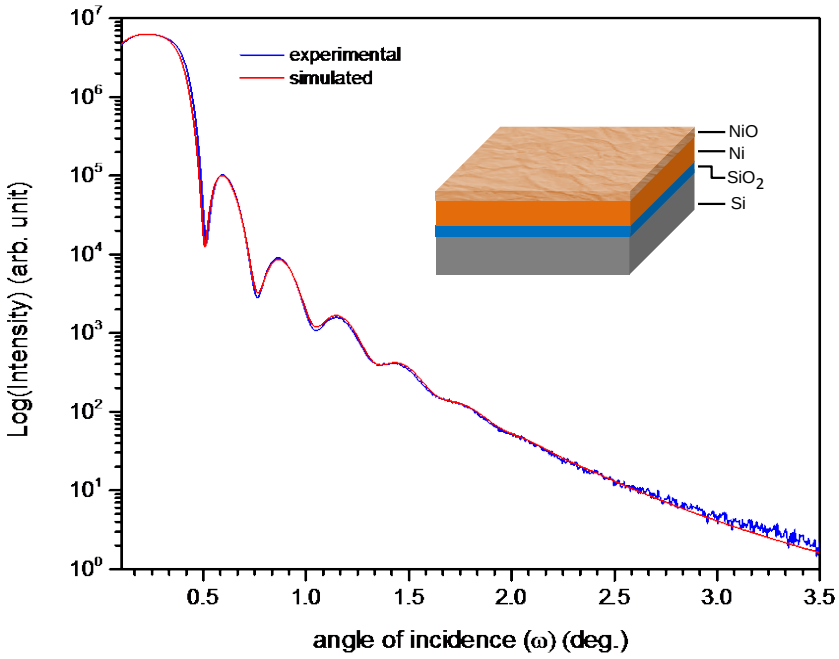

Figure 35. XRR fringe pattern for Ni/ Si (100) for 3.5 min deposition time film with layer thickness about 11.8 nm. The layer structure used for XRR fitting is shown in the inset.

8.272 g/cm^3. The surface roughness and density values are typical for samples grown by magnetron sputtering. Table 3 summarizes the parameters obtained from both RBS and XRR techniques.

Table 3: Summary of structure parameters obtained from RBS and XRR.

Sample based on dep. time	RBS	XRR	
	Thickness (±1nm)	Thickness (±2.9nm)	Roughness (±2.06Å)
3.5 min.	13.7	11.8	15.64
5.0 min.	16.4	18.5	16.63
8.0 min.	27.4	28.1	14.39
10.0 min.	30.5	36.9	15.51
12.0 min.	31.3	48.0	19.80

Based on XRR thickness calculations, it was found out that the deposition rate of Ni thin films is about 4.10 ± 0.2 nm per minute. The catalyst film thickness of about 4 nm is suited for carbon nanotube nucleation and growth; it was decided to deposit Ni thin films with 1 minute deposition time on the Si (100) substrate and then RBS, XRR, and SEM characterization were carried out. Figure 36 shows RBS, XRR data of the Ni thin film for 1 minute deposition time. The thickness of the film is about 3.7 nm and 2.6 nm according to XRR and RBS respectively. RBS uses bulk density of Ni to determine the Ni film thickness. Generally it is well known that bulk density of the material is different from its thin film density. Therefore, XRR film thickness values are much reliable than RBS values.

Figure 37 (a) shows the SEM image of the above mentioned thin film and it shows that the Ni film is almost continuous. This feature can be explained via the nucleation and growth process of a thin film. The growth process emerging from a statistical process of nucleation, surface-diffusion growth of 3D nuclei, and formation of a network structure followed by subsequent filling to give a continuous film based on various experimental and theoretical studies. Based on the thermodynamic parameters of the target material and the substrate surface, initial nucleation and growth steps can be describe as (1) Volmer-Weber (island) type (2) Frank-van der Merwe (layer) type, and (3) Stranski-Krastanov (mixed) type [83]. Therefore, the growth of the Ni film on the silicon substrate can be explained by thermodynamic parameters and *wetting* properties of the target and the substrate. Thus the problem is whether the metal would at equilibrium form a continuous film or would form particles or a discontinuous film on the surface. By assessing the spreading coefficient S from the surface energy of the metal/substrate

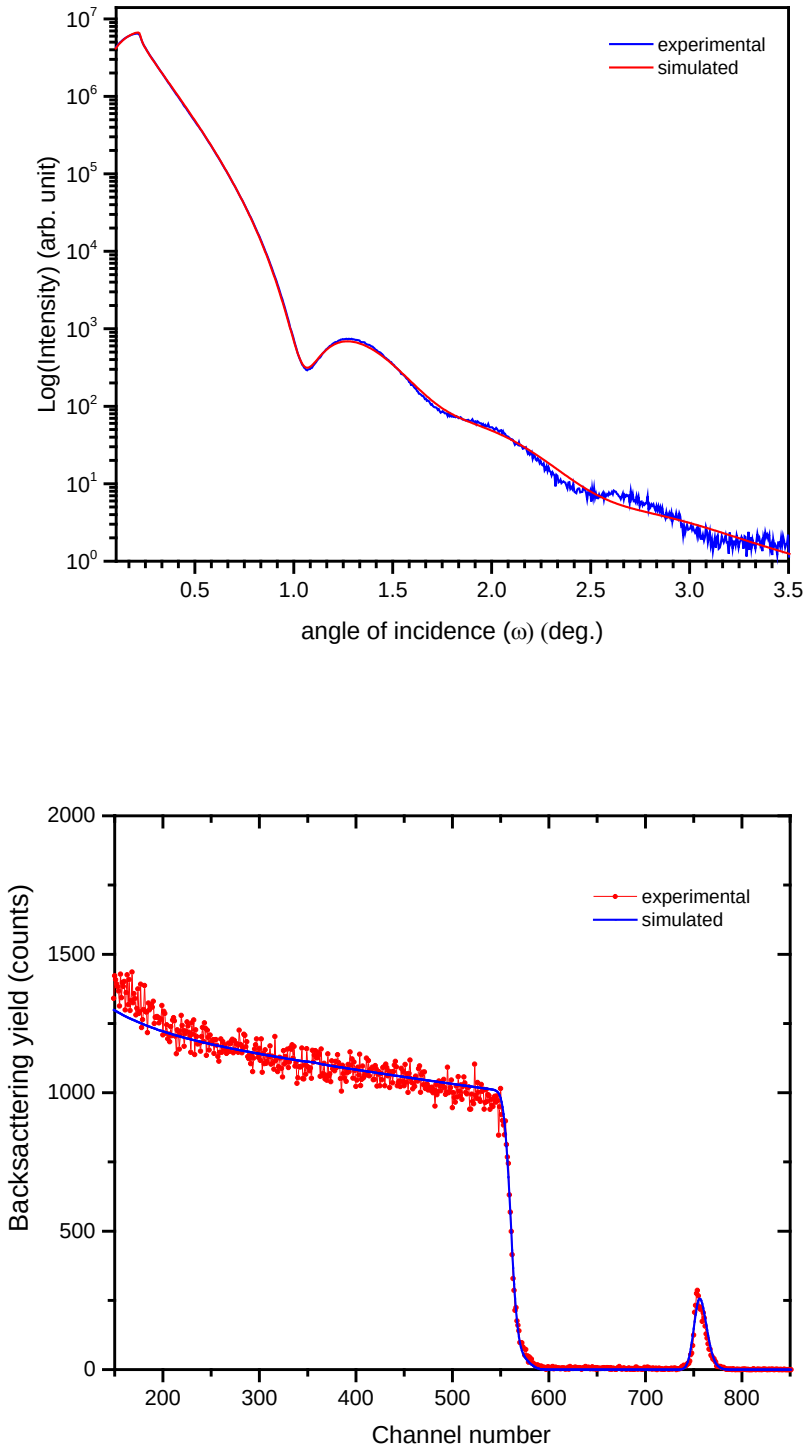

Figure 36. XRR fringe pattern (top) and RBS spectra (bottom) for Ni/Si (100) 1 min. deposition time.

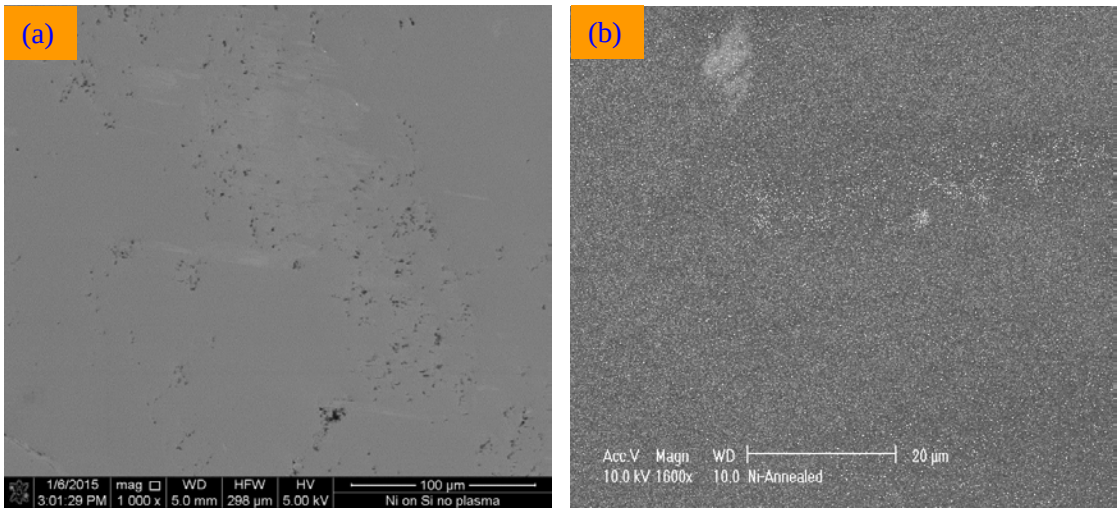

Figure 37. SEM image of the (a) as-deposited Ni thin film for 1 min. deposition time and (b) as-deposited sample after annealing in H_2 environment at 600 °C for 60 minute.

interface γ_i, substrate surface energy γ_s and the nickel surface energy γ_{Ni} as following formula [159],

$$S = \gamma_s - (\gamma_i + \gamma_{Ni}) \dots\dots\dots\dots\dots\dots\dots\dots\dots\dots \quad (43)$$

If $S \geq 0$, then it is expected that a spreading of Ni on the substrate (complete wetting) would occur. If not, the surface remains dry, i.e., the metal partially wets the substrate. The surface energies of Si (γ_{Si}~2130 mJ/m^2) [160] and Ni (γ_{Ni}~1883 mJ/m^2) [161] [162] are well known. On the other hand, surface energy of the silicon-nickel interface is not reported in literature. Based on the Katsman et al. [163] report, the silicon-nickel interface energy should be between 100-247 mJ/m^2. According to these interface energies, $S \geq 0$ is more favorable, suggesting a perfect wetting of the Si substrate by Ni. Therefore, formation of the Ni smooth thin film is expected. Prior to CNT growth, a nickel coated silicon substrate were pre-treated in two steps. In the first step, thermal annealing of substrates at 600 °C for 60 minutes in H_2 environment at about 0.4 Torr (or

40 sccm H_2 flow rate) was carried out in the PECVD reactor chamber. Based on the RBS and XRR data, it was revealed that the catalyst layer is oxidized due to exposure to the air or the argon gas used to sputter the Ni target may contain a few parts per million of oxygen impurities. Hence, the thermal process with hydrogen does allow the reduction of the nickel oxide (NiO) to nickel and formation of nickel clusters [164]. Figure 37 (b) shows the SEM image of the as-deposited Ni film after annealing at 600 °C in H_2 for 60 minute and it clearly shows continuous Ni film turned into a granulated layer. The two SEM images shown in Figure 37 (a) and (b) are taken at different magnifications. These are used for qualitative comparison only. To confirm the presence of the Ni on the Si substrate, EDS spectra were collected on bright gray areas of as-deposited and annealed sample. The EDS spectra for as-deposited and annealed samples are shown in Figure 38.

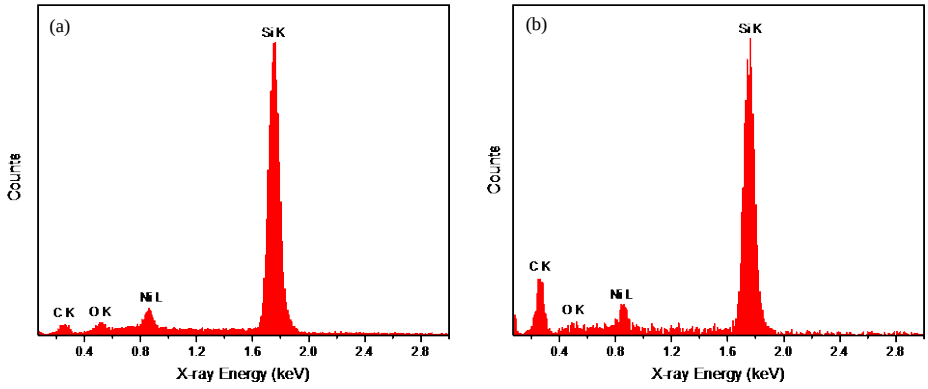

Figure 38. EDS spectra of (a) as-deposited Ni film and (b) as-deposited Ni film after annealed at 600 °C in H_2 environment.

The EDS spectra were collected using 5.0 keV electron beam. The depth resolution of the electron beam is about 5µm and the interaction volume is about 5-10 µm, therefore the characteristic X-ray from Si (Si K ~ 1.74 keV) substrate can be seen in the spectra. Ni L

shell characteristic X-ray appears around 0.85 keV and the intensity of the Ni L radiation is less due to the smaller thickness of the Ni film. The K shells characteristic X-ray of carbon and oxygen are present in the spectra due to contamination.

5.2 Nucleation and growth of carbon nanotubes on Ni catalyst particles

In the second step, the substrates were treated in H_2 plasma for 30 minutes at the same chamber pressure (~0.4 Torr) or same 40 sccm H_2 flow rate. In the H_2 plasma, H_2 molecules are decomposed into radicals as summarized in **Table 4** [165]. The bombardment of the catalyst layer by radicals, atoms, ions and electrons during H_2 plasma treatment results in a granulate catalyst layer into catalytic seeds. To investigate the effect of plasma treatment with time, the substrate with catalyst layers were treated in H_2 plasma for 10, 20, 30, and 40 minutes, SEM characterization was carried out on the samples. Figure 39 shows the effect of H_2 plasma treatment with different times. During the hydrogen plasma treatment, etching of the catalyst layer also occurred. If the pretreatment is too long and the catalyst layer is too thin, the layer can be totally etched. If the plasma pretreatment is too long, a Ni catalyst nano-sized island begins to conglomerate into a larger island that is not suitable for CNT growth as can be seen in Figure 39. This phenomenon arises due to minimization of surface energy enabled by the increase of the surface mobility of the metal atoms and reducing the film stress caused by the difference in thermal expansion during the plasma pretreatment [166]. CNTs were grown on a 30 minute plasma-treated layer as discussed in Chapter 4, due to the absence of SEM images at CNT growth time.

Table 4: Electron-H_2, ion reactions

Electron-H_2 reactions
$\mathbf{H_2 + e \rightarrow H_2^* + e}$
$\mathbf{H_2 + e \rightarrow H^* + H + e}$

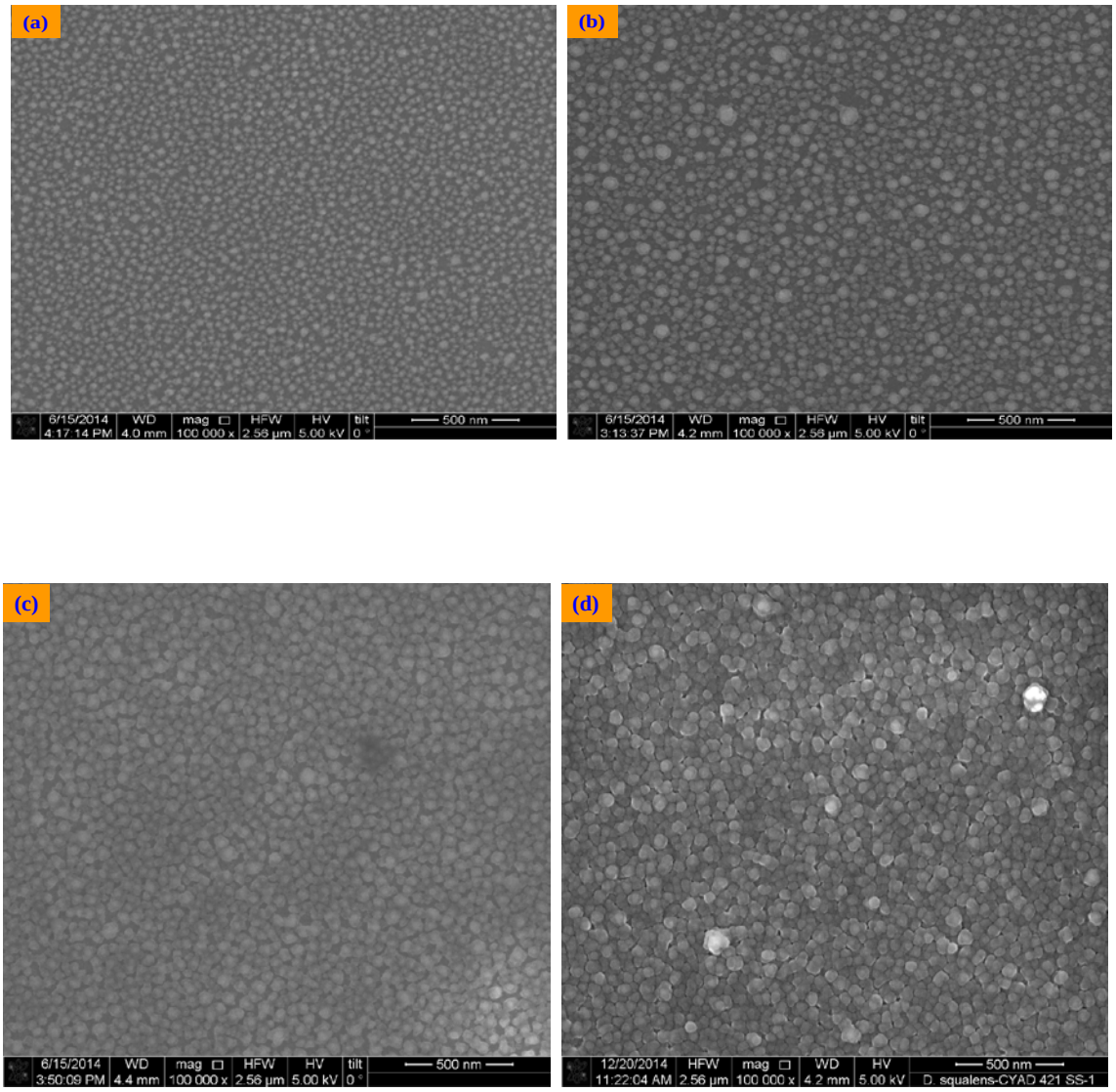

Figure 39. Effect of H_2 plasma treatment with time for (a) 10 (b) 20 (c) 30 and (d) 40 minutes.

CNT growth mechanism: This widely accepted and most general CNT growth mechanism is outlined as follows. There are many types of different non-radicals, radicals, atomic hydrogen and charged species present in the plasma [167]. When they come in contact with the hot metal nano-particles, hydrocarbon and radicals decompose into carbon and hydrogen, with hydrogen then leaving the chamber and carbon dissolving into the metal particle. After reaching the carbon saturation limit in the metal particle, carbon precipitates out and crystallizes in the form of energetically stable cylindrical network without dangling bonds [168]. Decomposition of hydrocarbons releases heat to the exposed zone of metal particle, while carbon crystallization absorbs heat from the particle's precipitation zone. This thermal gradient inside the particle keeps the decomposition, diffusion, and crystallization process on. At this point in time, two different scenarios are possible. If the particle adherence to the surface is weak, then carbon precipitation occurs at the bottom surface of the particle and lifts the whole particle off the substrate. In this case, the resultant scenario is called the "tip growth model". Once the particle is covered with excess carbon its catalytic activity comes to an end and CNT growth is discontinued. If the particle adherence to the surface is strong, initial hydrocarbon dissolution and diffusion take place similar to the tip growth model, but precipitation fails to lift the particle off the substrate and emerge out from the top surface of the particle. Carbon crystallizes as a hemispherical dome and the filament continues to grow with the particle attached to the substrate. This is called the "base growth model". Figure 40 illustrates the CNT growth mechanism.

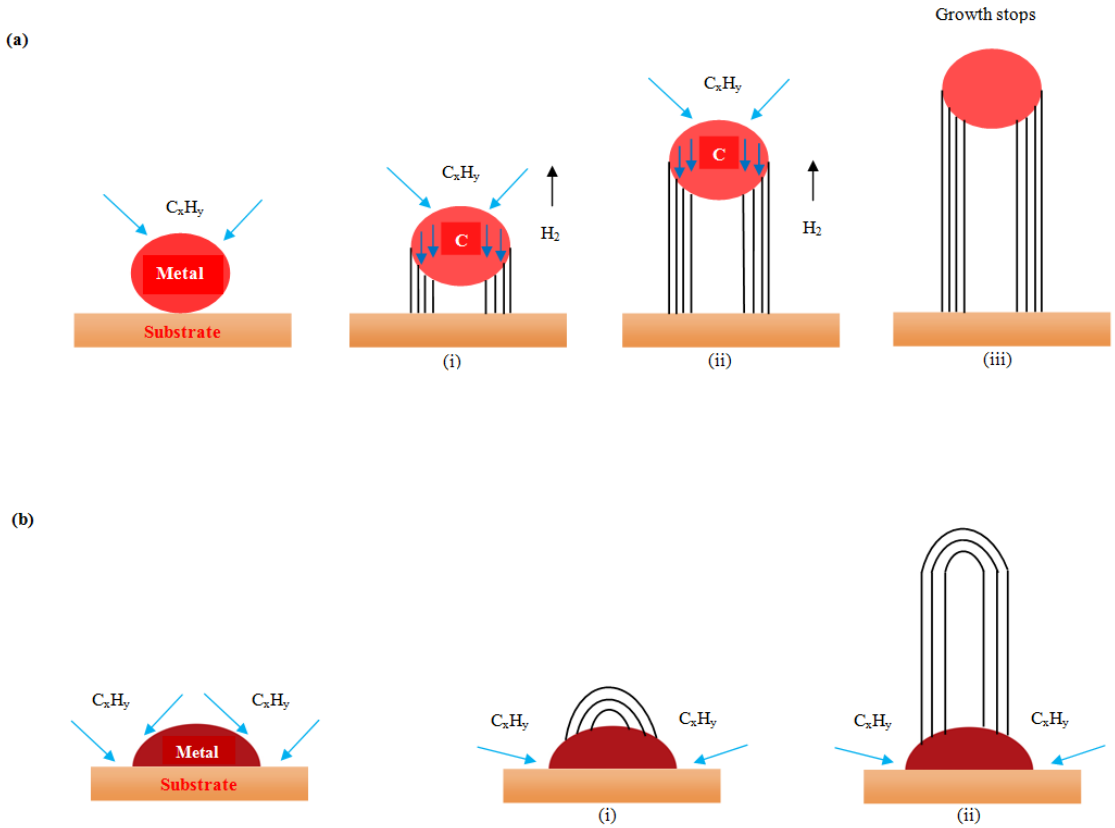

Figure 40. Growth mechanism for CNTs: (a) tip growth (b) base growth mechanisms. (Adopted from Yan et al. **[169]**)

5.3 Raman spectroscopy of PECVD grown carbon nanotube

Raman spectroscopy is for the most part well suited to molecular morphology characterization of carbon materials. Each band in the Raman spectrum corresponds to a specific vibrational frequency of a bond within the molecule. Because vibrational frequency and hence the position of the Raman band is sensitive to the orientation of the bond and weight of the atoms at the end of the bond. The Raman spectrum of single-wall CNT consists of three dominant Raman-allowed bands called G-band, D-band, and radial breathing mode (RBM). The G-band is associated with the longitudinal optical phonon mode, i.e., vibration of sp^2 bonded carbon atoms in tangential to the tube surface and

occurring around~ 1582 cm^{-1}. The presence of disorder in sp^2-hybridized carbon atoms at the edges and atomic defects on the surface of finite-size carbon nanotubes give rise to the D-band feature that appears at~1345 cm^{-1}. The relative intensity of D to G provides a good indicator for determining the crystallinity or the amount of disorder in the carbon nanotubes. The radial breathing mode (RBM) corresponds to the expansion and contraction of the tubes. RBM band appears at the low frequency end of the spectrum around ~186 cm^{-1}. The radial breathing mode is especially important in two ways: (1) for the determination of the diameter of a nanotube (d_t) through the dependence of frequency of RBM (ω_{RBM}), and (2) for relating ω_{RBM} and the resonant optical transition energies E_{ii} for a given tube. Multi-wall CNTs have similar Raman spectra to those of single-wall CNTs. The basic differences are the lack of RBM band and a more prominent D-band. The RBM mode has not appeared because the outer tubes restrict the breathing mode. The more prominent D-band is expected, because the multilayer configuration indicates more disorder in the structure [170] [171].

In this investigation, five different sample sets were deposited on substrates with different experimental parameters, and samples were analyzed using green laser (wavelength: 514 nm). Raman spectra of the first two sets of samples are shown in Figure 41 and Figure 42.

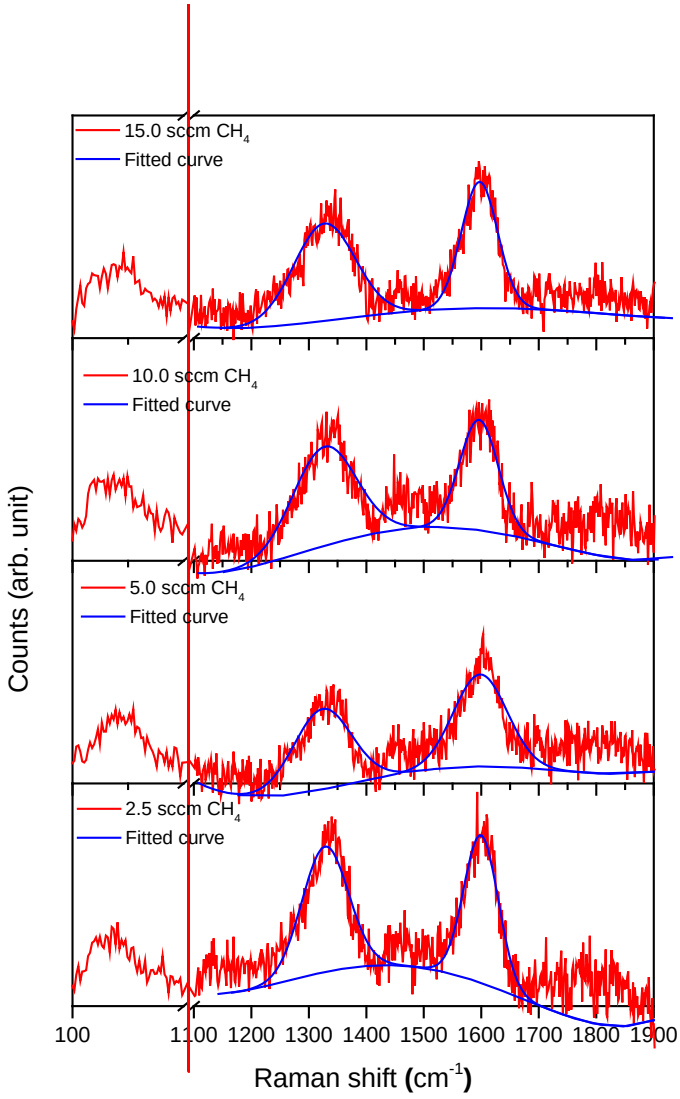

Figure 41. Raman spectra for CNTs growth with 40 sccm H_2, 0 sccm Ar and 2.5, 5.0, 10.0 and 15 sccm of CH_4.

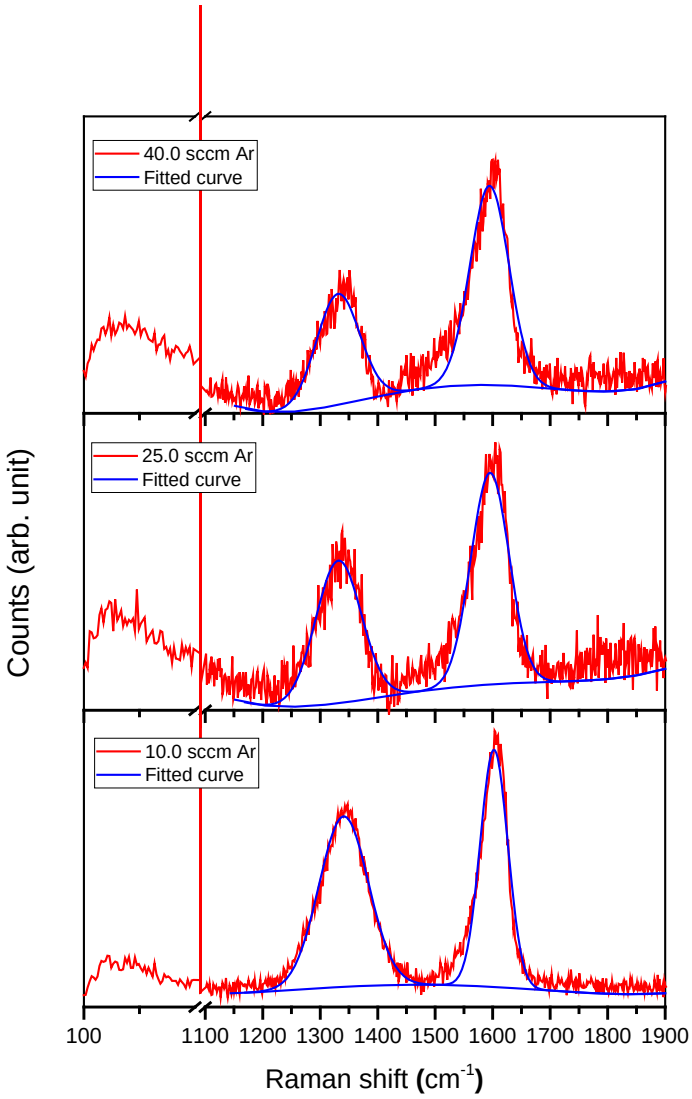

Figure 42. Raman spectra for CNTs growth with 40 sccm H_2, 2.5 sccm CH_4 and 10.0, 25.0 and 40.0 sccm of Ar.

The experimental Raman spectra were simulated and fitted using Origin software to determine the band positions and the intensity of the bands. The D-band position of the growth CNTs is varied between 1338 cm^{-1} and 1352 cm^{-1}. The G-band position also varied between 1585 cm^{-1} and 1610 cm^{-1}. Further, I_D/I_G ratios are very close to 1 or even

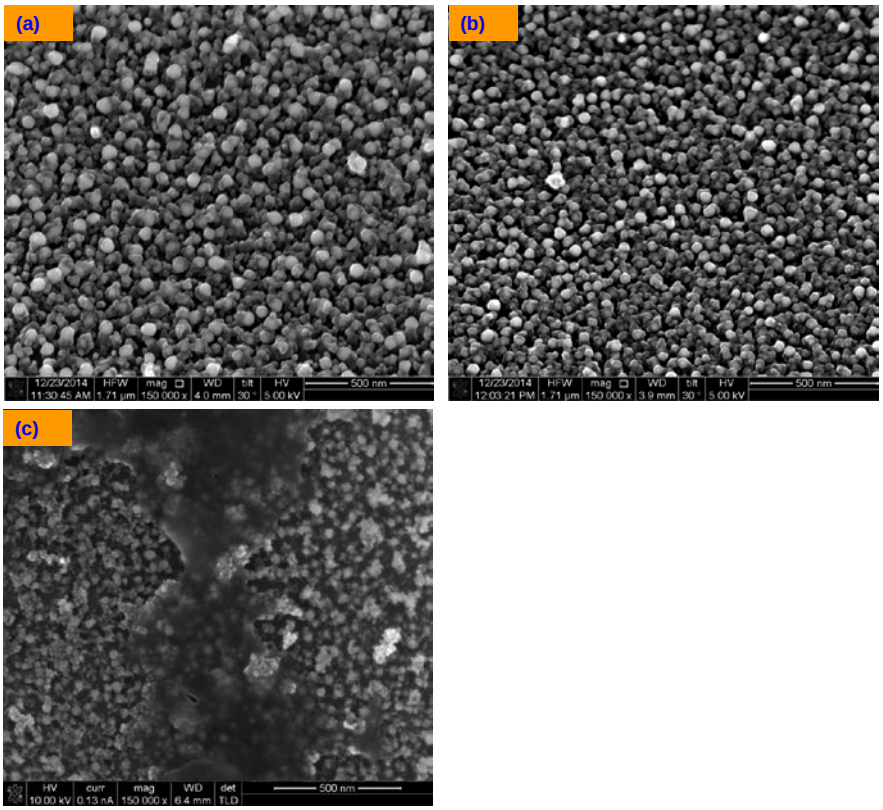

Figure 43. SEM images of CNTs growth at 600 °C with 40 sccm H_2, 0 sccm Ar (a) 2.5 sccm CH_4 (b) 5.0 sccm CH_4 and (c) 40 sccm H_2 and Ar with 2.5 sccm CH_4.

exceed 1. The experimental observations and calculations such as positions of the D-, G-bands and intensity ratio of D- to G-bands were summarized in Table 5. In addition, above observations, the broadening of the D- and G-bands in the spectra is sign of amorphous nature of CNTs growth. Therefore, Raman data indicate that the growth CNTs contain disorder in the structure. At the low frequency, it was not able to observe

the RBM band, indicating growth of multi-wall CNTs.

Figure 43 shows the SEM images of A1, A2 and B3 samples. It is obvious that CNTs growth is not perfect as

Table 5: Summary of experimental outcome of Raman spectra.

Sample name	Gas flow rate (sccm)			Raman band position (cm^{-1})		I_D/I_G ratio
	Ar	CH_4	H_2	D	G	
A1	0	2.5	40.0	1329	1598	0.93
A2	0	5.0	40.0	1324	1598	0.62
A3	0	10.0	40.0	1330	1596	0.78
A4	0	15.0	40.0	1328	1596	0.72
B1	10.0	2.5	40.0	1341	1602	0.73
B2	25.0	2.5	40.0	1332	1596	0.55
B3	40.0	2.5	40.0	1331	1595	0.42
C1	10.0	10.0	40.0	1348	1599	0.89
C2	25.0	10.0	40.0	1327	1595	0.49
C3	40.0	10.0	40.0	1332	1602	0.50
D1	50.0	2.5	0.0	1336	1597	1.05
D2	50.0	5.0	0.0	1341	1600	0.73
D3	50.0	10.0	0.0	1333	1601	0.75
E1	50.0	2.5	5.0	1341	1602	0.79
E2	50.0	2.5	10.0	1333	1599	0.57
E3	50.0	2.5	25.0	1344	1602	0.50

seen on SEM images. It looks like, instead of a cylindrical crystalline growth of CNTs, there is a bulky amorphous carbon formation. The SEM observations agree with the Raman data. To investigate the particles on the CNTs, and EDS spectra were collected on

A1 and B3 samples by focusing the electron beam on the particles of CNTs. The EDS spectra are shown in Figure 44. The EDS spectrum of particles on A1 samples shows intense Ni L radiation peak, indicating the particles on the CNTs to be Ni particles. Since Ni particles can be seen on the CNTs, it is fair to assume the CNTs growth model is a tip growth model. The EDS spectrum of the particles on the B3 samples show less intense Ni L peak. This could be due to amount of Ar ions in the rector chamber. Higher amount of Ar ions in the chamber leads to sputtering off of Ni particles on the CNTs. Raman and EDS data of samples A and B series point out that there are two competing events occurring during the CNTs growth process. The higher amount of methane in the chamber helps to grow better CNTs. On the other hand, when the higher amount of Ar in the chamber, it sputters the carbon atom as well as Ni atoms off the Si substrate. Therefore, the methane and argon gas flow rates should be optimized at a point where crystalline CNTs can be grown.

To investigate the odd formation of CNTs and chemical state of the Ni catalyst layer, XRD and XPS characterizations were carried on substrates that were subjected to different time plasma treatment.

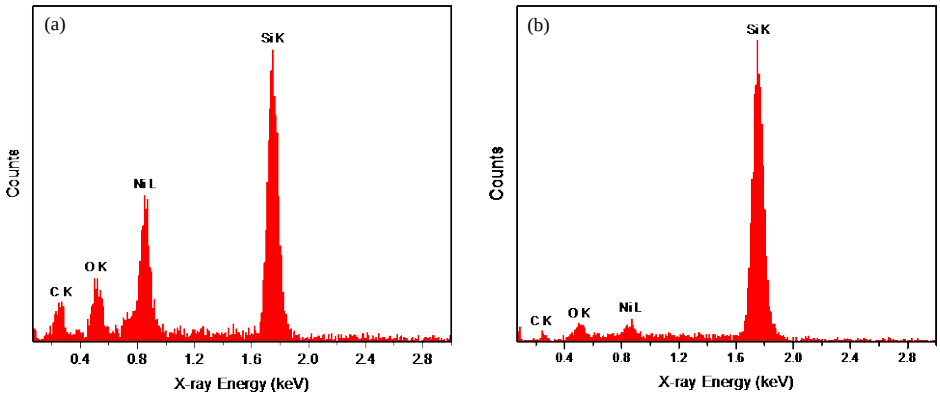

Figure 44. EDS spectra of particles on the CNTs of (a) A1 and (b) B3 samples.

5.4 The glancing X-ray diffraction of Ni catalyst layers

First, GIXRD characterization was carried on as-deposited, 10, 20, 30 and 40 minute plasma-treated samples. GIXRD pattern shows no reflections from the as-deposited thin film suggesting that layer is amorphous. The Figure 45 shows the GIXRD pattern of as-deposited nickel film.

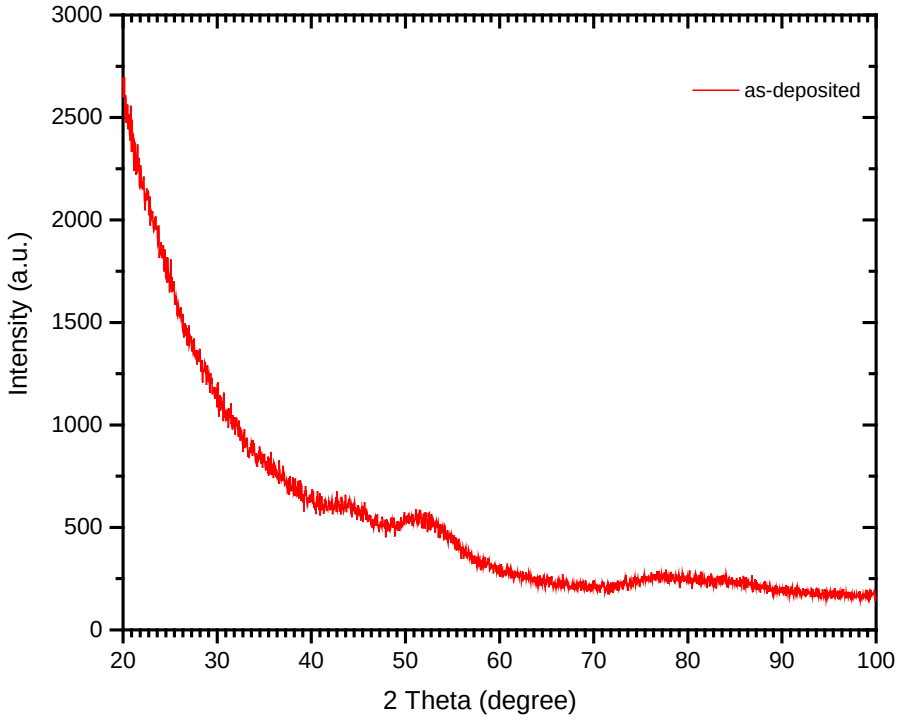

Figure 45. GIXRD pattern of as-deposited nickel thin film on Si substrate.

In 1965, H. Weik and co-workers reported a nickel hexagonal close packed (hcp) lattice system with lattice parameters 2.622 Å, 2.622Å and 4.321 Å for a, b and c respectively. The angles between these axes α, β and γ become 90°, 90° and 120° respectively with space group $p6_3/mmc$ (194) [172]. There are three major reflections from (100), (002)

and (101) planes at 2θ values 39.660°, 41.775° and 45.066° respectively. Figure 46 shows the GIXRD pattern for 10, 20, 30 and 40 minute plasma-treated samples. GIXRD pattern for the 10 minute plasma-treated sample show three major reflections at 2θ values 41.86°, 44.38° and 47.66°. Jade XRD structure calculation was revealed that the XRD pattern for 10 minute plasma-treated sample is originated due to hexagonal close packed lattice system with reduce lattice parameters to 2.491Å and 4.082Å for *a* and *c* axes respectively with $p6_3/mmc$ space group. The reflections at 41.86°, 44.38° and 47.66° are originated from the planes (100), (002) and (101) respectively, the same as reported in literature. The shift in the 2θ to higher values is due to the reduction of the lattice parameters. No other literature was found on the nickel hexagonal close packed structure with reduced lattice parameters. For the 20 and 30 minute plasma-treated samples, the Ni phase is changed from hexagonal p63/mmc to cubic Fm-3m with lattice parameter 3.524Å. The cubic Fm-3m with lattice parameter 3.524Å is the most favorable nickel phase [173]. For the cubic phase, reflections occur at 44.60Å, 51.97°, 76.59° and 93.22° from (111), (200), (220), and (311) planes respectively. But for the 30 minute plasma-treated sample, major reflection peaks are diminished compared to the 20 minute plasma-treated sample. After the 40 minute plasma–treatment, the sample turns out to be amorphous.

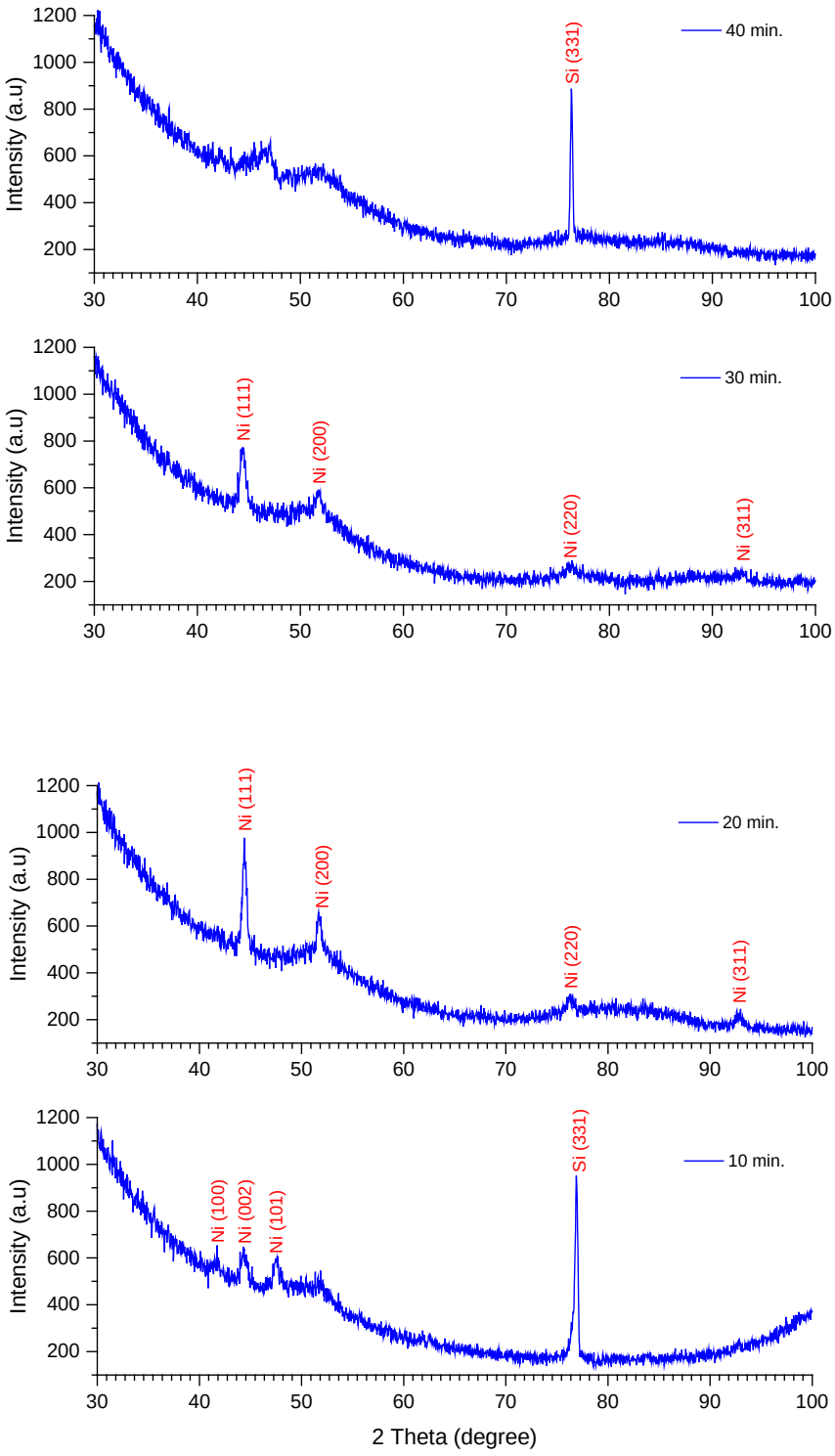

Figure 46. GIXRD pattern of 10, 20, 30 and 40 minute plasma-treated samples.

5.5 X-ray photoelectron spectroscopy of Ni catalyst layers

To determine the chemical states and the composition of as-deposited nickel thin film and plasma-treated samples, XPS experiment was carried out. The near surface XPS survey spectra of as-deposited film is shown in Figure 47, which shows the binding energy peaks corresponding to C1s, N1s, O1s and Ni2p along with Auger lines. The C1s peak appears due to the surface contamination. The Ni2p peak appears in the spectrum in the energy range ~ 840-890 eV. By considering high intensity peaks in the survey scan, high resolution XPS spectrum was obtained for Ni2p region as shown in Figure 48.

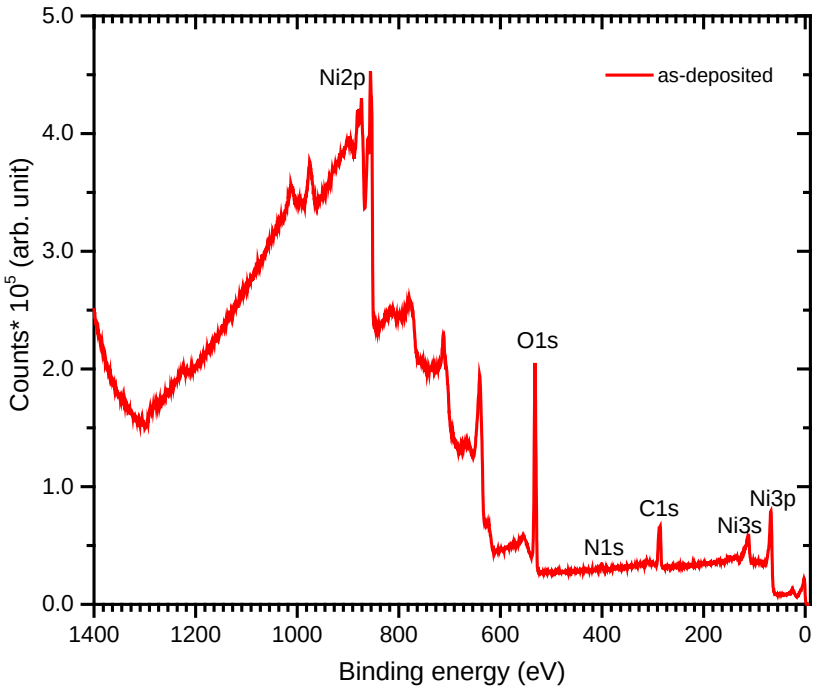

Figure 47. XPS survey spectra of as-deposited Ni thin film on Si (100) substrate indicating the presence of Ni, O and N. The residual C peak is also visible.

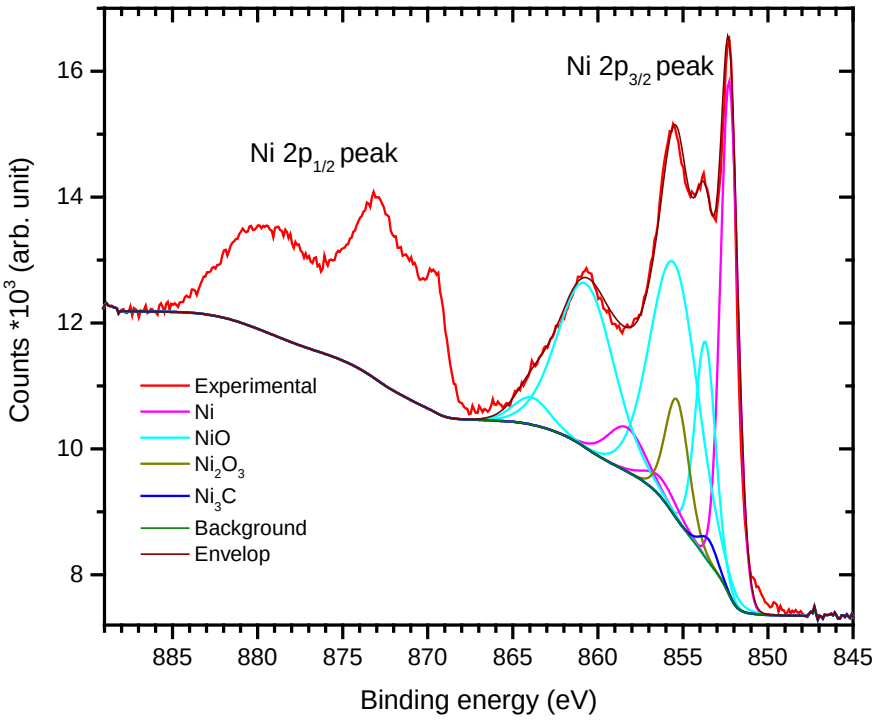

Figure 48. High resolution XPS spectrum of Ni2p which was used to find the chemical state of as-deposited Ni thin films. Ni is in the 0, 2+ and 3+ oxidation states.

The high resolution Ni2p spectrum of as-deposited Ni thin film shows multiple peaks corresponding to multiplet splitting associated with spin-orbit split $2p_{3/2}$ and $2p_{1/2}$ core levels. The spin-orbit splitting between $2p_{3/2}$ and $2p_{1/2}$ core levels is about 17.3 eV. The fitted binding energy peaks located at about 852.28±0.1 eV, 856.30±0.1 eV and 858.30±0.1 eV are the characteristic peaks (pink) for Ni^0 state. The binding energy peaks located at about 853.68±0.1 eV, 855.50± 0.1 eV, 860.70±0.1 eV and 863.90±0.1eV are the characteristic peaks (cyan) for Ni^{2+} (NiO) state. The peaks located at 853.49±0.1eV (blue) and 855.35±0.1eV (dark yellow) corresponding to Ni_3C and Ni_2O_3 respectively

[174]-[176]. XPS data for as-deposited Ni film confirms the existence of the NiO layer. The as-deposited Ni film contains 27.3 at. % of pure Ni and 71.8 at. % as nickel oxides. XPS surface analysis was also used to find out the chemical state of the plasma-treated samples. The survey spectrum of 10 minute plasma-treated samples shows that there is less amount of Ni on the Si surface compared to the as-deposited sample as shown in Figure 49.

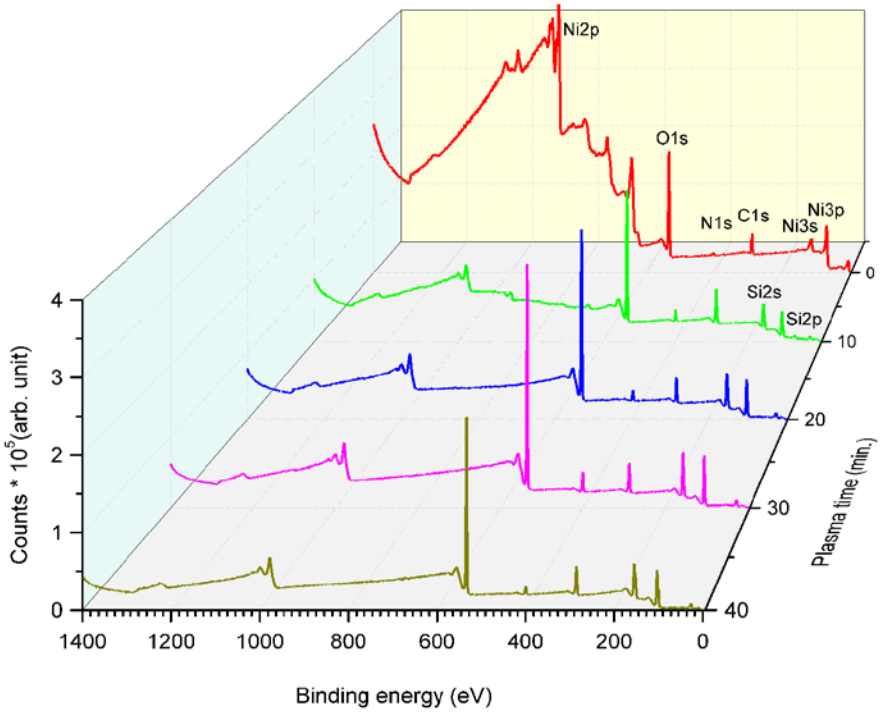

Figure 49. XPS survey spectra of plasma treated samples, indicating diminishing of Ni2p peak (840-890 eV) with plasma treatment time.

Further, XPS survey spectra of 20, 30 and 40 minute plasma-treated samples indicated that there is no Ni metal on the surface of the Si substrate. To investigate the extinction of

Ni layer, XPS depth profile was carried out. For this experiment, 3×3 mm^2 area of the 30 minute plasma-treated sample was sputtered for 3 minutes in each cycle using 2 keV Ar^+ ions and Ni2p, O1s, C1s, N1s and Si2p high resolutions scans were carried out after each sputtering cycle, with a total sputtering time of 104 minutes. Figure 50 shows the depth profile of Ni2p high resolution scans with sputtering time.

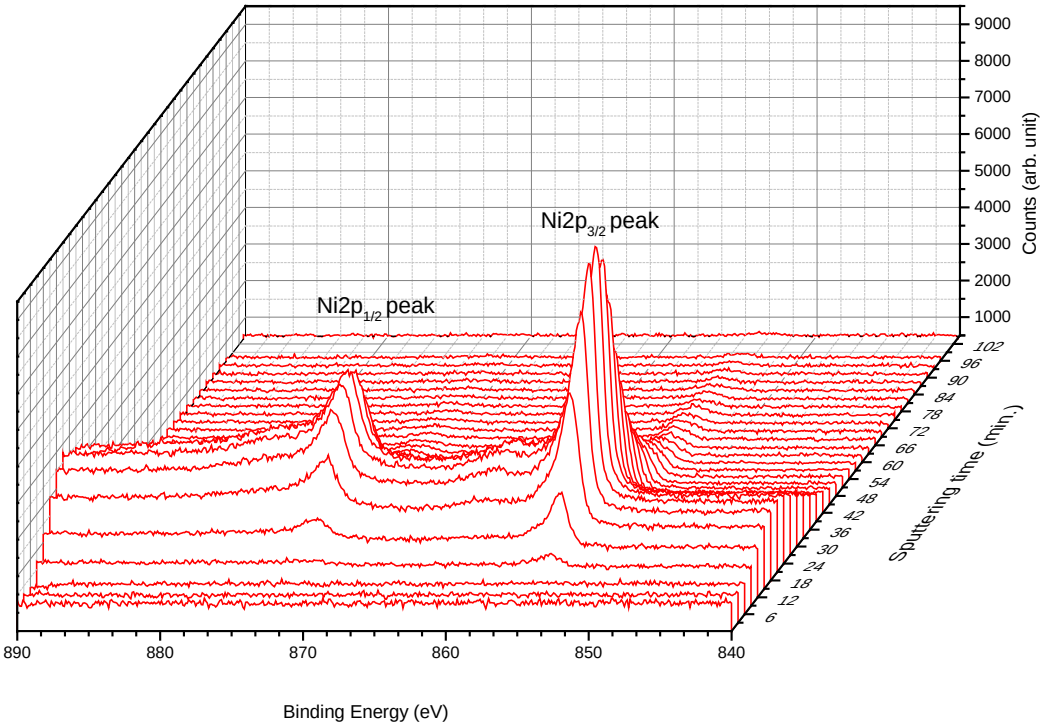

Figure 50. XPS high resolution of Ni2p peak with sputtering time.

Based on these spectra it is revealed that for the first 9 minutes of sputtering, Ni was not detected. From 12 to 78 minutes sputtering time, Ni was detected and the intensity of the peak was gradually increased up to about 24 minutes sputtering time, and after that intensity of the peak diminishing. After 104 minutes sputtering, Ni peak was not

observed. These spectra indicate Ni was diffused into the Si substrate with plasma treatment. The atomic concentration profiles of Ni2p, Si2p, O1s, N1s, and C1s were calculated with sputtering time and shown in

Figure 51. Based on the SRIM simulation [155], the Si substrate is sputtered about 5.2 nm in one sputtering cycle with 2keV Ar^+ ions. Therefore, Ni is diffused into the Si about 52 nm below the surface.

In addition, to investigate the chemical state and chemical composition of diffused Ni into Si, deconvolution of the Ni peaks after 24 and 48 minutes sputtering was carried out. The high resolution Ni2p spectrum of a 30 minute plasma-treated sample after 24 minutes sputtering shows multiple peaks corresponding to Ni, Ni_2Si, $NiSi_2$, and NiSi. The

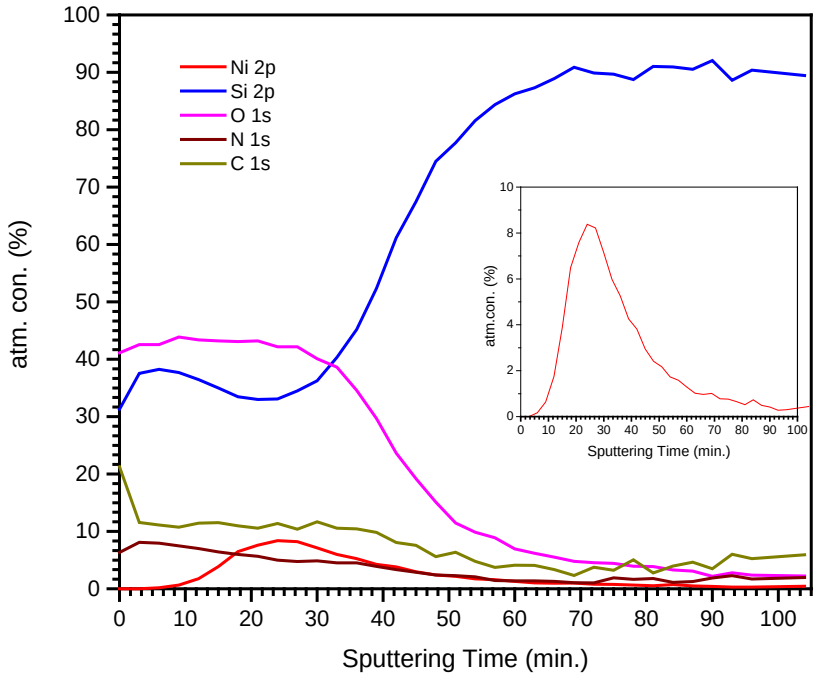

Figure 51. Atomic concentration profiles of Ni, Si, O, N and C with sputtering time for 30 min. plasma treated sample. Inset shows atomic concentration of Ni only.

fitted binding energy peaks located at about 852.55±0.1 eV, 856.40±0.1 eV and 858.40±0.1 eV are the characteristic peaks (pink) for pure Ni. The fitted binding energy curves located at 853.4±0.1 eV (blue), 853.8±0.1 eV (green) and 854.6±0.1 eV (dark yellow) associated with Ni_2Si, NiSi, and $NiSi_2$ respectively [177] [178].

The atomic concentration of Ni, Ni_2Si, NiSi, and $NiSi_2$ at this point were 60.76%, 18.98%, 5.39% and 14.87% respectively. The high resolution spectrum of Si2p of 30 minute plasma-treated sample after 24 minutes sputtering also confirmed the existence of nickel silicide. Figure 52 shows high resolution spectra of Ni2p and Si2p after 24 minutes sputtering. High resolution XPS spectra of Ni2p and Si2p after 48 minutes sputtering showed Ni exists as NiSi. Figure 53 shows high resolution XPS spectra of Ni2p and Si2p after 48 minutes sputtering..

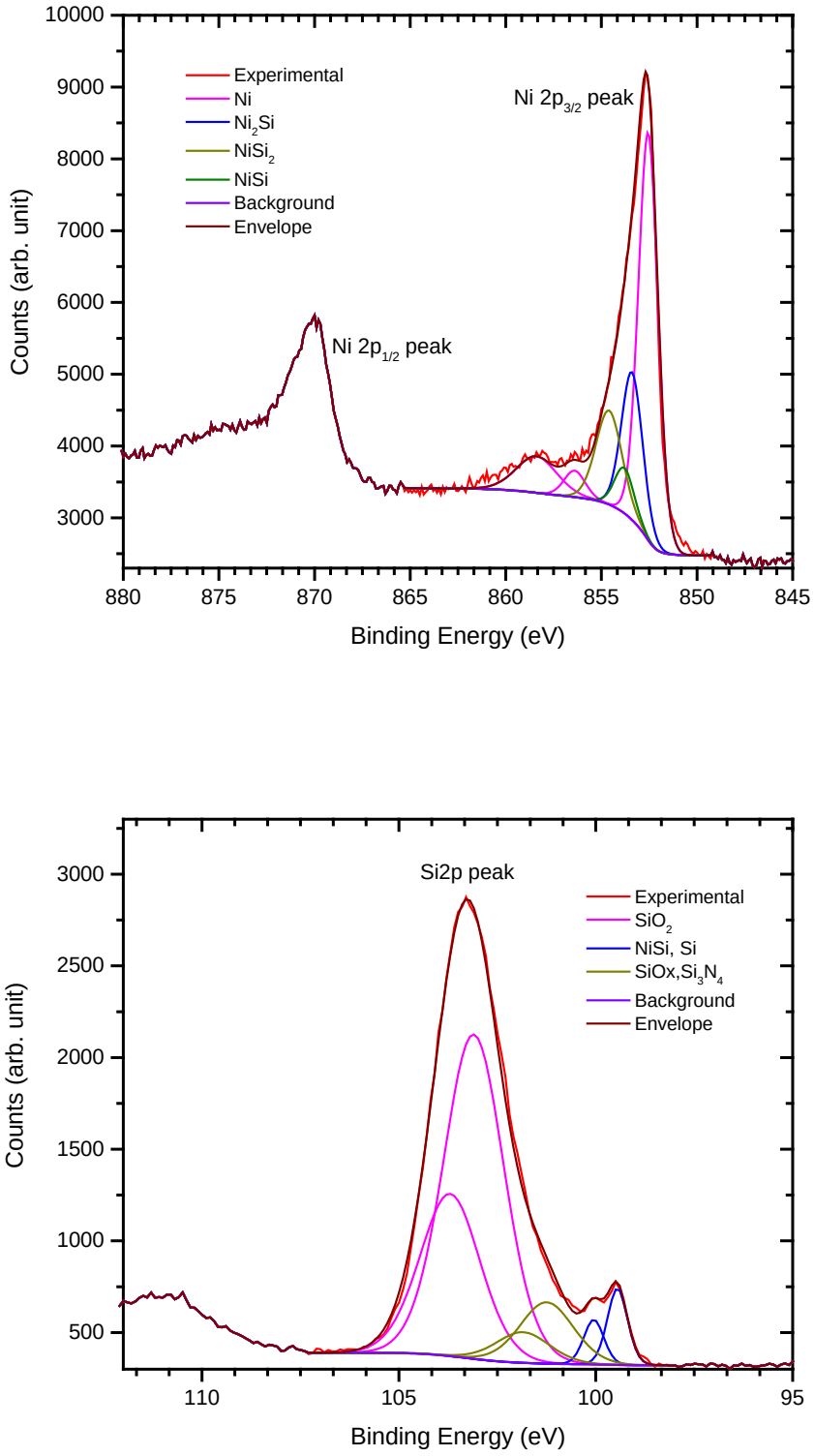

Figure 52. High resolution XPS spectrum of Ni2p (top) and Si2p (bottom) after 24 min. sputtering (30 min. plasma treated sample).

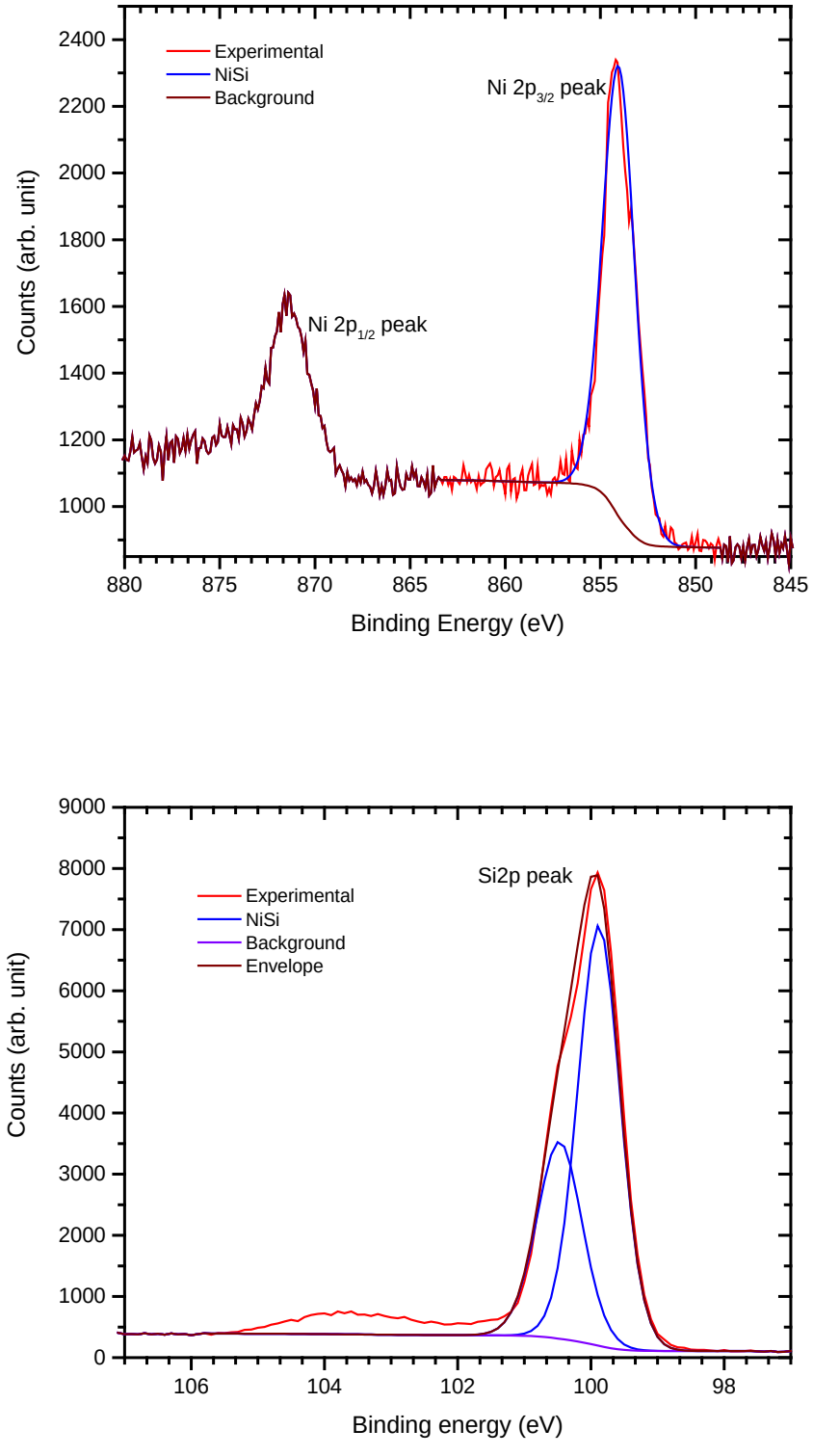

Figure 53. High resolution XPS spectrum of Ni2p (top) and Si2p (bottom) after 48 min. sputtering (30 min. plasma treated sample).

For the Ni catalyst system, it is well understood that upon annealing, formation of metal silicide accompanied by changes in chemical state, composition, and topography takes place when metal is in contact with the Si substrate [179]. Above XRD and XPS results indicated the formation of nano-particles with the Ni core surrounded by metal silicide that could be either due to plasma treatment and/or conditions used for CNT growth. These particles are embedded in the underlying Si substrate, thus reducing the catalytic activity leading to poor CNT or complete inhibited growth [180]. This process is shown in Figure 54. A combination of phenomena, namely formation of silicide, phase transformation of Ni with reduced lattice parameters could have resulted in the diffusion of Ni into the Si substrate, which may have led to such odd formation of CNTs. When Ni diffuses below the surface of Si, it totally transforms to NiSi even though atomic percentage of NiSi is very low.

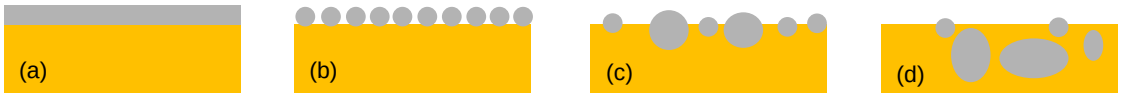

Figure 54. Schematic diagram of (a) Ni thin layer on Si substrate (b) metal nano-particles formation on Si (c) Change in topography, agglomeration and loss of catalytic activity (d) diffusion due to plasma treatment and/or CNT growth process.

Further, RBS experiments were carried out on the as-deposited and the plasma-treated nickel samples to confirm the nickel diffusion into the Si substrate. RBS spectra were collected using 2.0 MeV He^+ with 150° scattering angle. Figure 55 shows the RBS spectra of the as-deposited and the plasma-treated samples. RBS spectra indicate, Ni edges of the plasma-treated samples compared to the Ni edge of the as-deposited sample moved towards the lower channel numbers.

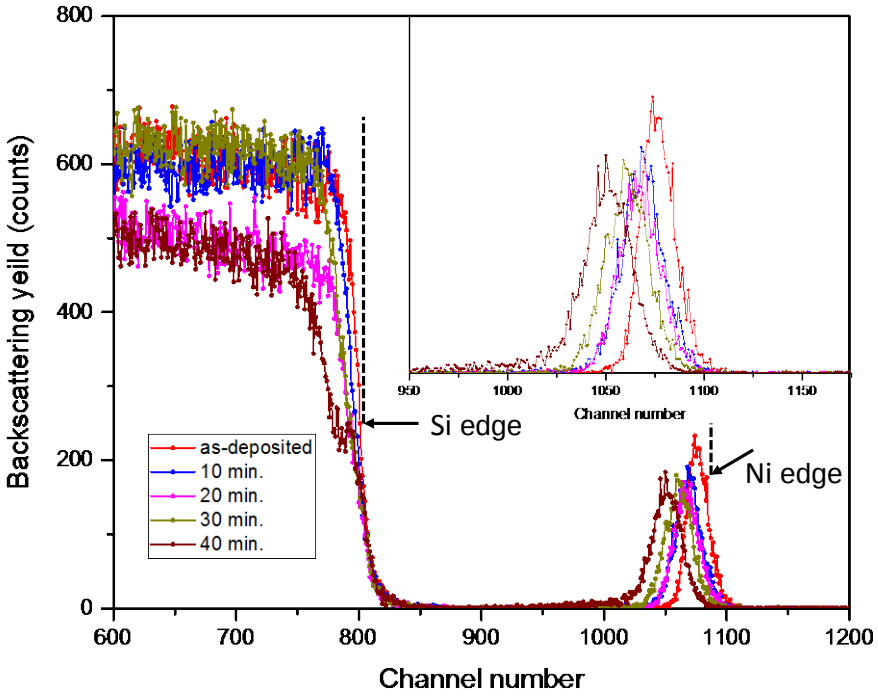

Figure 55. RBS spectra of the as-deposited and the plasma-treated nickel samples. Inset shows the nickel peak.

This is an indication of Ni is diffused into the Si substrate (underneath the surface of the Si substrate). Therefore, the energy of the backscattered He ions from the Ni atoms loses their energy within the Si matrix and appears at the lower energy of the RBS spectrum. The Ni edge of the 30-minute plasma-treated sample is moved towards lower energy about 20 channels with respect to the Ni edge of the as-deposited sample. The standard sample (CdTe) calibration is given about 1.37 keV per channel. Therefore, He^+ ions lose about 27.4 keV energy. The stopping power of He^+ in the Si matrix is 44.25 eV/°A [102]. The diffusion depth was found out to be about 62 nm. This result is comparable with XPS data.

5.6 Surface energy calculation of polyimide substrate

The Young's equation [181] is defined by the balance forces caused by a wet drop on a dry surface. Its current form is as follows,

$$\gamma_s = \gamma_{sl} + \gamma_l \cos\theta \ldots\ldots\ldots\ldots\ldots\ldots\ldots\ldots\ldots\ldots\ldots\ldots\ldots \quad (44)$$

Where, γ_s is the surface energy of a solid, γ_l is surface energy of liquid, γ_{sl}-surface energy corresponding to the solid liquid interface and θ-contact angle. Ownes and Wendt [182] significantly changed the Young's equation by assuming the surface energy of liquid and substrate is composed of two components, namely polar (γ^p) and dispersive (γ^d) components,

$$2\left(\gamma_s^d \gamma_l^d\right)^{0.5} + 2\left(\gamma_s^p \gamma_l^p\right)^{0.5} = \gamma_l(1 + \cos\theta) \ldots\ldots\ldots\ldots\ldots\ldots\ldots\ldots \quad (45)$$

In this experiment two liquids were used as probes for measuring the contact angle, water ($\gamma_l^p = \frac{50.2mN}{m}, \gamma_l^d = \frac{22.6mN}{m}$), and ethylene glycol ($\gamma_l^p = \frac{16.0\,mN}{m}, \gamma_l^d = \frac{32.8\,mN}{m}$). Two linear equations were yielded from these two probe liquids in the form of equation (45) with two unknowns, namely dispersion (γ_s^d) and polar (γ_s^p) components of the substrate, which could easily be solved. The liquid with a dominant polar component should be chosen as one of the measuring liquids and the dispersive liquid as the other one. Then the solution of the equation (45) would be affected as slightly as possible by the errors associated with determination of the polar and dispersive surface energy components of the solid. Figure 56 shows variation of contact angles of probe liquids and surface energy of the polyimide substrate with UVO cleaner time.

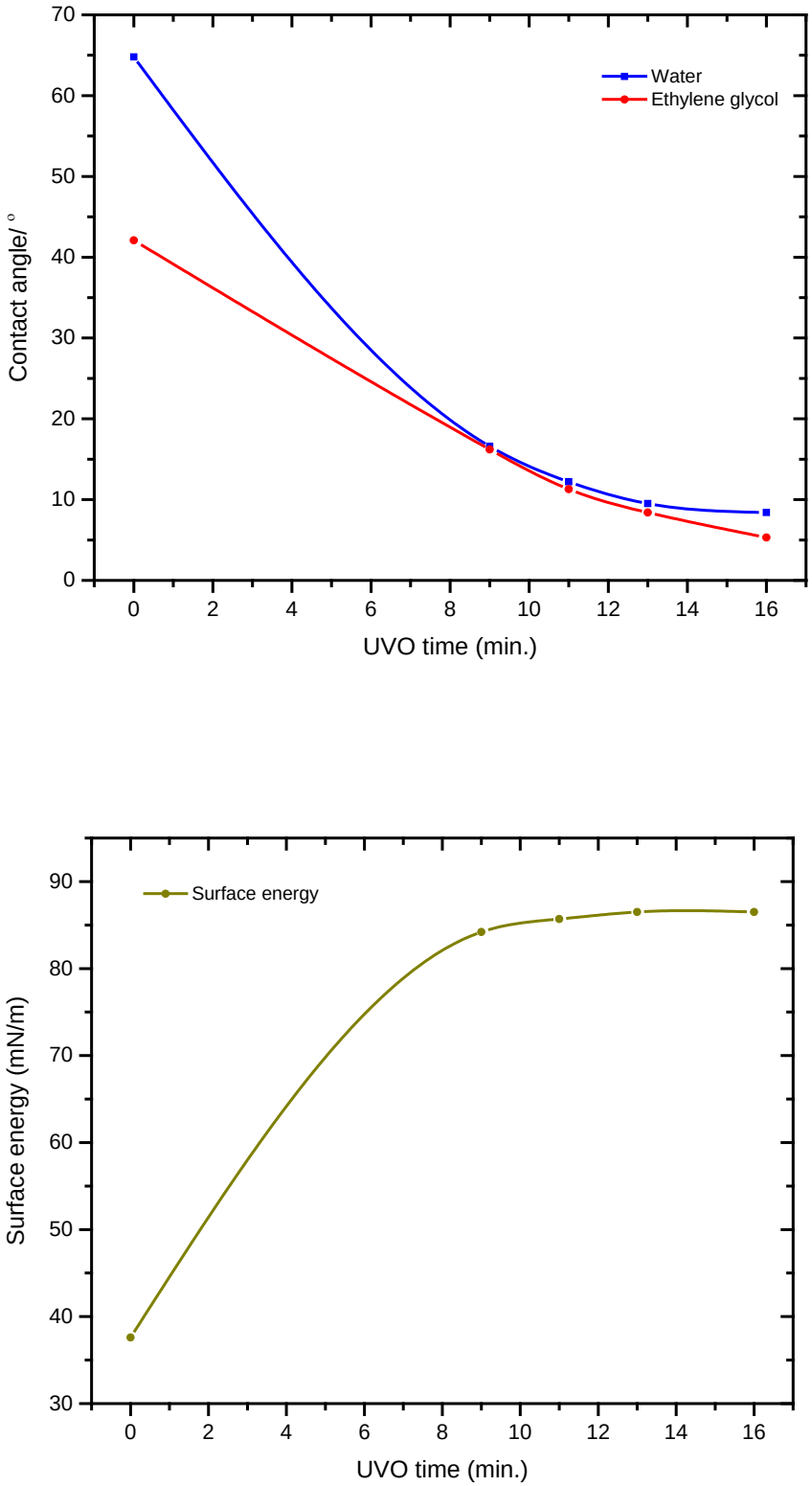

Figure 56. Variation of contact angles of water and ethylene glycol (top) and surface energy of polyimide substrate with UVO cleaner time (bottom).

The variation of surface energy of the substrate with UVO cleaner time is very crucial to determine at which point the surface energy reaches its maximum value. At this maximum surface energy level, the substrate is suitable to synthesize uniform carbon nanotube-polymer composite thin films. For the polyimide substrate, after 16 minutes of UVO plasma treatment, it reaches its maximum surface energy value 86.5mN/m. Figure 57 shows the measuring of contact angle of a water drop on un-treated polyimide substrate.

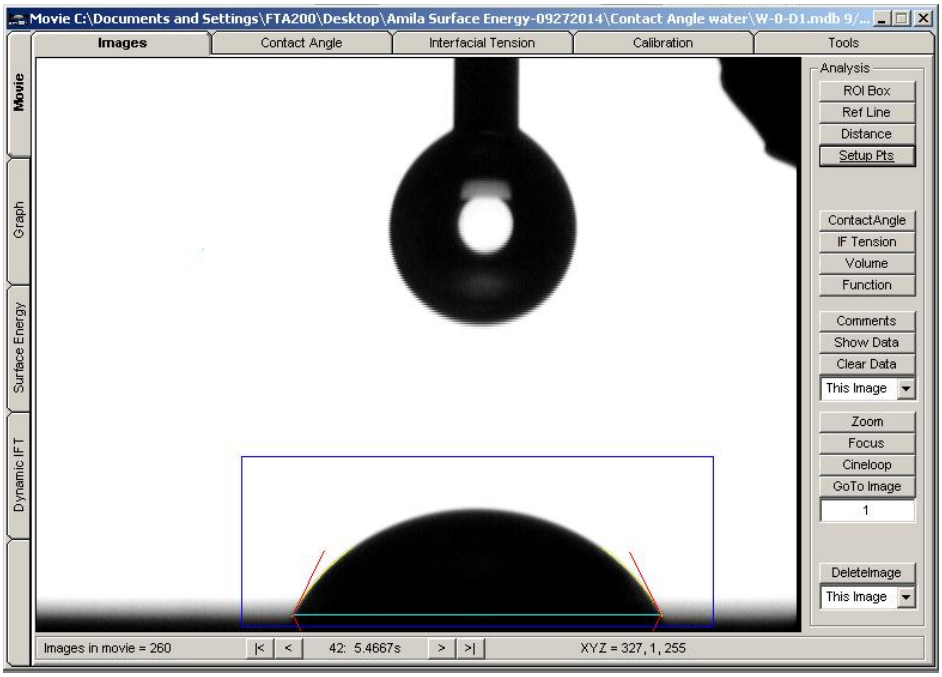

Figure 57. Measuring of contact angle of a water drop on un-treated polyimide substrate.

Atomic force microscopy (AFM) images recorded for polyurethane, 15 wt.% CNT, 15 wt.% CNT with 10 wt.% 1,2,6-Trihydroxyhexane and 15 wt.% CNT with 10 wt.% 2,4,6-trihydroxybenzaldehyde composites thin films are shown in Figure 58.

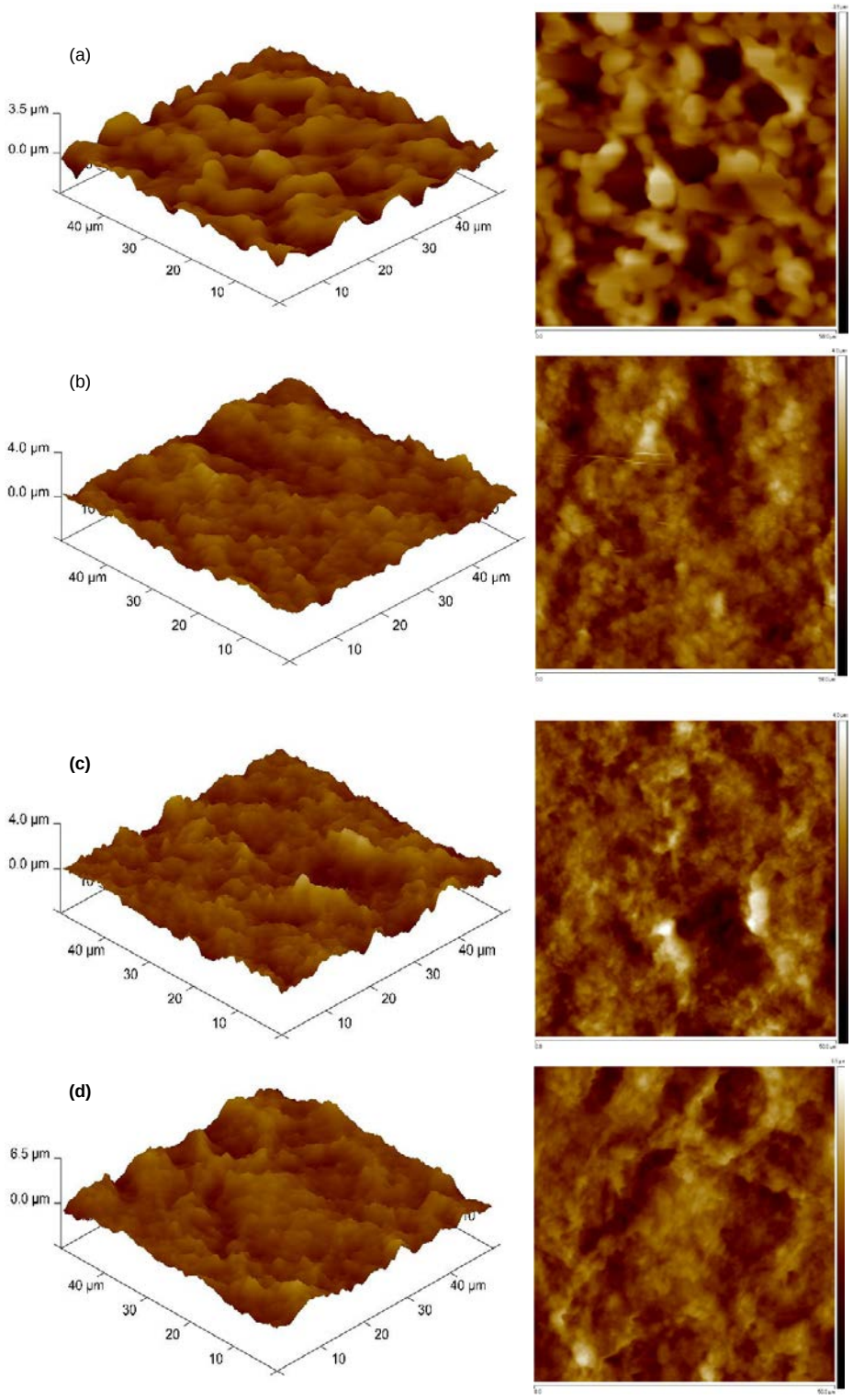

Figure 58. AFM 3D (left) and corresponding 2D (right) images of (a) polymer (b) 15 wt.% loaded CNT and polymer (c)15 wt.% loaded CNT, polymer and 10 wt.% loaded 1,2,6-Trihydroxyhexane cross-linker and (d) 15 wt.% loaded CNT, polymer and 10 wt.% loaded 2,4,6-trihydroxybenzaldehyde cross-linker thin film composite films.

An AFM image of the polymer thin film reveals that polymer film itself is not continuous. It consists of upper boundary 10 μm size pores. Further, composite thin film with 15 wt.% loaded CNT shows less porosity due to strong van der Waals' interaction between CNTs. The same trend goes with the cross-linkers added samples, i.e., less porosity in the samples. The average surface roughness (R_a) values for sample (a), (b), (c) and (d) are found to be 399 nm, 320 nm, 327 nm and 466 nm respectively, indicating very high rough surfaces. The film thickness varied between 1.75 μm and 1.89 μm for the above samples.

5.7 AC conductivity and impedance spectroscopy of carbon nanotube-polymer composite

The log-log plots of absolute impedance ($|Z|$) against frequency (Bode plot) for 1 wt.%, 5 wt.% and 8 wt.% carbon nanotube loaded composites are shown in Figure 59. AC conductivities of these samples were determined based on equation (39). The AC conductivity versus log frequency plots are shown in Figure 60 and with this carbon nanotube content, the maximum value of ac conductivity of the composites reached 3.86 Sm^{-1}, 5.90 Sm^{-1} and 5.38 Sm^{-1} for 1 wt.%, 5 wt.% and 8 wt.% CNTs loaded composite respectively. The obtained ac conductivity values are few orders of magnitude higher than the composites reported in literature [39] [47] [183]. The composites show frequency independent conductivity as frequency increases. This is an indication of composites consisting of measurable DC conductivity which increases at high frequencies. Higher ac conductivity of 1 wt.% loaded CNTs composite indicates the percolation threshold of the composite which occurs at less than at 1 wt.% of CNTs loading. In that case, composite behavior is identical to the conductivity of dielectric materials, i.e., ac conductivity depends on the signal frequency. For dielectric materials,

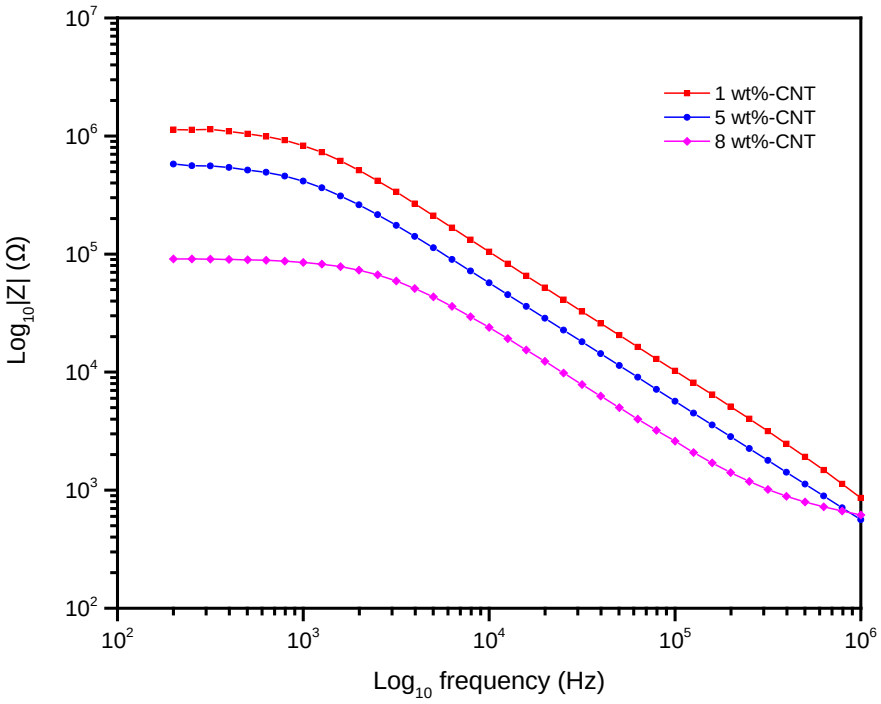

Figure 59. Bode plots of 1 wt.%, 5 wt.% and 8 wt.% carbon nanotube loaded polymer composites.

ac conductivity can be described by the relationship $\sigma = \omega\varepsilon''\varepsilon_o$, where σ is the dielectric conductivity, ω is the angular frequency, ε'' is the imaginary portion of the dielectric constant and ε_o is the vacuum permittivity [184]. Generally, ac conductivity as a function of signal frequency for the above composites shows conductive behavior. This is due to the carbon nanotube network developed with increasing CNTs content in the polymer matrix. The conductivity of the composite depends on growth of the conductive paths. These conductive paths can be divided into two components, called resistive and capacitive paths. Figure 61 (a) shows the capacitive paths dominate at low CNTs concentration and the conductivity at this stage depends on the inter-tube distance and the composite shows capacitive behavior. Figure 61 (b) shows formation of resistive paths in

high CNTs concentration composite and conductivity of these composites depend on nanotube-nanotube contacts. This composite shows frequency independent response as seen in Figure 60 due to increasing the resistive paths and saturation of the resistive paths in this composite.

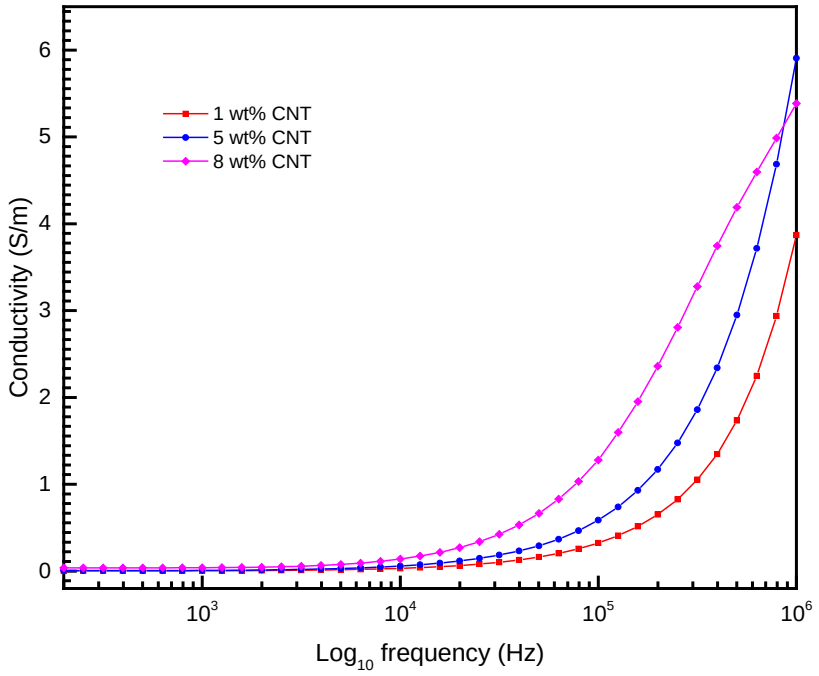

Figure 60. AC conductivity against Log of frequency for carbon nanotube-polymer composite at different percent nanotube weight loading.

5.7.1 Nyquist plot and equivalent circuit modeling

The electrical conductivity and development of the CNT network in the polymer composite can be divided into three categories. At low CNTs loading, the inter-tube distance is large and electrons transmission is very low, therefore the composite may have conductivity comparable to that of an insulating polymer. At the percolation state, the inter-tube distance is close and the electrons must overcome the potential barrier to cross the inter-tube distance. Simply, there is a limited contact resistance R_c for the electron channel in the inter-tube distance [184]. This inter-tube distance can be deduced to a parallel-plate capacitor with area A, separation distance d, and capacitance $C = {\varepsilon A}/{d}$, where ε is the dielectric constant of the polymer. Each nanotube or nanotube aggregate has a resistance R_a. An equivalent circuit for the small area of the composite can be represented as shown in Figure 62. Impedance for the equivalent circuit shown in Figure 62 can be written as follows,

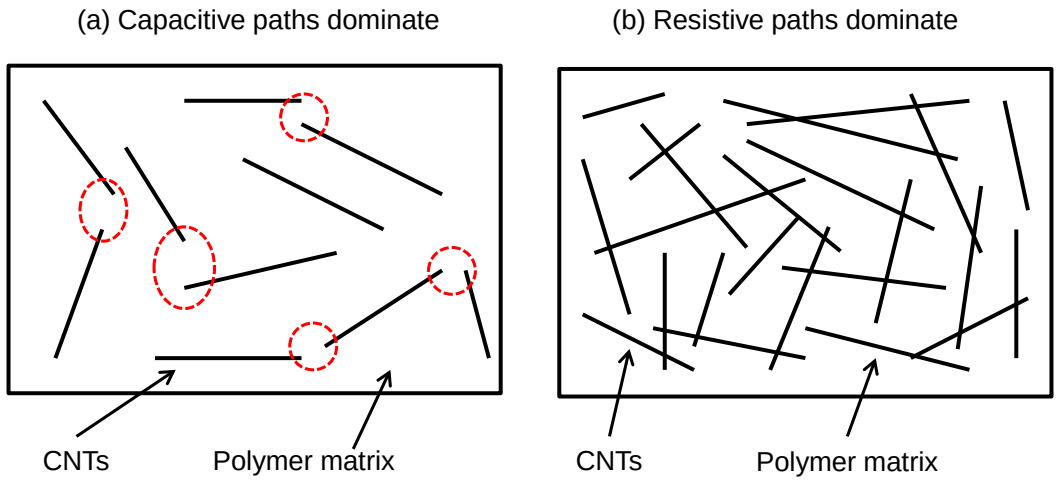

Figure 61. Schematic diagram of occurrence of (a) capacitive paths and (b) resistive paths at low and high CNTs loading regions respectively.

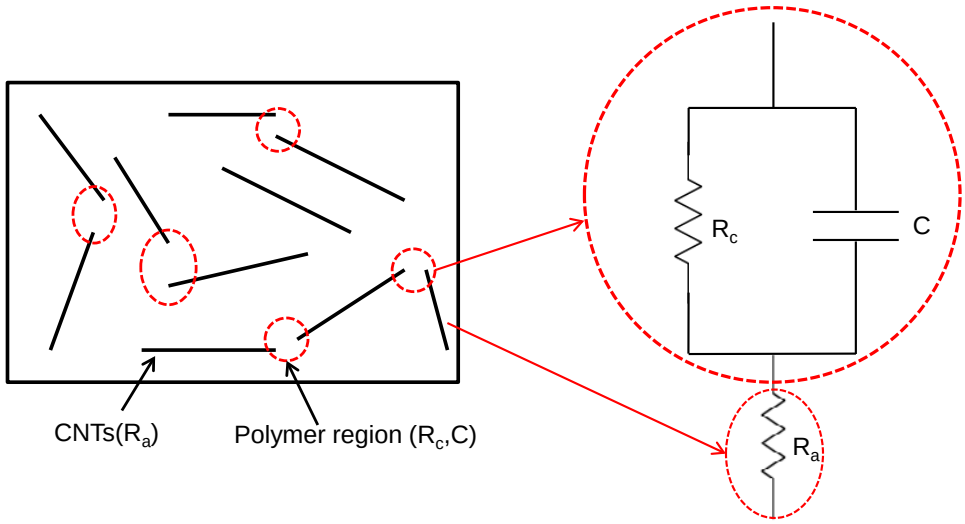

Figure 62. Equivalent circuit model with resistors and capacitor for explaining Nyquist plot of 1 wt.%, 5 wt.% and 8 wt.% CNTs loaded composites.

$$Z = R_a + \frac{R_c}{1+\omega^2 R_c^2 C^2} - j\frac{\omega R_c^2 C}{1+\omega^2 R_c^2 C^2} \quad \text{(46)}$$

Equation (46) can be divided into two sections, called real ($Re(Z)$) and imaginary ($Im(Z)$) parts.

$$Re(Z) = R_a + \frac{R_c}{1+\omega^2 R_c^2 C^2} \quad \text{(47)}$$

$$Im(Z) = -\frac{\omega R_c^2 C}{1+\omega^2 R_c^2 C^2} \quad \text{(48)}$$

From equation (47) and (48) absolute value of the impedance ($|Z|$) and phase angle can be obtained as follow,

$$|Z| = \left(R_a^2 + \frac{R_c^2 + 2R_c R_a}{1+\omega^2 R_c^2 C^2}\right)^{1/2} \quad \text{(49)}$$

phase angle,

$$\tan\varphi = \frac{Im(Z)}{Re(Z)} = -\frac{\omega^2 R_c^2 C}{R_a + R_c + \omega^2 R_c^2 R_a C^2} \ldots\ldots\ldots\ldots\ldots\ldots\ldots\ldots\ldots\ldots\ldots\ldots\ldots\ldots\ldots \quad (50)$$

From equation (47) and (48), a relationship between $Re(Z)$ and $Im(Z)$ can be obtained as following equation,

$$\left(Re(Z) - \frac{2R_a + R_c}{2}\right)^2 + Im(Z)^2 = \left(\frac{R_c}{2}\right)^2 \ldots\ldots\ldots\ldots\ldots\ldots\ldots\ldots\ldots\ldots\ldots\ldots\ldots\ldots\ldots \quad (51)$$

Equation (51) represents a circle which has a center at $\left(\frac{2R_a+R_c}{2}, 0\right)$ and radius $\frac{R_c}{2}$. Therefore, plotting $Im(Z)$ against $Re(Z)$ gives a half circle with a center and radius mentioned above. In Nyquist plot the semi-circle curve occurs only in the case of a parallel resistor-capacitor (RC circuit). The parallel RC circuit can be used to confirm the existence of the capacitor effect, i.e., gaps between CNTs which controlled the electrical conduction through tunneling. Figure 63 shows Nyquist plot of 1 wt.%, 5 wt.% and 8

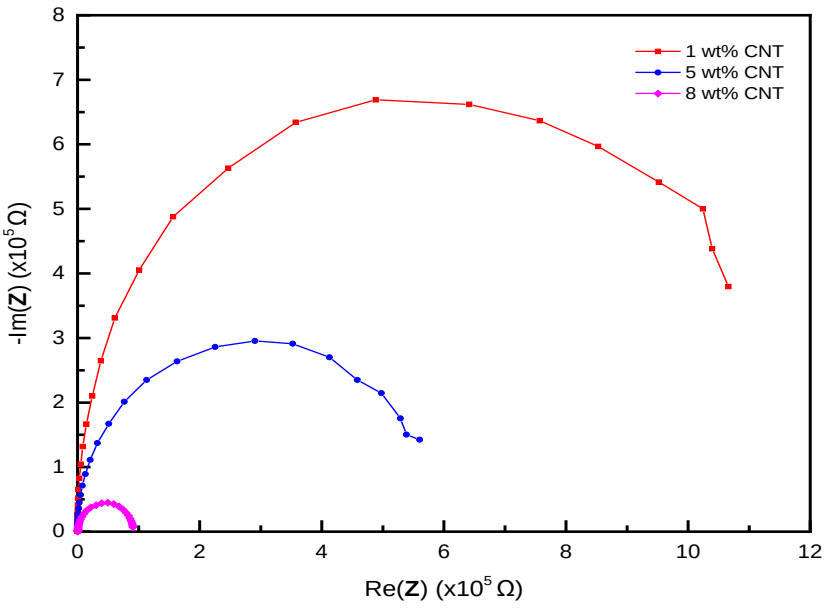

Figure 63. Nyquist plots of 1 wt.%, 5 wt.% and 8 wt.% CNTs loaded composites.

wt.% CNTs loaded composites.

Figure 64 shows a simulated Nyquist plot using equivalent RC-circuit modeling and experimental data for 5 wt.% CNTs loaded composite. As mentioned above, it confirms the existence of gaps between CNTs controlling ac electrical conduction via electron tunneling between the gaps.

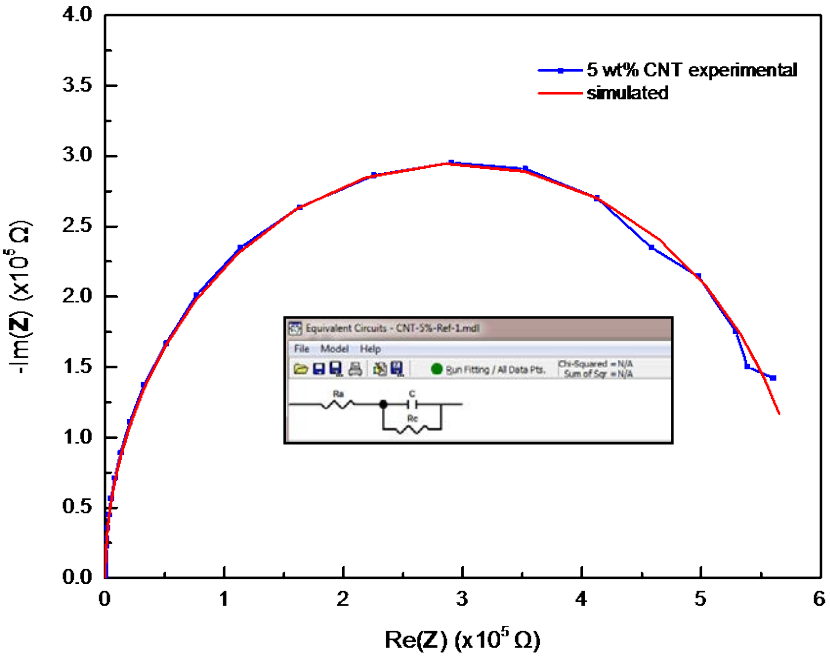

Figure 64. Experimental and simulated Nyquist plot of 5 wt.% CNTs loaded composite. Inset picture shows equivalent RC-circuit model used to simulate the experimental data.

Equivalent RC-circuit modeling was carried out for all three samples mentioned above and R_a, R_c and C values were determined from the simulation. Equation (10) and R_a values determined from the simulation were used to calculate the conductivity of the

CNTs σ_{cnt} and the result is summarized in Table 6. The average diameter of the nanotube is about 6.6 nm and the length is about 5 μm (based on vendor specification).

Table 6: Equivalent RC-circuit model estimated parameters for CNT-polymer composites with CNT conductivity.

Composite	$R_a(\Omega)$	$R_c(\Omega)$	C(F)	σ_{cnt}(S/m)
1 wt.%	433.60	1.31×10^{6}	1.57×10^{-10}	3.37×10^{8}
5 wt.%	19.49	5.89×10^{5}	2.79×10^{-10}	1.50×10^{9}
8 wt.%	493.40	8.89×10^{4}	6.17×10^{-10}	2.96×10^{8}

The estimated CNT conductivity value is about ten times higher than the value reported in literature [185]. To compare the tunneling resistance values in Table 6, the theoretical tunneling resistance value was determined from equation (21).

$$R_{tunnel} = \frac{V}{AJ} = \frac{h^2 d}{Ae^2\sqrt{2m\lambda}} \exp\left(\frac{4\pi d}{h}\sqrt{2m\lambda}\right)$$

The parameters in the equation were defined in the section 2.5 and assuming potential barrier for polyurethane is 4.0 eV [186], the cross sectional area of the CNT as an approximation of the cross section of tunneling area A, and the maximum tunneling resistance was found to be 5.45×10^{8} Ω for a maximum tunneling distance of 0.7 nm. Generally, in carbon nanotube-polymer composites tunneling resistance dominate electrical resistance occurred when the inter-tube distance is less than 1.8 nm [52]. These results confirm that the equivalent parallel RC-circuit model can be used to estimate σ_{cnt} and the inter-tube tunneling resistance above the percolation threshold.

5.7.2 CNT-polymer composite with cross-linkers

Figure 65 shows the conductivity of 1 wt.% and 5 wt.% loaded carbon nanotube-polymer composites with 10 wt.% loaded 1,2,6-trihydroxyhexane and 2,4,6-trihydroxybenzaldehyde cross-linkers. The maximum conductivities of the 1 wt.% loaded

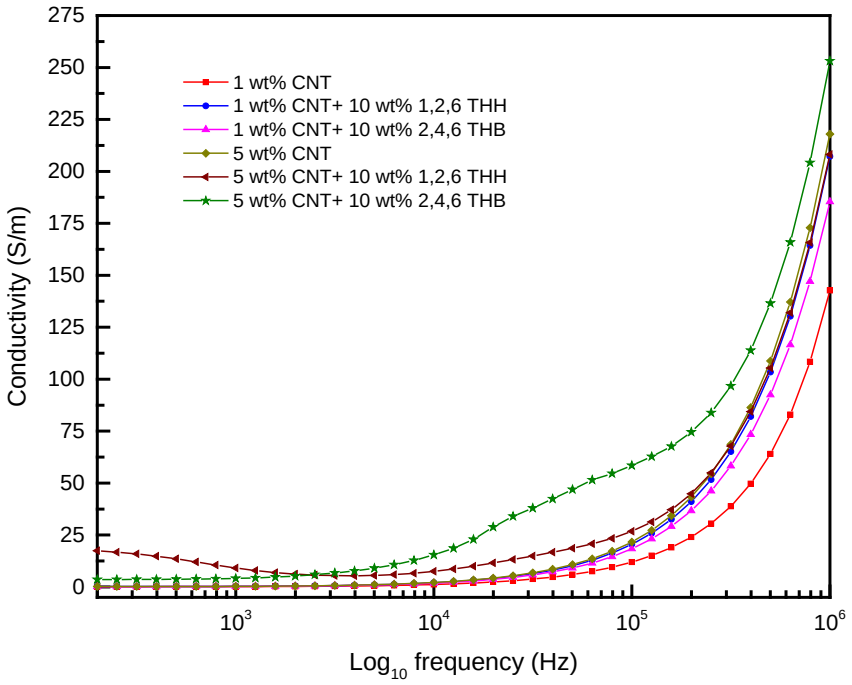

Figure 65. AC conductivity vs Log of frequency for carbon nanotube-polymer composite at different percent nanotube weight loading with 10 wt.% of 1,2,6-trihydroxyhexane and 2,4,6-trihydroxybenzaldehyde cross-linkers.

CNTs with 10 wt.% of 1,2,6-trihydroxyhexane and 2,4,6-trihydroxybenzaldehyde at 10^6 Hz were 207.17 Sm^{-1} and 185.41 Sm^{-1} respectively when compared to the conductivity value of 142.69 Sm^{-1} equivalent composite without cross-linkers. This enhancement in the conductivity could be due to agglomeration of CNTs in the polymer matrix due to the

effect of cross-linkers, i.e., cross-linkers attempts to hold the polymer chain together closely and at the same time CNTs are tangled within these chains and make agglomerations. The development is more or less the same for composites with 5 wt.% loaded CNTs with 10 wt.% cross-linkers. The maximum conductivities of the 5 wt.% loaded CNTs with 10 wt.% 1,2,6-trihydroxyhexane and 2,4,6-trihydroxybenzaldehyde at 10^6 Hz were 208.13 Sm^{-1} and 253.11 Sm^{-1} respectively when compared to the conductivity value of 217.94 Sm^{-1} counterpart composite without cross-linkers. The difference in dispersion state is observed in the different in ac conductivity response. The ac conductivity for 5 wt.% loaded CNTs composites with cross-linkers shows a 'hump' in the 10^4 to 10^5 Hz frequency range. This feature is absent in the low content (1 wt.%) of CNT-polymer composite with cross-linkers. This behavior implies that the dispersion state of the CNTs within the polymer matrix has influence on the ac conductivity of the composite. Figure 66 shows the Nyquist plots of 1 wt.% and 5 wt.% CNTs loaded composite with 10 wt.% 1,2,6-trihydroxyhexane. The experimental data of a composite with low CNTs content (1 wt.%) can be modeled using equivalent parallel RC-circuit as earlier. But for the composite with higher CNTs content (5 wt.%), the equivalent circuit model developed for composites without cross-linkers could not model the ac conductivity results. Therefore, a different model was developed for this sample. The simulated data show the existence of two conducting regions for this higher CNTs content sample (Figure 66 (bottom)). Based on the equivalent circuit model, it is revealed that the composite contains isolated agglomerates of nanotubes surrounded by large areas of insulating matrix. The other region was able to model using a simple parallel RC-circuit as before indicating that region consists of well dispersed CNTs with gaps

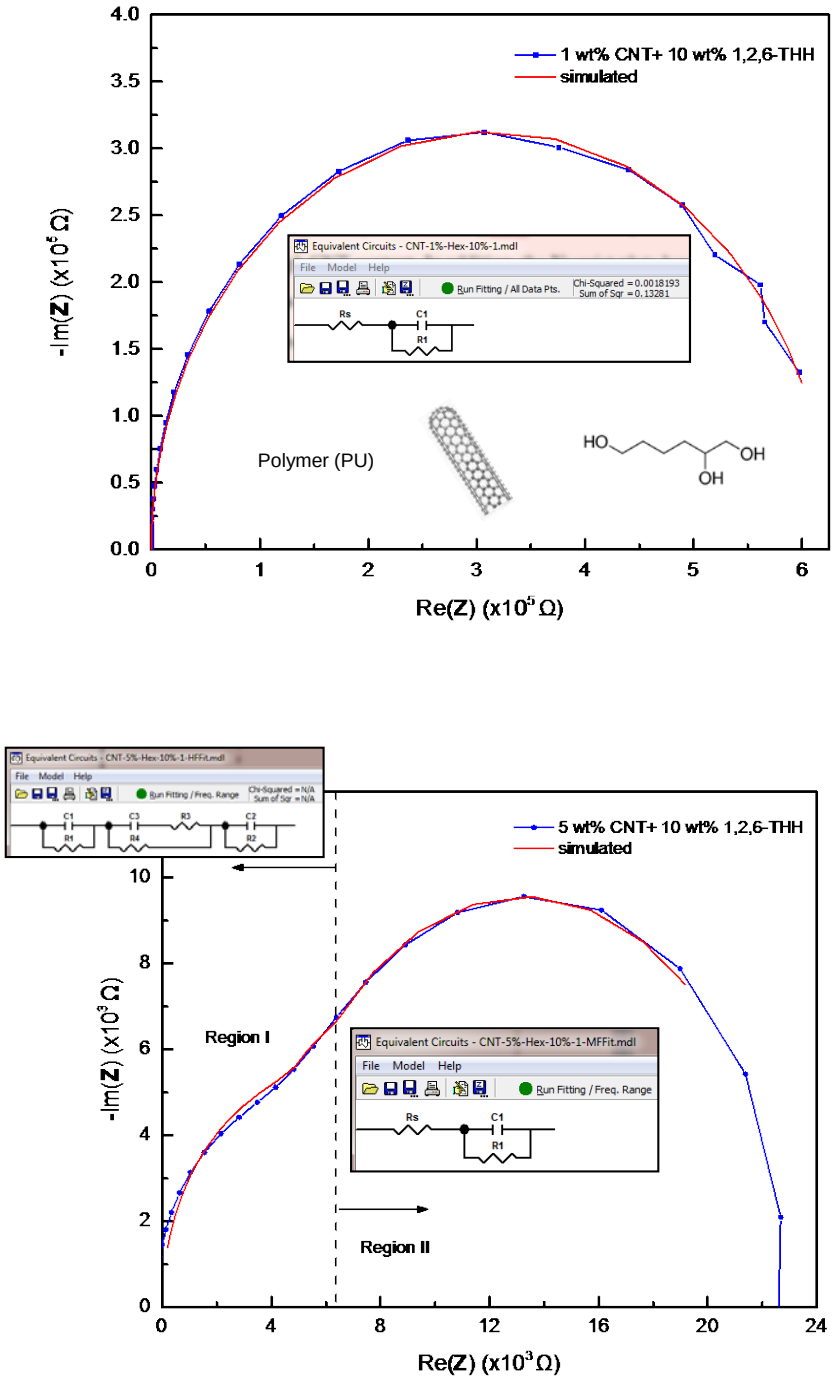

Figure 66. Nyquist plots of 1 wt.% (top) and 5 wt.% (bottom) CNTs loaded composite with 10 wt.% 1,2,6-trihydroxyhexane. Inset diagrams show equivalent circuit model for simulating experiment data.

between them. The size of the agglomerations was dependent on the weight percentage of the CNTs. There is no such effect in the lower content CNTs composite. In this model, the areas of polymer matrix between CNTs agglomerates were represented as parallel RC-circuit. Further, by assuming the polymer matrix was infiltrated into CNTs agglomerates, a parallel circuit with resistive and capacitive path was used as shown in Figure 67. R_1, R_2, C_1 and C_2 are the equivalent resistance and capacitance in the polymer matrix between agglomerates. R_2 and C_2 represent the resistance and the capacitance of the capacitive paths within the agglomerates and R_3 represents the equivalent resistance of the resistive paths in the agglomerates. For the equivalent circuit shown in Figure 67, the impedance can be written as follows,

$$Z = \frac{R_1}{1+\omega^2 R_1^2 C_1^2} + \frac{R_2}{1+\omega^2 R_2^2 C_2^2} + \frac{\omega^2 R_4 R_3 C_3^2 + \omega^2 R_3^2 C_3^2 + 1}{R_4(1+R_3^2 C_3^2)} - j\left[\frac{\omega R_1^2 C_1}{1+\omega^2 R_1^2 C_1^2} + \frac{\omega R_2^2 C_2}{1+\omega^2 R_2^2 C_2^2} - \frac{\omega C_3}{1+R_3^2 C_3^2}\right] \ldots\ldots\ldots\ldots\ldots\ldots\ldots \quad (52)$$

The real and imaginary impedance can be written as follows,

$$Re(Z) = \frac{R_1}{1+\omega^2 R_1^2 C_1^2} + \frac{R_2}{1+\omega^2 R_2^2 C_2^2} + \frac{\omega^2 R_4 R_3 C_3^2 + \omega^2 R_3^2 C_3^2 + 1}{R_4(1+R_3^2 C_3^2)} \ldots\ldots\ldots\ldots \quad (53)$$

$$Im(Z) = -\omega\left[\frac{R_1^2 C_1}{1+\omega^2 R_1^2 C_1^2} + \frac{R_2^2 C_2}{1+\omega^2 R_2^2 C_2^2} - \frac{C_3}{1+R_3^2 C_3^2}\right] \ldots\ldots\ldots\ldots\ldots\ldots\ldots\ldots \quad (54)$$

From equations (53) and (54), the absolute value of impedance and phase angle can be determined as $|Z| = (Re(Z)^2 + Im(Z)^2)^{1/2}$ and $\tan\varphi = Im(Z)/Re(Z)$ respectively. The equivalent circuit model parameters determined for low and high content CNTs with 1,2,6-trihydroxyhexane cross-linker composite are summarized in Table 7.

Table 7: Equivalent circuit parameters determined for low and high content CNTs with trihydroxyhexane cross-linker.

Composite	$R_s(\Omega)$	$R_1(\Omega)$	$C_1(F)$	$R_3(\Omega)$	$R_4(\Omega)$	$C_3(F)$
1 wt.% CNT+ 10 wt.% 1,2,6-trihydroxyhexane	17.56	6.26×10^{5}	2.644×10^{-10}	-	-	-
5 wt.% CNT+ 10 wt.% 1,2,6-trihydroxyhexane	3710	1.91×10^{4}	8.07×10^{-10}	1.64×10^{-7}	6178	3.58×10^{-10}

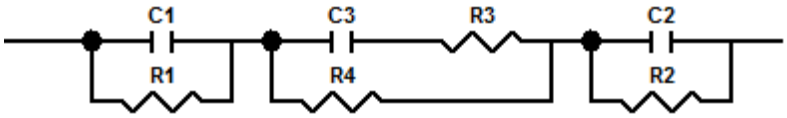

Figure 67. An equivalent resistor-capacitor model for composite with agglomerated CNTs.

The composites with cross-linkers show higher conductivity compared to the composites without any cross-linkers as mentioned before. Now this phenomenon can be understood from the dispersion form of CNTs in the polymer. The polymer regions between the agglomerates increase the conductivity due to homogenous dispersion of CNTs in that region and at the same time agglomerates show higher conductivity due to close packing of CNTs. Hence overall conductivity of the composites was improved because of the above mentioned phenomenon.

The same development can be seen in the composite synthesized with 2,4,6-trihydroxybenzaldehyde cross-linker, i.e., for the low content (1 wt.%) CNTs composite shows a simple equivalent parallel RC-circuit model. For the higher content (5 wt.%) CNTs composite shows similar behavior to its counterpart composite with

trihydroxyhexane cross-linker. Figure 68 shows Nyquist plots of low and high content CNTs composite with 2,4,6-trihydroxybenzaldehyde cross-linker.

5.8 Strain measurements

The strain measurement on the CNT-polymer composite (8 wt.% CNT) was carried out using the National Instruments SCXI expansion chassis with a SCXI-1520 module, a quarter bridge beam and a LabVIEW program. First, silver electrodes were deposited on a CNT-polymer composite thin film using a thermal evaporator with a separation of 0.5 mm as shown in Figure 69 (a). Secondly, a composite with electrodes was mounted on the aluminum beam as shown in Figure 69 (b). Next, ohmic contacts were connected to the two electrodes separate at a distance 0.5 mm. Then this aluminum beam was attached to a cantilever. The ohmic connections from the composite were connected to the quarter bridge configuration as shown in Figure 69 (c). One contact from the composite was connected to the QTR terminal and the other one was connected to the P+ terminal of the quarter bridge. The QTR terminal and S+ terminal were shorted, since there is no third connection from the sensor. Finally, the LabVIEW program shown in Figure 69 (d) was used to measure the strain, by applying a 0.2 Kg tensile force on the aluminum beam. A typical strain response from the composite was observed in the range of 519-521 micro-strains as shown in Figure 70. Although, a strain response was observed from the composite, the DC resistance of this film was very high (~ 15 kΩ). To obtain a better strain response from these composites, experimental parameters such as type of polymer, CNT loading, type of CNTs etc., are needed to be improved further.

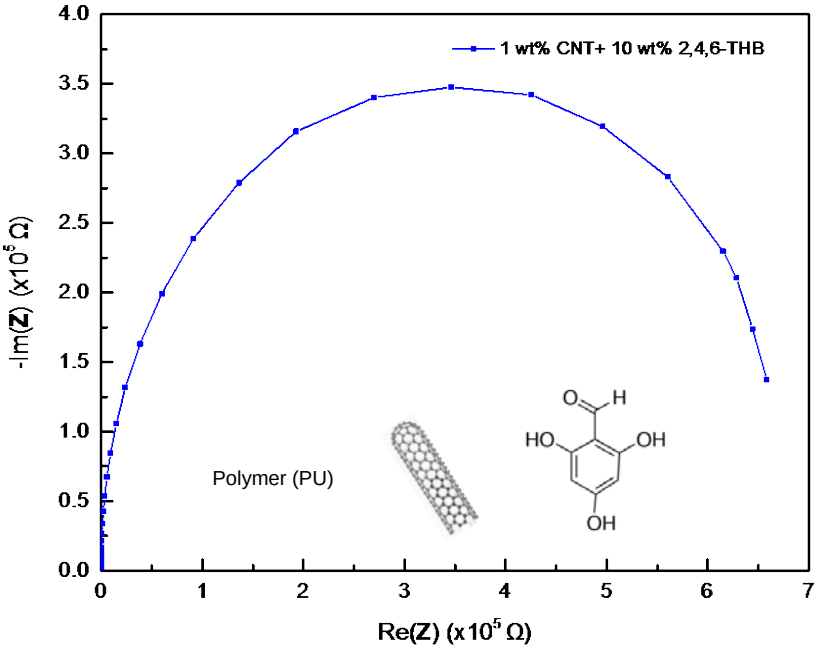

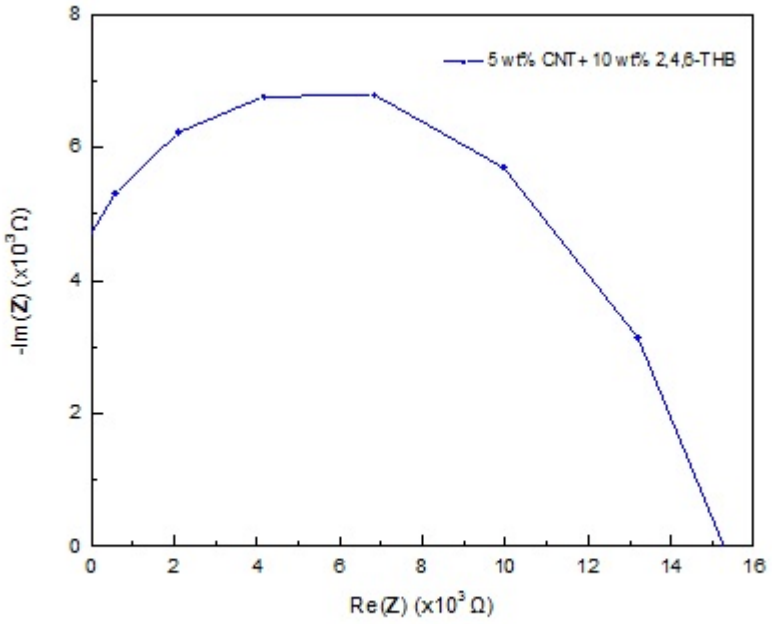

Figure 68. Nyquist plots of 1 wt.% (top) and 5 wt.% (bottom) CNTs loaded composite with 10 wt.% 2,4,6- trihydroxybenzaldehyde.

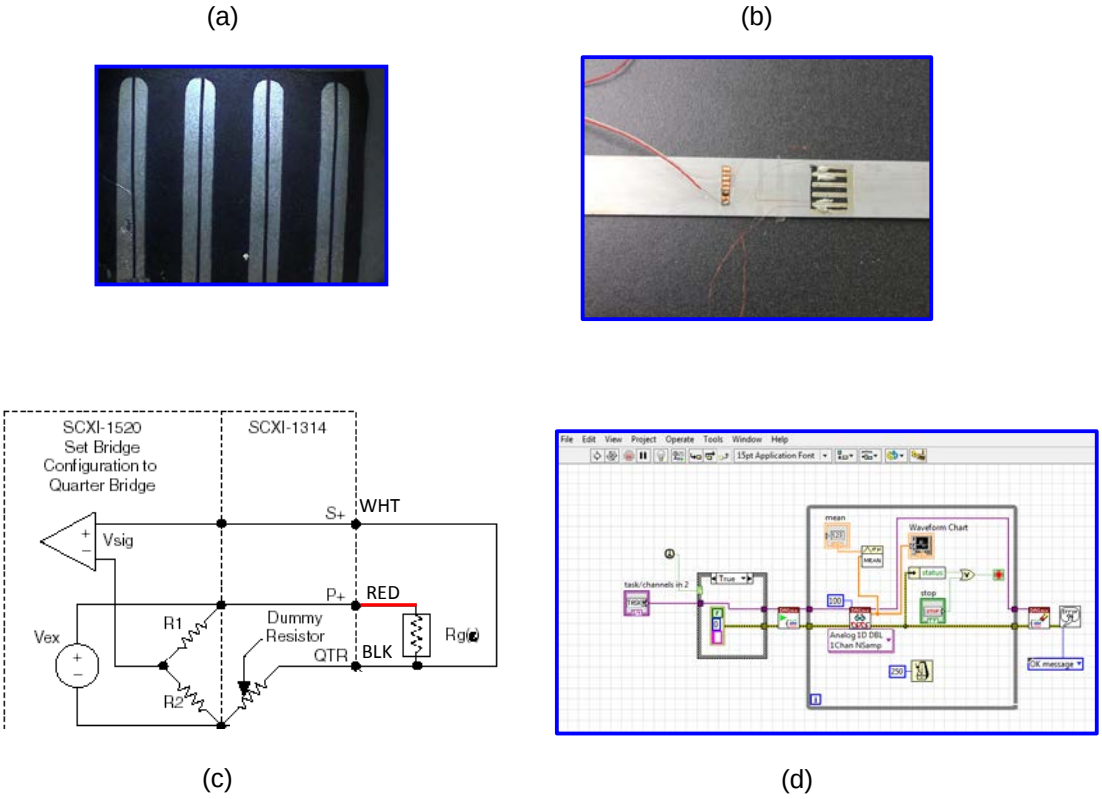

Figure 69. A picture of (a) silver electrode deposited CNT-polymer composite (b) composite with electrodes mounted on aluminum beam (c) quarter bridge configuration (d) LabVIEW software to obtain strain measurements.

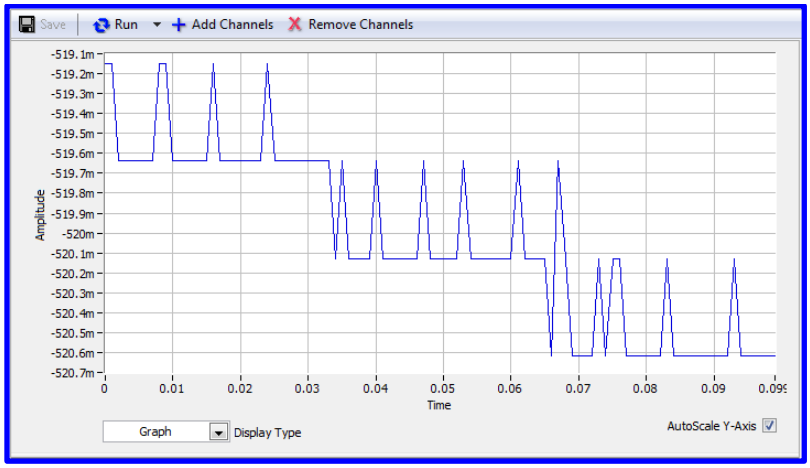

Figure 70. The strain response from the CNT-polymer composite (8 wt.% CNT).

CHAPTER 6

CONCLUSIONS

In this study, the influence of growth conditions of carbon nanotubes (CNTs) on the Si substrate, and the synthesis parameters of novel carbon nanotube-polymer composite in terms, and electronic and mechanical properties for strain sensor applications were explored. Carbon nanotube forests were grown on an Si (100) substrate with a thin Ni catalyst layer by plasma-enhanced chemical vapor deposition (PECVD) to establish optimum growth conditions for carbon nanotube films. The Ni catalysts layer thickness was optimized at 4 nm per minute to obtain catalyst thin films thickness required for carbon nanotube growth at 200 sccm of Ar gas flow rate and about 10^{-3} Torr chamber pressure. The Ni catalyst-deposited Si substrates were annealed at 600 °C in a hydrogen environment for 60 minutes followed by the hydrogen plasma treatment for 30 minutes to create Ni nano-islands. The growth of CNTs was performed immediately after the hydrogen plasma treatment using a mixture of hydrogen (H_2), methane (CH_4) and argon (Ar) gasses at the same temperature with different combinations of gas flow rates for another 30 minutes to optimize the nanotube growth. The results and the conclusions of this study are summarized in the following sections.

6.1 Influence of plasma treated and deposition time on growth of carbon nanotube

The Raman spectra of carbon nanotubes deposited on the Si (100) substrate show variations in D and G positions of the bands and higher value for I_D/I_G ratios. By

analyzing the Raman spectra, it is also learned that less amount of hydrocarbons and higher amount of argon gas environment is much suited for CNT growth. In addition, the broadening (higher FWHM) of the D- and G-bands indicates an amorphous nature of growth nanotubes. This amorphous nature of the growth nanotube is further confirmed by the SEM images. XPS survey spectrum of a 30 minute plasma-treated sample, which was used to deposit carbon nanotubes, shows there is no Ni metal on the Si surface. The nickel layer disappeared from the Si surface. The XPS depth profile of the 30 minute plasma-treated sample shows Ni is diffused into the Si substrate. The experimental observations from the Raman, SEM, and XPS techniques explain the odd growth of carbon nanotube on the Si substrate, i.e., with a higher plasma treatment time and the deposition time Ni thin film granulate into nano-size island and nano-island conglomerate into larger size-island diffused into the substrate leaving few catalysts islands on the surface. This process is further confirmed by the SEM images of the Ni catalyst layer exposed to different plasma treatment times. For 10 minute plasma-treated sample consists of much smaller nano-islands with even distribution on the substrate surface. But the 20, 30 and 40 minute plasma-treated samples show conglomeration of catalyst particles with time into much bigger islands. Therefore, without any catalyst particles or with a larger conglomerated catalyst on the substrate surface it is impossible to grow carbon nanotube either with *tip growth* or *base growth* mechanisms. In addition, the XPS depth profile shows the formation of nickel silicide which loses the catalytic activity due to plasma treatment and/or nanotube growth. The factors mentioned above individually or collectively affected the growth of crystalline carbon nanotubes. Therefore, to prevent inter mixing of catalyst layer and the substrate, metal (Al, Ti, Ta or W) or insulating

(SiO_2) under-layer can be used. Thermodynamics and kinetic studies show that alloying a catalyst with a non-catalytic metal would increase the reactive sites. Also, metal under layer may allow tuning the conductivity of the substrate and the carbon nanotubes. Further, it is learned that based on the SEM images of catalyst layers exposed to different plasma treatment time, about 10 minute plasma-treatment time is sufficient to make a catalyst layer into nano-islands and about 5-6 minutes growth time is sufficient to obtain well grown crystalline carbon nanotubes. If the 10 minute plasma-treated samples were used to synthesize carbon nanotubes, then hopefully it has partially embedded catalyst nanoparticles with pure Ni and/or surrounded by metal silicide would have got much better or massive growth of CNTs which requires to our experiment. Further, the investigations on the effect of annealing temperature on the catalyst layers, gas flow rates, catalyst layer thickness, power of plasma source, buffer layer between the substrate and the catalyst layer, and other transition metal as a catalyst are subjected to future work.

6.2 Synthesis and characterization of carbon nanotube-polymer composite

In this investigation, the electrical and mechanical properties of electrically conductive carbon nanotube-polymer thin film composites were studied. In this study, polymer (polyurethane) was dissolved in 1-Methyl-2-pyrrolidinone (NMP). This solution was loaded with a carbon nanotube with different weight percentage 1 wt.%, 5 wt.%, 8 wt.% ,10 wt.% and 15 wt.% to the total weight of polymer and carbon nanotubes. These CNTs loaded solutions were stirred for few hours to achieve a homogenous solution followed by ultra-sonication for 30 minutes. Another two sets of CNTs-polymer solutions were prepared with the same amount of CNTs loading with 10 wt.% of 1,2,6-trihydroxyhexane

and 2,4,6-trihydroxybenzaldehyde cross-linkers. Cross-linkers added solutions were further stirred for another 3 hours followed by 10 minutes of ultra-sonication. Thin films samples were prepared to assess the electrical and mechanical properties of CNT-polymer composite samples. Samples were synthesized on polyimide substrate (1.5×1.5 cm^2) using spin coating technique. The polyimide substrates were treated with plasma using UVO cleaner to enhance surface energy for better adhesion between substrate and composite. Once the plasma treatment was done, the polymer-carbon nanotube solution was carefully drop-casted onto the plasma-treated substrate and spin coated at 500 rpm for 30 seconds to spread the solution uniformly on the surface. Thin films with thickness of about 2 μm were obtained after curing for 24 hours at room temperature in a vacuum oven. These films were characterized to investigate their surface topography and electrical properties using AFM, SEM, and impedance spectroscopy. AFM image of the polymer thin film without loading CNTs reveals that the polymer film consists of a porous structure, i.e., the film is not continuous. The average pore size was about 10 μm. Observations on the AFM images of the polymer film reveal that crystallinity may form in the polymer itself. That may be the reason for the circular shape pattern with porous structure. This porosity in the polymer matrix is an obstacle for strain sensor fabrication. Because a sensor cannot be fabricated with imperfect inhomogeneous polymer matrix, as properties of the polymer matrix would affect the electrical and mechanical properties of the device. To investigate the crystallinity of this polymer can be done using Raman spectroscopy or Differential Scanning Calorimetry (DSC). If the porosity remains, then a slightly modified form of this polymer (polyurethane) can be used for future experiment. Composite thin films with CNTs loaded show less porosity in the film due to a strong van

der Waals' interaction between CNTs. The same observations can be seen in the cross-linkers added samples, i.e., less porosity in the samples. The surface roughness of these films is very high. A smoother surface can be achieved when sample synthesis is carried out with higher rpm in the spin coater. AFM images show the thickness of the samples around 2 μm. The film thickness also can be changed with rpm value.

The electrical properties of the composite thin films were determined based on Van der Pauw theory and four-point probe technique using a custom built experimental set up. The impedance spectra of the composite thin films with 1 wt.%, 5 wt.% and 8 wt.% loaded CNTs showed characteristic semi-circles, which are used to determine the electrical conductivity using the Van der Pauw equation and the distribution of CNTs in the polymer matrix. The electrical conductivity of composite thin films increased with the increase in CNTs content. The reported conductivity of these composite thin films is much higher than the conductivity reported in the literature and the frequency independent conductivity in the range 200-10^6 Hz which indicates the composite behaves as a conductor. For a strain sensor fabricated from composite thin films does not require higher conductivity than what we reported in this investigation. For the composite with higher conductivity, the change in the conductivity from the piezo-resistivity may not be detected easily. Therefore, the composite with less conductivity is preferred. To achieve a composite with less conductivity, the CNTs loading can be limited to less than 1 wt.%. Although the AC conductivity of these composites is much higher, the DC conductivity is still very low. To enhance the DC conductivity, metal nano-particles can be incorporated into the composites. To simulate the experimental data of Nyquist plot, the parallel RC-circuit model was used. Based on this model it is assessed that the dispersion of the CNTs

in the polymer matrix is uniform and homogenous which is good for electrical and mechanical properties.

The carbon nanotube composites with 1 wt.% cross-linkers showed interesting observations. For the low (1wt.%) and high (5 wt.%) content, CNTs loaded composite show higher electrical conductivity compared to its counterpart without cross-linkers. But low content CNTs composites show a semi-circle in the Nyquist plot, which indicates homogenous dispersion of CNTs in the polymer matrix. For the higher content (5 wt.%) loaded CNTs composites show no semi-circle in the Nyquist plot, which indicates formation of CNTs and polymer agglomerates, and poor dispersion of CNTs in the polymer matrix. It is concluded that for strain sensor device fabrication, composite with 1wt.% CNTs loaded composite is much better than higher content CNTs loaded composite. Assessment of the mechanical properties of the composite without/with cross-linkers and the device fabrication are the subject of future work.

REFERENCES

[1] T. Guo, C. M. Jin and R. Smalley, "Doping Bucky: Formation and Properties of Boron-Doped Buckminsterfullerene," *J. Phys. Chem.*, vol. 95, no. 13, pp. 4948-4950, 1991.

[2] S. Iijima and T. Ichihashi, "Single-shell carbon nanotubes of 1-nm diameter," *Nature*, vol. 263, no. 6430, pp. 603-605, 1993.

[3] K. S. Novoselov, A. K. Geim, S. V. Morozov, D. Jiang, Y. Zhang, S. V. Dubonos, I. V. Grigorieva and A. A. Firsov, "Electric Field Effect in Atomically Thin Carbon Films," *Science*, vol. 306, no. 5696, pp. 666-669, 2004.

[4] M. Holcomb, "Orbital Picture of Bonding: Orbital combinations, hybridization theory, and molecular orbitals," West Virginia University, [Online]. Available: http://community.wvu.edu/~miholcomb/hybridization.pdf.

[5] D. Tomanek and N. Frederick, "Cn Fullerenes," Michigan State University, [Online]. Available: http://www.nanotube.msu.edu/fullerene/fullerene.php?C=60.

[6] H. S. Philip Wong and D. Akinwande, Carbon nanotube and Graphene Device Physics, New York: Cambridge University Press, 2011.

[7] M. S. Dresselhaus, G. Dresselhaus and A. Jorio, Group Theory: Application to the Physics of Condensed Matter, Heidelberg: Springer, 2008.

[8] R. Saito, G. Dresselhaus and M. S. Dresselhaus, Physical Properties of Carbon Nanotubes, London: Imperial College Press, 1998.

[9] F. Michelis, L. Bodelot, C.-S. Cojocaru, J.-L. Sorin, Y. Bonnassieux and B. Lebental, "Wireless Flexible Strain Sensor Based on Carbon Nanotube Piezoresistivity Networks for Embedded Measurment of Strain in Concrete," in *7th European Workshop on Structural Health Monitoring*, La Cite, Nantes, France, 2014.

[10] A. Rochefort, D. R. Salahub and P. Avouris, "Effects of Finite Length on the Electronic Structure of Carbon Nanotubes," *J. Phys. Chem. B*, vol. 103, pp. 641-646, 1999.

[11] S. Iijima, "Helical microtubules of graphitic carbon," *Nature*, vol. 354, no. 6348, pp. 56-58, 1991.

[12] D. S. Bethune, C. H. Kiang, M. S. De Vries, G. Gorman, R. Savoy, J. Vazquez and R. Beyers, "Cobalt-Catalyzed Growth of Carbon Nanotubes with Single-Atomic-Layer walls," *Nature*, vol. 363, no. 6430, pp. 605-607, 1993.

[13] M. Meyyappan, CARBON NANOTUBES: SCIENCE AND APPLICATIONS, Boca Raton: CRC press, 2005.

[14] L. C. Qin, D. Zhou, A. R. Krauss and D. M. Gruen, "Growing carbon nanotubes by microwave plasma-enhanced chemical vapor deposition," *Appl. Phys. Lett.,* vol. 72, no. 3437, 1998.

[15] M. Okai, T. Muneyoshi, T. Yaguchi and S. Sasaki, "Structure of carbon nanotubes grown by microwave-plasma-enhanced chemical vapor deposition," *Appl. Phys. Lett.,* vol. 77, no. 3468, 2000.

[16] H. Cui, O. Zhou and B. R. Stoner, "Deposition of aligned bamboo-like carbon nanotubes via microwave plasma enhanced chemical vapor deposition," *J. Appl. Phys.,* vol. 88, no. 6072, 2000.

[17] L. Delzeit, I. McAninch, B. A. Cruden, D. Hash, B. Chen, J. Han and M. Meyyappan, "Growth of multiwall carbon nanotubes in an inductively coupled plasma reactor," *J. Appl. Phys.,* vol. 91, no. 6027, 2002.

[18] K. Matthews, B. A. Cruden, B. Chen, M. Meyyappan and L. Delzeit, "Plasma-Enhanced Chemical Vapor Deposition of Multiwalled Carbon Nanofibers," *J. Nanosci. Nanotech.,* vol. 2, no. 5, pp. 475-480, 2002.

[19] Z. F. Ren, Z. P. Huang, J. W. Xu, J. H. Wang and P. Bush, "Synthesis of Large Arrays of Well-Aligned Carbon Nanotubes on Glass," *Science,* vol. 282, no. 5391, pp. 1105-1107 , 1998.

[20] J.-h. Han, W.-S. Yang, J.-B. Yoo and C.-Y. Park, "Growth and emission characteristics of vertically well-aligned carbon nanotubes grown on glass substrate by hot filament plasma-enhanced chemical vapor deposition," *J. Appl. Phys.,* vol. 88, no. 7363, 2000.

[21] Y. H. Wang, J. Lin, C. H. A. Huan and G. S. Chen, "Synthesis of large area aligned carbon nanotube arrays from C 2 H 2 –H 2 mixture by rf plasma-enhanced chemical vapor deposition," *Apply. Phys. Lett.,* vol. 79, no. 680, 2001.

[22] V. I. Merkulov, D. H. Lowndes, Y. Y. Wei, G. Eres and E. Voelkl, "Patterned growth of individual and multiple vertically aligned carbon nanofibers," *Appl. Phys. Lett.,* vol. 76, no. 3555, 2000.

[23] M. Chhowalla, K. B. K. Teo, C. Ducati, N. L. Rupesinghe, G. A. J. Amaratunga, A. C. Ferrari, D. Roy, J. Robertson and W. I. Milne, "Growth process conditions of vertically aligned carbon nanotubes using plasma enhanced chemical vapor deposition," *J. Appl. Phys.,* vol. 90, no. 5308, 2001.

[24] L. Delzeit, C. V. Nguyen, B. Chen, R. Stevens, A. Cassell, J. Han and M. Meyyappan, "Multiwalled Carbon Nanotubes by Chemical Vapor Deposition Using Multilayered Metal Catalysts," *J. Phys. Chem. B,* vol. 106, no. 22, pp. 5629-5635, 2002.

[25] C. Bower, W. Zhu, S. Jin and O. Zhou, "Plasma-induced alignment of carbon nanotubes," *Appl. Phys. Lett.,* vol. 77, no. 830, 2000.

[26] F. Ding, P. Larsson, J. A. Larsson, R. Ahuja, H. Duan, H. Duan, A. Rose´n and K. Bolton, "The Importance of Strong Carbon−Metal Adhesion for Catalytic Nucleation of Single-Walled Carbon Nanotubes," *Nano Lett,* vol. 8, no. 2, pp. 463-468, 2008.

[27] T. W. Tombler, C. Zhou, L. Alexseyev, J. Kong, H. Dai, L. Liu, C. S. Jayanthi, M. Tang and S.-Y.

Wu, "Reversible electromechanical characteristics of carbon nanotubes under local-probe manipulation," *Nature,* vol. 405, pp. 769-772, 2000.

[28] N. Sinha, J. Ma and J. T. Yeow, "Carbon Nanotube-Based Sensors," *Journal of Nanoscience and Nanotechnology,* vol. 6, pp. 573-590, 2006.

[29] J. Hilding, E. A. Grulke, Z. G. Zhang and F. Lockwood, "Dispersion of Carbon Nanotubes in Liquids," *Journal of Dispersion Science and Technology,* vol. 24, no. 1, pp. 1-41, 2003.

[30] Y. Pan, L. Li, S. H. Chan and J. Zhao, "Correlation between dispersion state and electrical conductivity of MWCNTs/PP composites prepared by melt blending," *Composites: Part A,* vol. 41, pp. 419-426, 2010.

[31] J. Sandler, M. Shaffer, T. Prasse, W. Bauhofer, K. Schulte and A. Windle, "Development of a dispersion process for carbon nanotubes in an epoxy matrix and the resulting electrical properties," *Polymer,* vol. 40, pp. 5967-5971, 1999.

[32] E. Assouline, "Nucleation Ability of Multiwall Carbon Nanotubes in Polypropylene Composites," *Journal of Polymer Science: Part B: Polymer Physics,* vol. 41, pp. 520-527, 2003.

[33] B. Safadi, R. Andrews and E. Grulke, "Multiwalled Carbon Nanotube Polymer Composites:Synthesis and Characterization of Thin Films," *Journal of Applied Polymer Science,* vol. 84, pp. 2660-2669, 2002.

[34] R. Andrews, D. Jacques, M. Minot and T. Rantell, "Fabrication of Carbon Multiwall Nanotube/Polymer Composites by Shear Mixing," *Macromol. Mater. Eng.,* vol. 6, pp. 395-403, 2002.

[35] P. Potschke, A. Bhattacharyya and A. Janke, "Melt mixing of polycarbonate with multiwalled carbon nanotubes: microscopic studies on the state of dispersion," *European Polymer Journal,* vol. 40, p. 137–148, 2004.

[36] K. Mukhopadhyay, C. Dwivedi and G. Mathur, "Conversion of carbon nanotubes to carbon nanofibers by sonication," *Carbon,* vol. 40, pp. 1371-1376, 2002.

[37] X. Gong, J. Liu, S. Baskaran, R. Voise and J. Young, "Surfactant-Assisted Processing of Carbon Nanotube/Polymer Composites," *Chem. Mater.,* vol. 12, pp. 1049-1052, 2000.

[38] N. Hu, Z. Masuda, G. Yamamoto, H. Fukunaga, T. Hashida and J. Qiu, "Effect of fabrication process on electrical properties of polymer/multi-wall carbon nanotube nanocomposites," *Composite: Part A 39,* vol. 39, pp. 893-903, 2008.

[39] B. Kilbride, J. Coleman, J. Fraysse, P. Fournet, M. Cadek, A. Drury, S. Hutzler, S. Roth and W. J. Blau, "Experimental observation of scaling laws for alternating and direct current conductivity in polymer-carbon nanotube composite thin films," *Journal of Applied Physics,* vol. 92, pp. 4024-4030, 2002.

[40] T. Ogasawara, Y. Ishida, T. Ishikawa and R. Yokota, "Characterization of multi-walled carbon

nanotube/phenylethynyl terminated polyimide composites," *Composites: Part A,* vol. 35, pp. 67-74, 2004.

[41] A. Montazeri, J. Javadpour, A. Khavandi, A. Tcharkhtchi and A. Mohajeri, "Mechanical properties of multi-walled carbon nanotube/epoxy composites," *Materials and Design,* vol. 31, pp. 4202-4208, 2010.

[42] A. Martone, C. Formicola, M. Giordano and M. Zarrelli, "Reinforcement efficiency of multi-walled carbon nanotube/epoxy nano composites," *Composites Science and Technology,* vol. 70, pp. 1154-1160, 2010.

[43] P. Potschke, A. R. Bhattacharyya and A. Janke, "Carbon nanotube-filled polycarbonate composites produced by melt mixing and their use in blends with polyethylene," *Carbon,* vol. 42, pp. 965-969, 2004.

[44] M.-K. Seo and S.-J. Park, "Electrical resistivity and rheological behaviors of carbon nanotubes-filled polypropylene composites," *Chemical Physics Letters,* vol. 395, pp. 44-48, 2004.

[45] K. Ke, Y. Wang, X.-Q. Liu, J. Cao, Y. Luo, W. Yang, B.-H. Xie and M.-B. Yang, "A comparison of melt and solution mixing on the dispersion of carbon nanotubes in a poly(vinylidene fluoride) matrix," *Composites: Part B,* vol. 43, pp. 1425-1432, 2012.

[46] F. Du, J. E. Fischer and K. I. Winey, "Coagulation Method for Preparing Single-Walled Carbon Nanotube/Poly(methyl methacrylate) Composites and Their Modulus, Electrical Conductivity, and Thermal Stability," *Polymer Science Part B: Polymer Physics,* vol. 41, p. 3333–3338, 2003.

[47] J. Sandler, J. Kirk, I. Kinloch, M. Shaffer and A. Windle, "Ultra-low electrical percolation threshold in carbon-nanotube-epoxy composites," *Polymer,* vol. 44, pp. 5893-5899, 2003.

[48] R. H. Schmidt, I. A. Kinloch and A. N. W. A. H. Burgess, "The Effect of Aggregation on the Electrical Conductivity of Spin-Coated Polymer/Carbon Nanotube Composite Films," *Langmuir,* vol. 23, pp. 5707-5712, 2007.

[49] G. D. Seidel and D. C. Lagoudas, "A Micromechanics Model for the Electrical Conductivity of Nanotube-Polymer Nanocomposites," *Journal of Composite Materials,* vol. 43, no. 9, pp. 917-925, 2009.

[50] F. Deng and Q.-S. Zheng, "An analytical model of effective electrical conductivity of carbon nanotube composites," *APPLIED PHYSICS LETTERS,* vol. 92, pp. 071902-1-071902-3, 2008.

[51] Y. Simsek, L. Ozyuzer, A. T. Seyhan, M. Tanoglu and K. Schulte, "Temperature dependence of electrical conductivity in double-wall and multi-wall carbon nanotube/polyester nanocomposites," *Journal of Materials Science,* vol. 42, no. 23, pp. 9689-9695, 2007.

[52] C. Li, E. T. Thostenson and T.-W. Chou, "Dominant role of tunneling resistance in the electrical conductivity of carbon nanotube–based composites," *Applied Physics Letters,* vol. 91, pp. 223114-1-223114-3, 2007.

[53] M. Grujicic and G. Cao, "A computational analysis of the percolation threshold and the electrical conductivity of carbon nanotubes filled polymeric materials," *Journal of Materials Science,* vol. 39, pp. 4441-4449, 2004.

[54] M. Bryning, M. F. Islam, J. M. Kikkawa and G. A. Yodh, "Very Low Conductivity Threshold in Bulk Isotropic Single-Walled Carbon Nanotube–Epoxy Composites," *Advanced Materials,* vol. 17, pp. 1186-1191, 2005.

[55] M. A. Tupta, "Measuring the resistivity of bulk materials," Electronic Engineering Times, Europe, 2011.

[56] M. K. Njuguna, "Characterisation of Multi Wall Carbon Nanotube-Polymer Composites for Strain Sensing Applications," Queensland University of Technology, Brisbane, 2012.

[57] B. Kim, J. Lee and I. Yu, "Electrical properties of single-wall carbon nanotube and epoxy composites," *Journal of Applied Physics,* vol. 94, no. 10, pp. 6724-6728, 2003.

[58] A. Allaoui, S. Bai, H. Cheng and J. Bai, "Mechanical and electrical properties of a MWNT/epoxy composite," *Composites Science and Technology ,* vol. 62, pp. 1993-1998, 2002.

[59] C. Berger, Y. Yi, Z. Wang and W. de Heer, "Multiwalled carbon nanotubes are ballistic conductors at room temperature," *Appl. Phys. A,* vol. 74, pp. 363-365, 2002.

[60] N.-K. Chang, C.-C. Su and S.-H. Chang, "Fabrication of single-walled carbon nanotube flexible strain sensors with high sensitivity," *Applied Physics Letters,* vol. 92, pp. 063501-1-063501-3, 2008.

[61] I. Kang, M. J. Schulz, J. H. Kim, V. Shanov and D. Shi, "A carbon nanotube strain sensor for structural health monitoring," *Smart Mater. Struct.,* vol. 15, pp. 737-748, 2006.

[62] T. Yamada, Y. Hayamizu, Y. Yamamoto, Y. Yomogida, A. Izadi-Najafabadi, D. N. Futaba and K. Hata, "A stretchable carbon nanotube strain sensor for human-motion detection," *Nature Nanotechnology,* vol. 6, pp. 296-301, 2011.

[63] K. Loh, J. Lynch, B. Shim and N. Kotov, "Tailoring Piezoresistive Sensitivity of Multilayer Carbon Nanotube Composite Strain Sensors," *Journal of Intelligent Material Systems and Structures,* vol. 19, pp. 747-764, 2008.

[64] G. Yin, N. Hu, Y. Karube, Y. Liu, Y. Li and H. Fukunaga, "A carbon nanotube/polymer strain sensor with linear and anti-symmetric piezoresistivity," *Journal of Composite Materials,* vol. 45, no. 12, pp. 1315-1323, 2011.

[65] N. Hu, Y. Karube, M. Arai, T. Watanabe, C. Yan, Y. Li, Y. Liu and H. Fukunaga, "Investigation on sensitivity of a polymer/carbon nanotube composite strain sensor," *Carbon,* vol. 48, pp. 680-687, 2010.

[66] N. Hu, Y. Karube, C. Yan, Z. Masuda and H. Fukunaga, "Tunneling effect in a polymer/carbon nanotube nanocomposite strain sensor," *Acta Materialia,* vol. 56, pp. 2929-2936, 2008.

[67] R. Rizvi, B. Cochrane, E. Biddiss and H. Naguib, "Piezoresistance characterization of poly(dimethyl-siloxane) and poly(ethylene) carbon nanotube composites," *Smart Materials and Structures,* vol. 20, no. 094003, pp. 1-9, 2011.

[68] G. T. Pham, Y.-B. Park, Z. Liang, C. Zhang and B. Wang, "Processing and modeling of conductive thermoplastic/carbon nanotube films for strain sensing," *Composites: Part B,* vol. 39, pp. 209-216, 2008.

[69] M. Park, H. Kim and J. P. Youngblood, "Strain-dependent electrical resistance of multi-walled carbon nanotube/polymer composite films," *Nanotechnology,* vol. 19, no. 055705, pp. 1-7, 2008.

[70] J. Bautista-Quijano, F. Avilés, J. Aguilar, Tapia and A., "Strain sensing capabilities of a piezoresistive MWCNT-polysulfone film," *Sensors and Actuators A: Physical,* vol. 159, pp. 135-140, 2010.

[71] A. Oliva-Avile´s, F. Avile´s and V. Sosa, "Electrical and piezoresistive properties of multi-walled carbon nanotube/polymer composite films aligned by an electric field," *Carbon ,* vol. 49, pp. 2989-2997, 2011.

[72] C.-F. Hu, W.-S. Su and W. Fang, "Development of patterned carbon nanotubes on a 3D polymer substrate for the flexible tactile sensor application," *Journal of Micromechanics and Microengineering,* vol. 21, no. 115012, pp. 1-12, 2011.

[73] M. H. G. Wichmann, S. T. Buschhorn, L. Boger, R. Adelung, Schulte and Karl, "Direction sensitive bending sensors based on multi-wall carbon nanotube/epoxy nanocomposites," *Nanotechnology,* vol. 19, no. 475503, pp. 1-5, 2008.

[74] M. H. G. Wichmann, S. T. Buschhorn, J. Gehrmann and K. Schulte, "Piezoresistive response of epoxy composites with carbon nanoparticles under tensile load," *Physical Review B,* vol. 80, no. 245437, pp. 1-8, 2009.

[75] A. J. Paleo, F. W. J. van Hattum, J. Pereira, J. G. Rocha, Silva, J, V. Sencadas and S. Lanceros-Mendez, "The piezoresistive effect in polypropylene—carbon nanofibre composites obtained by shear extrusion," *Smart Materials and Structures,* vol. 19, no. 065013, pp. 1-7, 2010.

[76] S. Boncel, K. K. Koziol, K. Z. Walczak, A. H. Windle and M. S. Shaffer, "Infiltration of highly aligned carbon nanotube arrays with molten polystyrene," *Materials Letters,* vol. 65, pp. 2299-2303, 2011.

[77] P. Dharap, Z. Li, S. Nagarajaiah and E. V. Barrera, "Flexural strain sensing using carbon nanotube film," *Sensor Review,* vol. 24, pp. 271-273, 2004.

[78] X. Li, C. Levy and L. Elaadil, "Multiwalled carbon nanotube film for strain sensing," *Nanotechnology,* vol. 19, no. 045501, 2008.

[79] S. M. Vemuru, R. Wahi, S. Nagarajaiah, Ajayan and P. M, "Strain sensing using a multiwalled carbon nanotube film," *Journal od Strain Analysis ofr Engineering Design ,* vol. 44, pp. 555-562, 2009.

[80] X. Song, S. Liu, Z. Gan, Q. Lv, H. Cao and H. Yan, "Controllable fabrication of carbon nanotube-polymer hybrid thin film for strain sensing," *Microelectronic Enginnering* , vol. 86, pp. 2330-2333, 2009.

[81] Z. Li, P. Dharap, S. Nagarajaiah, E. V. Barrera and J. D. Kim, "Carbon Nanotube Film Sensors," *Advanced Materials*, vol. 16, no. 7, pp. 640-643, 2004.

[82] J. G. Simmons, "Generalized Formula for the Electric Tunnel Effect between Similar Electrodes Separated by a Thin Insulating Film," *Journal of Applied Phyics*, vol. 34, pp. 1793-803, 1963.

[83] K. Wasa, M. Kitabatake and H. Adachi, Thin Film Materials Technology: Sputtering of Compound Materials, New York: William Andrew, 2004.

[84] F. Penning, "Coating by cathode disintegration". United State Patent 2146025, 7 Feb. 1939.

[85] K. Wasa and H. Shigeru, "Low Pressure Sputtering System of the Magnetron Type," *The Review of Scientific Instruments*, vol. 40, no. 5, pp. 693-697, 1969.

[86] P. Kelly and R. Arnell, "Magnetron sputtering: a review of recent developments and applications," *Vacuum*, vol. 56, pp. 159-172, 2000.

[87] J. A. Thornton, "Magnetron sputtering: basic physics and application to cylindrical magnetrons," *The Journal of Vacuum Science and Technology*, vol. 15, pp. 171-177, 1978.

[88] N. Window and N. Savvides, "Charged particle fluxes from planar magnetron sputtering sources," *Journal of Vacuum Science & Technology A*, vol. 4, pp. 196-202, 1986.

[89] J. -E. Sundgren, L. Hultman, G. Håkansson, J. Birch and I. Petrov, "Formation of Defects During Ion-Assisted Growth of Thin Films from the Vapor Phase," *Materials Research Society*, vol. 268, pp. 71-82, 1992.

[90] G. Stringfellow, "Overview of the OMVPE Process," in *Organometallic Vapour-Phase Epitaxy*, San Diego, Academic Press, 1989, pp. 1-16.

[91] M. L. Hitchman and K. F. Jensen, Chemical Vapour Deposition: Principles and applications, San Diego: Academic Press, 1993.

[92] A. C. Jones and M. L. Hitchman, Chemical Vapour Deposition: Precursors, Process and Applications, Cambridge: Royal Society of Chemistry, 2009.

[93] J. R. Roth, "Industrial Plasma Enginerring, Vol.1," IOP, Bristol, 2001.

[94] J. Roth, "Industrial Plasma Engineering, Vol. 2," IOP, Bristol, 2001.

[95] M. L. Hitchman and K. F. Jensen, Chemical Vapour Deposition: Principles and Applications, New York: Acedemic Press, 1989.

[96] W. Kern and J. L. Vossen, Thin Film Processes II, London: Academic Press, 1991.

[97] M. A. Lieberman and A. .. J. Lichtenberg, Principles of Plasma Discharges and Materials Processing, New York: Wiley Interscience, 1994.

[98] P. Gregory, "Chemical Vapor Deposition," John Wiley & Sons, Inc., 1995. [Online]. Available: http://onlinelibrary.wiley.com/journal/10.1002/(ISSN)1521-3862. [Accessed 09 04 2015].

[99] D. B. Hall, P. Underhill and J. M. Torkelson, "Spin Coating of Thin and Ultrathin Polymer Films," *Polymer Engineering and Science*, vol. 38, no. 12, pp. 2039-2045, 1998.

[100] L. Feldman and J. M. Poate, "Rutherford Backscattering and Channeling Analysis of Interface and Epitaxial Structures," *Ann. Rev. Mater. Sci.*, vol. 12, pp. 149-76, 1982.

[101] M. Mayer, "Rutherford Backscattering Spectrometry (RBS)," EURATOM Association, Garching, 2003.

[102] R. J. Tesmer and M. Nastasi, Handbook of Modern Ion Beam Materials Analysis, Pittsburgh: Materials Research Society, 1995.

[103] D. Baer and S. Thevuthasan, "Characterization of Thin Films and Coating," in *Handbook of Deposition Technologies for Films and Coatings*, Oxford, Elsevier, 2010, pp. 749-856.

[104] "Western Michigan University: Department of Physics," [Online]. Available: http://tesla.physics.wmich.edu/Van_de_Graaff_Accelerator_Facility/.

[105] M. Mayer, "SIMNRA Home Page," Max-Planck-Institut für Plasmaphysik, [Online]. Available: http://home.rzg.mpg.de/~mam/.

[106] M. Mayer, "SIMNRA User's Guide," Max-Planck-Institut für Plasmaphysik, Garching, 1997.

[107] R. E. Dinnebier and S. J. L. Billinge, Powder Diffraction: Theory and Practice, Cambridge: Royal Society of Chemistry, 2008.

[108] A. Guinier, X-Ray Diffraction, San Francisco: W.H. Freeman and Company, 1963.

[109] B. Cullity, Elements of X-Ray Diffraction, Massachusets: Addison-Wesley Publishing Company, Inc., 1956.

[110] C. Kittel, Introduction to Solid State Physics, John Wiley & Sons, 2004.

[111] M. F. C. Ladd and R. A. Palmer, Structure Determination by X-ray Crystallography, New York: Plenum Press, 1993.

[112] A. T. Jensen, "Determination of Particle Size By the X-ray Powder Method," 1943.

[113] A. Patterson, "The Scherrer Formula for I-Ray Particle Size Determination," *Physical Review*, vol. 56, pp. 978-982, 1939.

[114] EMSL, "Multipurpose XRD," [Online]. Available:

http://www.emsl.pnl.gov/emslweb/instruments/multipurpose-xrd.

[115] F. J. Watts and J. Wolstenholme, An Introduction to Surafce Analysis by XPS and AES, Chichester: John Wiley & Sons Ltd, 2003.

[116] D. Briggs and M. Seah, Practical Surafce Analysis: Auger and X-ray Photoelectron Spectroscopy, New York: John Wiley & Sons, 1990.

[117] J. M. Wagner, X-ray Photoelectron Spectroscopy, New York: Nova Science Publisher, Inc., 2011.

[118] K. Siegbahn, Alpha- beta- and gamma-ray spectroscopy, Amsterdam: North-Holland Pub. Co, 1965.

[119] J. F. Moulder, W. F. Stickle, P. E. Sobol and K. D. Bomben, Handbook of X-ray Photoelectron Spectroscopy, Eden Prairie: Physical Electronics, Inc., 1995.

[120] C. Powell, "NIST Electron Inelastic-Mean-Free-Path Database," U.S. Secretary of Commerce, Gaithersburg, 2010.

[121] S. Tanuma, C. Powell and D. Penn, "Calculation of Electron Inelastic Mean Free Paths for 31 Materials," *Surface and Interface Analysis,* vol. 11, p. 5770589, 1988.

[122] S. Tanuma, "Calculations of Electron Inelastic Mean Free Paths," *Surface and Interface Analysis,* vol. 20, pp. 77-89, 1993.

[123] J. R. Ferraro, K. Nakamoto and C. W. Brown, Introductory Raman Spectroscopy, San Diego: Academic Press, 2003.

[124] P. Larkin, "Infrared and Raman Spectroscopy: Principles and Spectral Interpretation," Elsevier Inc., San Diego, 2011.

[125] D. L. Gerrard and J. Birnie, "Raman spectroscopy," *Analytical Chemistry,* vol. 64, no. 12, pp. 502-513, 1992.

[126] A. Smekal, "The quantum theory of dispersion," *Naturwissenschaften,* vol. 11, pp. 873-875, 1923.

[127] A. H. Compton, "A QUANTUM THEORY OF THE SCATTERING OF X-RAYS BY LIGHT ELEMENTS," *The Physical Review ,* vol. 21, no. 5, pp. 483-502, 1923.

[128] C. Raman and K. S. Krishnan, "The optical analogue of the Compton effect," *Nature,* vol. 121, p. 711, 1928.

[129] C. Raman and K. Krishnan, "The Production od New Radiations by Light Scatetring-Part 1," *Ind. J. Phys.*, vol. 2, p. 387, 1928.

[130] C. Raman, "The molecular scattering of light," Elsevier, Amsterdam, 1930.

[131] J. Heath and N. Taylor, "Energy Dispersive Spectroscopy," John Wiley & Sons Ltd, Chichester, 2015.

[132] L. J. van der Pauw, "A method of measuring spesific resistivity and Hall effect of discs of arbitary shape," *Philips Research Reports,* vol. 13, no. 1, pp. 1-9, 1958.

[133] N. Liu, F. Wei, L. Liu, H. S. S. Lai, H. Yu, Y. Wang, G.-B. Lee and W. J. Li, "Optically-controlled digital electrodeposition of thin-film metals for fabrication of nano-device," *Optical Materials Express,* vol. 5, no. 4, pp. 838-848, 2015.

[134] D. C. Grahame, "The Electrical Double Layer and the Theory of Electrocapillarity," *Chemical Reviews,* vol. 41, no. 3, pp. 441-501, 1947.

[135] H. Bauer, "Alternating Current Polarography and Tensammetry," *Journal of Electroanalytical Chemistry,* vol. 1, pp. 363-378, 1959/60.

[136] J. R. Macdonald, "Impedance Spectroscopy," *Annals of Biomedical Engineering,* vol. 20, pp. 289-305, 1992.

[137] B.-Y. Chang and S.-M. Park, "Electrochemical Impedance Spectroscopy," *Annual Review of Analytical Chemistry,* vol. 3, pp. 207-229, 2010.

[138] V. Vermeeren and L. Michiels, "Evolution Towards the Implementation of Point-Of-Care Biosensors," Hasselt University.

[139] G. Binning, H. Rohrer, C. Gerber and E. Weibel, "Surface Studies by Scanning Tunneling Microscopy," *The American Physical Society,* vol. 49, no. 1, pp. 57-60, 1982.

[140] G. Binning and C. Quate, "Atomic Force Microscope," *Physical Review Letters,* vol. 56, no. 9, pp. 930-934, 1986.

[141] E. Meyer, "Atomic Force Microscopy," *Progress in Surface Science,* vol. 41, pp. 3-49, 1992.

[142] C. R. Blanchard, "Atomic Force Microscopy," *The Chemical Educator,* vol. 1, no. 5, pp. 1-8, 1996.

[143] D. Rugar and P. Hansma, "Atomic Force Microscopy," *Physics Today,* vol. 43, no. 10, pp. 23-30, 1990.

[144] F. J. Giessible, "Atomic Resolution of the Silicon (111)-(7*7) Surface by Atomic Force Microscopy," *Science ,* vol. 267, pp. 68-71, 1995.

[145] R. Garcia and A. S. Paulo, "Dynamics of a vibrating tip near or in intermittent contact with a source," *Physical Review B,* vol. 61, no. 20, pp. 381-384, 2000.

[146] Y. J. Yoon, J. C. Bae, H. K. Baik, S. J. Cho, S.-J. Lee, K. M. Song and M. N. Seung, "Growth control of single and multi-walled carbon nanotubes by thin film catalyst," *Chemical Physics Letters,* vol. 366, pp. 109-114, 2002.

[147] C. Bower, O. Zhou, W. Zhu, D. J. Werder and S. Jin, "Nucleation and growth of carbon nanotubes by microwave plasma chemical vapor deposition," *Applied Physics Letters,* vol. 77, no. 17, pp. 2767-2769, 2000.

[148] Z. Huang, D. Wang, J. Wen, M. Sennette, H. Gibson and Z. Ren, "Effect of nickel, iron and cobalt on growth of aligned carbon nanotubes," *Applied Physics A: Materials Science and Processing*, vol. 74, pp. 387-391, 2002.

[149] A.-C. Dupuis, "The catalyst in the CCVD of carbon nanotubes-a review," *Progress in Materials Science* , vol. 50, pp. 929-961, 2005.

[150] Y. Murakami, S. Chiashi, Y. Miyauchi, M. Hu, M. Ogura, T. Okubo and S. Maruyama, "Growth of vertically aligned single-walled carbon nanotube films on quartz substrates and their optical anisotropy," *Chemical Physics Letters*, vol. 385, pp. 298-303, 2004.

[151] E. Flahaut, R. Bacsa, A. Peigney and C. Laurent, "Gram-scale CCVD synthesis of double-walled carbon nanotubes," *Chem. Commun.*, pp. 1442-1443, 2003.

[152] H. Yu, Q. Zhang, G. Luo and F. Wei, "Rings of triple-walled carbon nanotube bundles," *Applied Physics Letters*, vol. 89, pp. 1-3, 2006.

[153] G. Lolli, L. Zhang, L. Balzano, N. Sakulchaicharoen, Y. Tan and D. E. Resasco, "Tailoring (n,m) Structure of Single-Walled Carbon Nanotubes by Modifying Reaction," *J. Phys. Chem. B*, vol. 110, no. 5, pp. 2108-2115, 2006.

[154] J. F. Ziegler, J. P. Biersack and M. D. Ziegler, "The Stopping and Range of Ions in Matter," *Nuclear Instruments and Methods in Physics Research B*, vol. 268, pp. 1818-1823, 2010.

[155] J. F. Ziegler, "James Ziegler-SRIM & TRIM," [Online]. Available: www.srim.org/SRIM/SRIMLEGL.htm.

[156] J. Daillant and A. Gibaud, X-ray and Neutron Reflectivity, Berlin: Springer, 2009.

[157] D. Chateigner, "X-Ray Reflectivity," in *Combined Analysis*, Wiley, 2010, pp. 235-256.

[158] P. Colombi, D. K. Agnihotri, V. E. Asadchikov, E. Bontempi, D. K. Bowen, C. H. Chang, L. E. Depero, M. Farnworth, T. Fujimoto, A. Gibaud, M. Jergel, M. Krumrey, T. A. Lafford, A. Lamperti, T. Ma, R. J. Matyai, M. Meduna and S. S. K. Milita, "Reproducibility in X-ray reflectometry: results from the first world-wide round-robin experiment," *Journal of Applied Crystallography*, vol. 41, pp. 143-152, 2008.

[159] N. Abdellaoui, A. Pillonnet, J. Berndt, C. Boulmer-Leborgne, E. Kovacevic, B. Moine, J. Penuelas and A. Pereira, "Growth process of nanosized aluminum thin films by pulsed laser deposition for fluorescence enhancement," *Nanotechnology*, vol. 26, pp. 1-7, 2015.

[160] R. Jaccodine, "Surafce Energy of Germanium and Silicon," *Journal of the Electrochemical Society*, vol. 110, no. 6, pp. 524-527, 1963.

[161] V. M. Kuznetsov, R. I. Kadyrov and G. E. Rudenskii, "Calculation of Surface Energy of Metals and Alloys by the Electron Density Fuctional Method," *Journal of Material Science Technology*, vol. 14, pp. 320-322, 1998.

[162] T. C. Campbell, "Ultrathin metals films and particles on oxide surfaces: structural, electronic and chemisorptive properties," Elsevier, New York, 1997.

[163] A. Katsman, Y. Yaish, E. Rabkin and M. Beregovsky, "Surafce Diffusion Controlled Formation of Nickel Silicides in Silicon Nanowires," *Journal of Electronic Materials* , vol. 39, no. 4, pp. 365-370, 2010.

[164] G. D. Nessim, A. J. Hart, J. S. Kim, D. Acquaviva, J. Oh, D. C. Morgan, M. Seita, J. S. Leib and C. V. Thompson, "Tuning of Vertically-Aligned Carbon Nanotube Diameter and Areal Density through Catalyst Pre-Treatment," *Nano Letters,* vol. 8, no. 11, pp. 3587-3593, 2008.

[165] A. Okita, S. Yoshiyuki, A. Oda, J. Nakamura, A. Ozeki, K. Bhattacharyya, H. Sugawara and Y. Sakai, "Effect of hydrogen on carbon nanotube formation in CH4/H2 plasmas," *Carbon,* vol. 45, pp. 1518-1526, 2007.

[166] E. Jiran and C. Thompson, "Capillary Instabilities in Thin Films," *Journal of Electronic Materials,* vol. 19, no. 11, pp. 1153-1160, 1990.

[167] I. B. Denysenko, S. Xu, J. D. Long, P. P. Rutkevych, N. A. Azarenkov and K. Ostrikov, "Inductively coupled Ar/CH 4 / H 2 plasmas for low-temperature deposition of ordered carbon nanostructures," *J. Appl. Phys.,* vol. 95, no. 2713, 2004.

[168] V. Vinciguerra, F. Buonocore, G. Panzera and L. Occhipinti, "Growth mechanisms in chemical vapour deposited carbon nanotubes," *Nanotechnology,* vol. 14, pp. 655-660, 2003.

[169] Y. Yan, J. Miao, Z. Yang, F.-X. Xiao, H. B. Yang, B. Liu and Y. Yang, "Carbon nanotube catalysts: recent advances in synthesis, characterization and applications," *Chem Soc Rev,* vol. 44, pp. 3295-3346, 2015.

[170] M. Dresselhaus, A. Jorio and R. Saito, "Characterzing Graphene, Graphite, and Carbon Nanotubes by Raman Spectroscopy," *Annu. Rev. Condens. Matter Phys.,* vol. 1, pp. 89-108, 2010.

[171] S. M. Dresselhaus, A. Jorio, M. Hofmann, G. Dresselhaus and R. Saito, "Perspectives on Carbon Nanotubes and Graphene Raman Spectroscopy," *Nano Letters,* vol. 10, pp. 751-758, 2010.

[172] H. Weik and P. Hemenger, "Existence of the hexagonal modification of nickel Locality: synthetic," *Bulletin of the American Physical Society,* vol. 10, p. 1140, 1965.

[173] C. Kittel, Introduction to Solid State Physics, John Wiley & Sons, Inc., 2004.

[174] M. C. Biesinger, B. P. Payne, L. W. M. Lau, A. Gerson and R. S. C. Smart, "X-ray photoelectron spectroscopic chemical state quantification of mixed nickel metal, oxide and hydroxide systems," *Surf. Interface Anal.,* vol. 41, pp. 324-332, 2009.

[175] Y. Goto, K. Taniguchi, T. Omata, S. Otsuka-Yao-Matsuo, N. Ohashi, S. Ueda, H. Yoshikawa, Y. Yamashita, H. Oohashi and K. Kobayashi, "Formation of Ni3C Nanocrystals by Thermolysis of Nickel Acetylacetonate in Oleylamine: Characterization Using Hard X-ray Photoelectron Spectroscopy," *Chem. Mater,* vol. 20, p. 4156–4160, 2008.

[176] B. Yan, J. Liu, B. Song, P. Xiao and L. Lu, "Li-rich Thin Film Cathode Prepared by Pulsed Laser Deposition," *Scientific Reports,* vol. 3, pp. 1-5, 2013.

[177] Y. Cao, L. Nyborg and U. Jelvestam, "XPS calibration study of thin-film nickel silicides," *Surafce and Interface Analysis,* vol. 41, pp. 471-483, 2009.

[178] P. Tam and L. Nyborg, "Sputter deposition and XPS analysis of nickel silicide thin films," *Surface & Coatings Technology,* vol. 203, pp. 2886-2890, 2009.

[179] Y. Y. Wei, G. Eres, V. I. Merkulov and D. H. Lowndes, "Effect of catalyst film thickness on carbon nanotube growth by selective area chemical vapor deposition," *Applied Physics Letters,* vol. 78, no. 10, pp. 1394-1396, 2001.

[180] S. Esconjauregui, C. M. Whelan and K. Maex, "Carbon nanotube catalysis by metal silicide: resolving inhibition versus growth," *Nanotechnology,* vol. 18, pp. 1-11, 2007.

[181] T. Young, "An essay on the cohesion of fluids," *Philosophical Transactions of the Royal Society of London,* vol. 95, pp. 65-87, 1805.

[182] D. Owens and R. Wendt, "Estimation of the Surafce Free Energy of Polymers," *Journal of Applied Polymer Science,* vol. 13, pp. 1741-1747, 1969.

[183] D. S. McLachlan, C. Chiteme, C. Park, K. E. Wise, S. E. Lowther, P. T. Lillehei, E. Siochi and J. S. Harrison, "AC and DC Percolative Conductivity of Single Wall Carbon Nanotube Polymer Composites," *Journal of Polymer Science: Part B: Polymer Physics,* vol. 43, pp. 3273-3287, 2005.

[184] Y.-J. Wang, Y. Pan, X.-W. Zhang and K. Tan, "Impedance Spectra of Carbon Black Filled High-Density Polyethylene Composites," *Journal of Applied Polymer Science,* vol. 98, pp. 1344-1350, 2005.

[185] M. Miao, "Electrical conductivity of pure carbon nanotube yarns," *Carbon,* vol. 49, pp. 3755-3761, 2011.

[186] P. Singh, S. A. Ali and R. Kumar, "Modification of structural, optical and chemical properties of Li3+ irradiated polyurethane and polyetheretherketone," *Radiation Physics and Chemistry,* vol. 96, pp. 181-185, 2014.